ULTRAFAST COHERENT ELECTRON SPIN CONTROL AND CORRELATED TUNNELING DYNAMICS OF TWO-DIMENSIONAL ELECTRON GASES

by

CAREY E. PHELPS

A DISSERTATION

Presented to the Department of Physics
and the Graduate School of the University of Oregon
in partial fulfillment of the requirements
for the degree of
Doctor of Philosophy

June 2011

DISSERTATION APPROVAL PAGE

Student: Carey E. Phelps

Title: Ultrafast Coherent Electron Spin Control and Correlated Tunneling Dynamics of Two-Dimensional Electron Gases

This dissertation has been accepted and approved in partial fulfillment of the requirements for the Doctor of Philosophy degree in the Department of Physics by:

Dr. Daniel Steck	Chair
Dr. Hailin Wang	Advisor
Dr. Jens Nöckel	Inside
Dr. John Toner	Inside
Dr. Andrew Marcus	Outside
and	
Richard Linton	Vice President for Research and Graduate Studies/ Dean of the Graduate School

Original approval signatures are on file with the University of Oregon Graduate School.

Degree awarded June 2011

DISSERTATION ABSTRACT

Carey E. Phelps

Doctor of Philosophy

Department of Physics

June 2011

Title: Ultrafast Coherent Electron Spin Control and Correlated Tunneling Dynamics of Two-Dimensional Electron Gases

Approved: _____

Dr. Hailin Wang

Electron spins form a two-level quantum system in which the remarkable properties of quantum mechanics can be probed and utilized for many applications. By learning to manipulate these spins, it may be possible to construct a completely new form of technology based on the electron spin degree of freedom, known as spintronics. The most ambitious goal of spintronics is the development of quantum computing, in which electron spins are utilized as quantum bits, or qubits, with properties that are not possible with classical bits. Before these ideas can become reality, a system must be found in which spin lifetimes are long enough and in which spins can be completely controlled. Semiconductors are an excellent candidate for electron spin control since they can be integrated into on-chip devices and produced on a scalable level.

The focus of this dissertation is on electron spin control in two different semiconductor systems, namely a two-dimensional electron gas in a modulation-doped quantum well and donor-bound electrons in bulk semiconductors. Both systems have been studied extensively for a variety of purposes. However, the ability to manipulate spins has been elusive. In this dissertation, the first experimentally successful demonstration of electron spin control in a two-dimensional electron gas is presented, in which ultrafast optical pulses induce spin rotations via the optical Stark effect.

Donor-bound electron spin manipulation in bulk semiconductors is also investigated in this dissertation. Important information was obtained on the limiting factors that serve to prohibit spin control in this system. By taking these new factors into account, it is our hope that full electron spin control can eventually be accomplished in this system.

Finally, through the course of investigating electron spin dynamics, a strange nonlinear optical behavior was observed in a bilayer system, which was determined to result from a coupling of optical interactions with tunneling rates between layers. The data suggest that there is a strong interplay between interlayer and intralayer correlations in this system. Investigations into the nature of this interaction were undertaken and are presented in the last part of this dissertation.

This dissertation includes previously published and unpublished co-authored material.

CURRICULUM VITAE

NAME OF AUTHOR: Carey E. Phelps

GRADUATE AND UNDERGRADUATE SCHOOLS ATTENDED:

University of Oregon, Eugene, Oregon

DEGREES AWARDED:

Doctor of Philosophy in Physics, 2011, University of Oregon
Bachelor of Science in Physics and Mathematics, 2005, University of Oregon

AREAS OF SPECIAL INTEREST:

Quantum information processing
Alternative energy sources
DNA functionality

PROFESSIONAL EXPERIENCE:

Graduate research assistant,
University of Oregon, 2006 – 2011
Graduate teaching fellow,
University of Oregon, 2005 – 2011

GRANTS, AWARDS AND HONORS:

Graduated with physics departmental honors.

PUBLICATIONS:

Carey Phelps, Shannon O'Leary, John Prineas, and Hailin Wang, "Coherent Spin Dynamics of Donor-bound Electrons in GaAs", *submitted for review.*

Timothy Sweeney, Carey Phelps, and Hailin Wang, "Quantum Control of Electron Spins in Semiconductors with Phase-Locked Raman Pulse Pairs", *submitted for review.*

Carey Phelps, John Prineas, and Hailin Wang, "Excitonic Nonlinear Optical Response from Correlation-enhanced Tunneling in Mixed-type GaAs Quantum Wells" Phys. Rev. B **83**, 153302, (2011).

Carey Phelps, Timothy Sweeney, Ronald T. Cox, and Hailin Wang, "Ultrafast Coherent Electron Spin Flip in a Modulation-Doped CdTe Quantum Well" Phys. Rev. Lett. **102**, 237402, (2009).

ACKNOWLEDGEMENTS

First of all, I must thank my advisor, Hailin Wang, for all of his time and patience. His enthusiasm for my projects helped motivate me to succeed when progress looked bleak. I will never forget the many amazing things he has done for me for which I will never be able to thank him adequately. He ultimately shaped me into the scientist that I am today.

I must thank all of my labmates whom have come and gone through the years, teaching me a great deal of experimental technique, and being excellent friends that made coming into lab unpredictable and strange. I should specifically mention Timothy Sweeney, Shannon O'Leary, Young-Shin Park, Nima Dinyari, and Yan Guo, who contributed the most to my early progress when things were the most difficult. However, there has not been a single person in our lab who did not have something useful or interesting to impart to me, and I hope that I could do the same for them in some way.

I am extremely grateful to the local experts we have on campus whose skills helped me through some special challenges along the way; namely, Kris Johnson, Cliff Dax, Larry Scatena, and Kurt Langworthy. They are invaluable resources and could never possibly be paid as much as they deserve.

Most of all, I want to thank my family for all of the support they have shown me. My lovely wife, Mary Robinson, who tried to calm me down when I was stressed out on a semi-daily basis. I was lucky enough to have her working in the same building with me, where I could see her periodically and share my happiness or frustration with her throughout the day. Also my parents, who have always believed that I could do anything and were willing to make sacrifices to help me pursue my dreams. I am so happy to know that they can share in this accomplishment with me.

Finally, I want to acknowledge the existence of Bryan Wollen, Jon Timm, Alan Ullman, and Jessie Jonas.

For Mary, with whom I violate the Paul exclusion principle. We are two indistinguishable people who will inhabit the same quantum state for life.

TABLE OF CONTENTS

LIST OF FIGURES

LIST OF TABLES

CHAPTER I

INTRODUCTION

Spintronics

Semiconductors are an integral part of our society, forming the foundation for many technologies that have greatly increased our quality of life, such as computer chips, cell phones, solar panels, and solid state lasers, to name a few. Some of the most amazing applications of semiconductors result from their ability to provide a convenient environment in which quantum mechanical effects can be probed and manipulated. Electron spin and quantum tunneling are two such quantum mechanical effects that will be the focus of this dissertation.

Electrons have a spin degree of freedom which could be manipulated to provide us with an all new form of technology, known as spintronics [1], meaning spin based electronics. The most ambitious goal of spintronics is to store information in electron spins in the form of a qubit (quantum bit) for use in quantum information processing. Ultimately, it is hoped that qubits can be controlled with high enough precision to create a quantum computer. Quantum computers were first proposed in a famous publication by Richard Feynman [2], and have lead to intense research interest in seeking a suitable qubit in a variety of systems.

Semiconductors are of particular interest in the pursuit of quantum information processing and spintronics because they are suitable for scalable, on-chip devices. Along with this convenient aspect of semiconductors comes a host of challenges that need to be overcome before spin manipulation can become profitable. Electron spins must be completely controllable and must demonstrate lifetimes that are long enough for relevant applications. Most applications of spintronics have been focused on spin dependent transport, which is manipulated electronically or through external magnetic fields. However, recent interest has been focused on optical control of electron spins, which can be performed on a much faster scale.

The most successful application of spintronics to date stems from an effect known as giant magnetoresistance (GMR), a discovery for which Albert Fert and Peter Grünberg were awarded the 2007 Nobel Prize in physics. In GMR, the spin properties of electrons can greatly influence the resistance of a material composed of alternating ferromagnetic and non-magnetic layers [3]. Currents induced in a circuit containing such a lattice are extremely sensitive to the presence of external magnetic fields. This, and other similar spin dependent effects, have been utilized in modern hard disk storage devices.

The majority of spintronic research has been directed toward ferromagnetic metal alloys and ferromagnetic semiconductors. Ferromagnetic semiconductors are produced by doping a semiconductor with magnetic ions, such as manganese. Control of spins within these devices is achieved through application of an external

magnetic field, or through manipulation of the spin-orbit interaction. Spin-orbit interactions in semiconductors are generally described by Dresselhaus [4] and Rashba [5] spin-orbit coupling, which are due to bulk and structural inversion asymmetry, respectively, and can be influenced by an applied voltage.

Spin manipulation through these means are ultimately temporally limited by the electronics which perform the spin control function to ~ 50 nanoseconds (ns). Alternatively, optical interactions with spins can be performed on a much faster timescale. Optical pulses with durations on the order of picoseconds (ps), or even femtoseconds (fs), are now commonplace in modern optical laboratories. By application of such pulses, spin control can be employed on an ultrafast scale, which is important for quantum information technologies.

Optical Electron Spin Manipulation in Semiconductors

For the most part, ultrafast optical research on semiconductor spin systems has been conducted in three major semiconductor structures. These are quantum dots, modulation-doped quantum wells, and donor-bound electrons in bulk semiconductors. Each system has its own inherent pros and cons.

Quantum dots are the most ideal system of the three as far as single spin control is concerned, because spins within quantum dots are immobile, demonstrate long lifetimes ($\sim$ ms), and are accessed via sharp, atomic-like transitions. Working with single quantum dots presents many technical challenges in that the quality of dots

greatly varies, their spatial location is determined by chance, and measurements require low signal detection techniques. For large scale qubit based devices, these technical challenges seem overwhelming at our present state. However, overcoming these challenges in single quantum dots may prove to be fruitful, since these systems demonstrate long electron lifetimes, and since high fidelity spin control has been demonstrated within them.

Early demonstrations of spin control in quantum dots were performed through control of the exchange interaction between two quantum dots [6], through pulsed external magnetic fields [7], or through pulsed microwaves [8]. These manipulation techniques were performed using electronic devices, and thus were temporally limited to a control time on the order of nanoseconds. Many applications involving electron spins, such as quantum computing, require faster manipulation times, on the order of picoseconds (ps). As a result, it was necessary for other control techniques to be investigated in the ultrafast regime. Over the next few years, a series of papers were published in which spin control was demonstrated in single quantum dots using ultrafast optical pulses ($\sim$ 2 ps) by J. Berezovsky *et al.* [9], D. Press *et al.* [10], and E. Kim *et al.* [11]. Rotations in ensembles of quantum dots have also been demonstrated by A. Greilich *et al.* [12].

Ensemble spin systems are also of interest since they have applications in spintronics and in quantum computing related devices such as quantum repeaters [13]. Although quantum dots are the clear front runner for single spin qubits in

semiconductors, ensembles of quantum dots demonstrate a large inhomogeneous broadening due to the distribution of quantum dot sizes that result during the growth process, which is not experienced in the other two semiconductor spin systems mentioned above. This large inhomogeneous broadening can greatly limit the fidelity of spin control, and therefore we prefer to investigate spin control in other ensemble spin systems. Donor-bound electrons in bulk semiconductors are ensemble spin systems which are relatively homogeneous. Optical transitions in which donor-bound electrons are accessed generally demonstrate linewidths of shorter than 1 Å [14]. Like quantum dots, donor-bound electrons are immobile and demonstrate spin lifetimes on the order of milliseconds [15]. These properties make donor-bound electron spins highly attractive for ensemble spin applications. The downside of the donor-bound electron spin system is that spin control appears to be much more difficult in this system than in quantum dots or modulation-doped quantum wells. This topic will be discussed at length in chapter V in which we present our own experimental results on spin control in this system.

Modulation-doped semiconductor quantum wells are another ensemble spin system in which electron spin coherence has been studied extensively. Unlike the other two semiconductor spin systems, the electrons whose spins are manipulated are mobile, and hence subject to spin-orbit coupling through the afore mentioned Rashba and Dresselhaus spin-orbit interactions. This greatly limits the dephasing time of the spins to times of the order of tens of ns [16]. Additionally, electron

spins in quantum wells are subject to many-body interactions and experience dipole decoherence times on the order of 2 ps [17]. These factors make electron spin control in this system extremely challenging, and have resulted in limited success in prior spin control attempts [18–20]. However, our success in this system has demonstrated that these limiting factors can be overcome [21], as will be discussed at length in chapter IV. Experimental progress in this system is valuable for quantum information technology as a whole since knowledge gained in this system can be applied to other systems, such as quantum dots, in which the spin control techniques are essentially the same.

Dissertation Overview

The focus of this dissertation is on three fronts: (1) ultrafast optical electron spin manipulation of 2D electron gases in modulation-doped quantum wells, (2) ultrafast optical donor-bound electron spin manipulation in bulk semiconductors, and (3) correlation-enhanced tunneling effects in mixed-type quantum wells.

Chapter II is an overview of the basics of semiconductors, targeting the details which are necessary for an understanding of the experimental data presented in the following chapters. Chapter III contains a full theoretical treatment of the mechanism utilized in this dissertation for electron spin control. Chapter IV focuses on ultrafast optical manipulation of electron spins in a modulation-doped CdTe quantum well in which the first experimental demonstration of complete electron

spin flips in this system is presented. Chapter V documents our attempts to apply the same technique to donor-bound electrons in bulk semiconductors. Although this endeavor was not as successful, much was learned about the limiting factors which must be overcome for successful donor-bound electron spin control, and the data presented is along those lines. In chapter VI we present surprising experimental data in which excitonic excitation can greatly enhance tunneling rates in a bilayer system. Chapter VII is a summary of the dissertation.

Chapter IV contains previously published material with co-authors Timothy Sweeney, Ronald T. Cox, and Hailin Wang. Chapter V contains material that is currently unpublished, although portions of it have been submitted for review with co-authors Shannon O'Leary, John Prineas, and Hailin Wang, and subsequent portions are currently under production for a second submission with co-authors Liming Zhang and Hailin Wang. Chapter VI contains previously published material with co-authors John Prineas and Hailin Wang.

CHAPTER II

SEMICONDUCTOR BAND STRUCTURE

Bulk Semiconductors

The energy structure of semiconductors is composed of a series of energy bands, which are known as conduction bands and valence bands. An electron is said to be in a valence band if it occupies a state in the valence shell of the atoms which compose the material. Alternatively, an electron in the conduction band has the ability to move freely through the material, unbound by the constituent atoms. The minimum energy necessary to excite an electron from the valence to the conduction band is known as the band gap energy. Band gap energies at low temperature for the materials to be discussed throughout this dissertation are: 1.52 eV for GaAs, 1.61 eV for CdTe, and 1.42 for InP [22].

Excitation of an electron from the valence band to the conduction band results in a vacancy in the valence band. This vacancy has a net positive charge and can be treated as a quasiparticle called a hole. Because the semiconductor valence band is a p-type orbital, the hole energy depends on its angular momentum state. The hole spin can take on the values $s = \pm\frac{1}{2}$. In a p-orbital, $l = 1$, therefore, the total angular momentum for a hole can take on the values $j = \frac{1}{2}$ or $\frac{3}{2}$. For $j = \frac{1}{2}$, the

z-component of the angular momentum can take on the values $j_z = \pm\frac{1}{2}$. For $j = \frac{3}{2}$, the z-component of angular momentum can take on the values $j_z = \pm\frac{1}{2}$ or $\pm\frac{3}{2}$

In bulk semiconductors, under zero magnetic field, three separate valence bands exist which are dependent on the angular momentum state of the holes. These valence bands are called the light hole band, the heavy hole band, and the split-off band. A representative diagram of bulk semiconductor band structure is shown in Fig. 2.1. Holes occupy the heavy hole valence band when $j = \frac{3}{2}$ and $j_z = \pm\frac{3}{2}$, the light hole band when $j = \frac{3}{2}$ and $j_z = \pm\frac{1}{2}$, and the split-off band when $j = \frac{1}{2}$ [23]. At zero wave vector ($k = 0$), the light and heavy hole bands are degenerate, but they are non-degenerate for $k \neq 0$. In direct gap semiconductors, the band structure is approximately parabolic near ($k = 0$). The curvature of the band near ($k = 0$) determines the effective mass of the particles occupying these states, according to the formula:

$$E = \pm\frac{\hbar^2 k^2}{2m^*} + E_0, \tag{II.1}$$

where the sign is positive for electrons in the conduction band and negative for holes in the valence band, m^* is the effective mass of the particle, and E_0 is the energy of the band at $k = 0$. At low temperatures, the effective mass interpretation of the band structure (i.e., $k \approx 0$) is generally a very reasonable approximation.

A more accurate calculation of the band structure can be obtained by diagonalizing the Luttinger-Kohn Hamiltonian. This Hamiltonian can take on various forms, depending on how many energy bands are considered. If the three

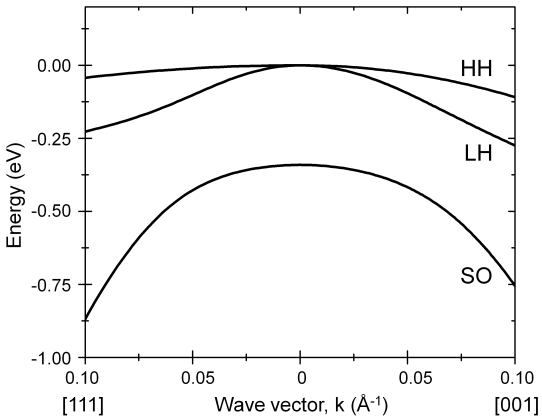

Figure 2.1 Valence band structure of bulk GaAs calculated by diagonalizing the 6×6 Luttinger-Kohn Hamiltonian. Heavy hole (HH), light hole (LH), and split-off (SO) subbands are all doubly degenerate.

valence bands are taken into account, then the Hamiltonian to be used is the 6×6 Luttinger-Kohn Hamiltonian. Six states are necessary to construct the Hamiltonian since each band is doubly degenerate in the absence of external magnetic fields and strain. Alternatively, the 4×4 Hamiltonian can be used if the split-off band is to be neglected, or the 8×8 Hamiltonian (developed by Pidgeon and Brown [24]) can be used to include the conduction band. The 6×6 Hamiltonian is sufficient for our purposes, since the conduction band makes a very small contribution in our energy range of interest.

The 6×6 Luttinger-Kohn Hamiltonian is given by:

$$H = \begin{pmatrix} P+Q & 0 & -S & R & \frac{1}{\sqrt{2}}S & \sqrt{2}R \\ 0 & P+Q & -R^\dagger & -S^\dagger & -\sqrt{2}R^\dagger & \frac{1}{\sqrt{2}}S^\dagger \\ -S^\dagger & -R & P-Q & 0 & \sqrt{2}Q & \sqrt{\frac{3}{2}}S \\ R^\dagger & -S & 0 & P-Q & -\sqrt{\frac{3}{2}}S^\dagger & \sqrt{2}Q \\ \frac{1}{\sqrt{2}}S^\dagger & -\sqrt{2}R & \sqrt{2}Q & -\sqrt{\frac{3}{2}}S & P+\Delta_{SO} & 0 \\ \sqrt{2}R^\dagger & \frac{1}{\sqrt{2}}S & \sqrt{\frac{3}{2}}S^\dagger & \sqrt{2}Q & 0 & P+\Delta_{SO} \end{pmatrix}, \tag{II.2}$$

where

$$P = \frac{\hbar^2}{2m_0}\gamma_1(k_x^2 + k_y^2 + k_z^2) \tag{II.3}$$

$$Q = \frac{\hbar^2}{2m_0}\gamma_2(k_x^2 + k_y^2 - 2k_z^2) \tag{II.4}$$

$$R = \frac{\hbar^2}{2m_0}\sqrt{3}[-\gamma_2(k_x^2 - k_y^2) + 2i\gamma_3 k_x k_y] \tag{II.5}$$

$$S = \frac{\hbar^2}{2m_0}2\sqrt{3}\gamma_3 k_z k_-. \tag{II.6}$$

Here, $k_- = k_x - ik_y$, γ_i are the Luttinger parameters, and Δ_{SO} is the energy difference between the HH/LH bands and the split-off band at $k = 0$. Given this Hamiltonian, the band structure is easily obtained by numerically solving for the energy eigenvalues for a given value of the wave vector $k = (k_x, k_y, k_z)$. This was done to obtain Fig. 2.1 using the values for GaAs, given in Table 2.1. Calculations of the band structure for semiconductor quantum wells are much more involved, and are described in detail at the end of this chapter.

	GaAs	AlAs
γ_1	6.98	3.76
γ_2	2.06	0.82
γ_3	2.93	1.42
V (eV)	-0.80	-1.33
Δ_{SO} (eV)	0.341	0.28

Table 2.1 Material parameters of GaAs and AlAs. γ_i are the Luttinger parameters, V is the valence band offset, and Δ_{SO} is the split-off band offset.

2D Electron Gas and Quasiparticles

The band structure of semiconductors is only the first of many factors which govern the dynamics of these systems. Many of the properties of semiconductors, such as conductance and optical interactions, are largely influenced by impurities, quasiparticles, and many-body interactions between free particles. In this section, we introduce the 2D electron gas (2DEG) and some relevant quasiparticles, which govern much of the dynamics of the systems in this dissertation.

2DEG

In semiconductor quantum wells, electrons which occupy the conduction band are often referred to as a two-dimensional electron gas. 2DEGs can be excited through above band gap optical excitation, where an electron in the valence band is excited to the conduction band. Such electrons quickly recombine with the hole in the valence band on a scale of ~ 1 ns. Alternatively, 2DEGs can be generated via alternative growth methods, such as modulation-doping (described in chapter IV) or by optically pumping electrons from an adjacent layer (described in chapter VI).

These methods produce longer lasting 2DEGs, which are spatially separated from hole states, and thus their optical properties can be utilized. Optical excitations of the 2DEG are characterized by trion transitions, described later.

In the spin control experiment, demonstrated in chapter IV, the electrons which compose the 2DEG store the spin information that will be controlled. In the tunneling measurements of chapter VI, the 2DEG can interact with the two-dimensional hole gas in a separate quantum well layer to alter the hole tunneling times.

Excitons

The sea of electrons and holes that can be excited in a semiconductor sample interact through Coulomb interactions and can form various quasiparticles which dictate many of the optical and electrical properties of the material. Excitons are among the most common quasiparticles in semiconductors, and are composed of a bound electron/ hole pair, similar to a hydrogen atom. Excitons can be light hole or heavy hole excitons, depending on the angular momentum of the bound hole. Many of the properties of excitons are properly predicted by making simple substitutions into the appropriate hydrogen atom equations. For example, the exciton binding energy in a bulk semiconductor is well approximated by substituting the effective masses of the electron and hole into the hydrogen binding energy equation, and multiplying the vacuum permittivity by the relevant dielectric constant:

$$E_X = -\frac{\mu e^4}{32\pi^2\hbar^2\epsilon_r^2\epsilon_0^2}, \tag{II.7}$$

where μ is the reduced mass of the electron/hole pair, e is the electric charge of a proton, and ϵ_r is the dielectric constant. For the bulk semiconductors referred to in this dissertation, the heavy hole exciton binding energies are -4.8 meV for GaAs (using the electron effective mass $0.067m_0$, heavy hole effective mass $0.51m_0$, and dielectric constant $\epsilon = 12.9$) and -6.1 meV for InP (using the electron effective mass $0.08m_0$, heavy hole effective mass $0.6m_0$, and dielectric constant $\epsilon_r = 12.5$). Here, m_0 is the true electron mass. In a similar manner, the Bohr radius can be calculated for excitons from the hydrogen atom Bohr radius equation:

$$a = \frac{4\pi\epsilon_r\epsilon_0\hbar^2}{\mu e^2}. \tag{II.8}$$

This calculation results in Bohr radii for the heavy hole exciton of 11.53 nm for GaAs and 9.37 nm for InP. Clearly, the Bohr radii of the excitonic states encompass a large number of lattice sites, since the lattice constants for GaAs and InP are 5.653 Å and 5.8687 Å, respectively. Excitons with a Bohr radius larger than the lattice spacing of the host material are known as Wannier excitons [25].

The exciton binding energy is more difficult to calculate in quantum wells due to the spatial confinement. It is generally accomplished by applying the variational principle. A very good summary of this method as applied to excitonic states is found in *Quantum Wells, Wires, and Dots*, by Paul Harrison [23].

Trions

Another quasiparticle of particular interest is the trion, also known as the negatively charged exciton, which is composed of two electrons of opposite spin

bound to a hole, similar to a negative hydrogen ion. Positively charged trions also exist, composed of one electron and two holes, although they will not be discussed in this dissertation since our samples are not constructed to support the formation of the positively charged version. We will use the word trion to refer to the negatively charged version. Trion formation requires the presence of excess electrons in the conduction band. An appropriate density of excess electrons can be provided through modulation-doping, or photo-injection from other layers, as described in chapters IV and VI, respectively. Trion binding energies are larger than exciton binding energies in the same material, and are generally calculated via the variational principle.

The excitation of a 2DEG is characterized by the trion energy level. In the absence of an external magnetic field, the transition scheme for trion excitation from an electron ground state in the 2DEG is shown in Fig. 2.2b. A photon of circular polarization can create an electron/ hole pair which binds to a free electron in the 2DEG to form a trion. In a quantum well, the spin states are quantized along the confinement direction, which we label as the z-axis. In forming a trion, the two electron spins form a singlet state, and thus the hole spin determines the total spin. $\sigma+$ ($\sigma-$) polarized photons excite an electron with $J_z = +\frac{1}{2}$ ($-\frac{1}{2}$) to the trion state, with total spin $J_z = +\frac{3}{2}$ ($-\frac{3}{2}$).

In the presence of an external magnetic field in the x-direction (Voigt geometry, see Fig. 2.2a), the degeneracy of the 2DEG spin states is lifted via the Zeeman

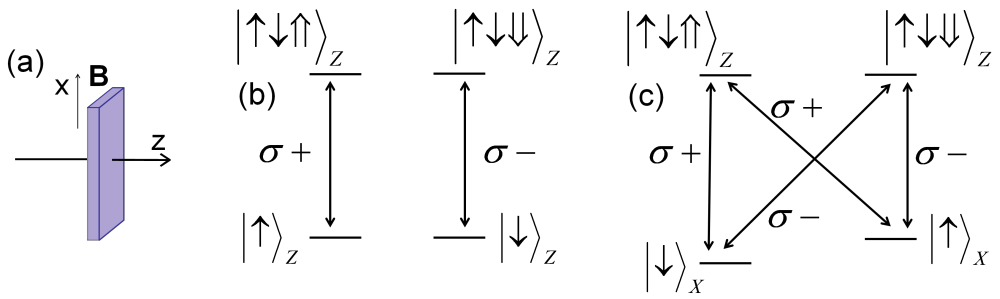

Figure 2.2 Trion transition scheme. (a) Definition of axes relative to sample growth direction and magnetic field (Voigt geometry). (b) Trion transition scheme with 2DEG ground states in the absence of magnetic field. (c) Trion transition scheme in the presence of magnetic field.

effect and the spin states become quantized along the magnetic field direction, as shown in Fig. 2.2c. Generally, the hole spin states do not become quantized along the magnetic field direction because the confinement of the quantum well competes with the quantization of the magnetic field [26], and is the dominant factor for quantum wells of typical widths. Therefore, in the presence of a magnetic field, the energy eigenstates of the 2DEG are quantized along the x-direction, while the energy eigenstates of the trion are quantized along the z-direction. We will return to this picture in chapter IV, when the trion transitions are used to manipulate the spin state of the 2DEG.

Donor and Acceptor Impurities

Donor and acceptor impurities can also greatly affect the behavior of a semiconductor. These are atoms which replace one of the constituent atoms of the material, and have either one electron more (donor), or one electron less (acceptor), in their valence shell. We will focus solely on donor impurities, since they are

relevant to the material of chapter V. At low temperatures, the extra electron remains bound to the donor impurity. This donor site can then attract excitons through the van der Waals interaction, and form a four particle bound state, known as a donor-bound exciton, which consists of two electrons of opposite spin, a positively charged hole, and the positively charged nucleus. The energy structure of this four particle complex is much more complicated than the analogous hydrogen molecule, and a full theoretical treatment of its properties remains to be completed. These particles will be elaborated on in chapter V.

Quantum Well Band Structure

In a semiconductor quantum well, the degeneracy of the light hole and heavy hole valence bands is lifted at k = 0 due to the confinement potential. Additionally, the spacial confinement leads to quantization of the wave vector along the confinement direction, leading to a series of valence bands, which are now superposition states of light hole, heavy hole, and split-off band states. In this case, the valence bands are labeled as either a light or heavy hole subband based on their angular momentum properties at $k = 0$. A representative diagram is shown in 2.3, although this figure can be dramatically altered for different materials and quantum well thicknesses.

Calculations of band structure are much more difficult in quantum wells because of the imposed boundary conditions and because of the wave vector quantization.

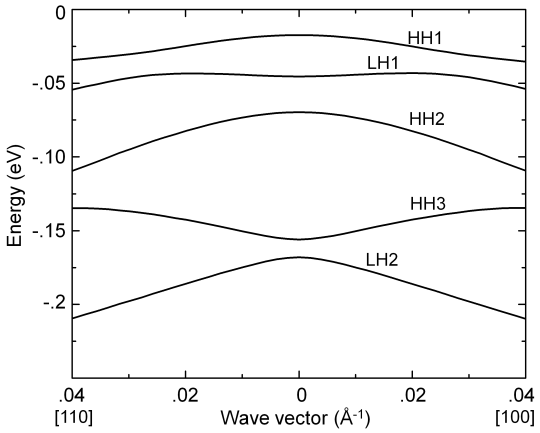

Figure 2.3 Valence band structure of a 68 Å GaAs/ AlAs quantum well, calculated using the transfer matrix method.

A technique known as the transfer matrix method can be used to overcome these difficulties, which will be described here in detail since results of the calculation will be necessary for the discussion on tunneling in chapter VI.

The valence band structure of a semiconductor quantum well can be calculated using various techniques. The calculation used for this dissertation follows the treatment described in *Quantum Wells, Wires, and Dots* by Paul Harrison [23]. Please see that book for more details. It makes use of the 6 X 6 Luttinger-Kohn Hamiltonian derived from k·p perturbation theory and the transfer matrix method. Note, this calculation is in the inverted energy picture, so the final result for the valence band energies must be multiplied by -1 to obtain the final answer.

The goal is to solve for the transfer matrix $\mathbf{T}$ of the quantum well system. Consider a single quantum well surrounded by barriers of finite height and infinite extent. Beginning in layer j, propagate the state through to the barrier/

well boundary using the propagation matrix $\mathbf{D_j}$. Propagate the state across the boundary by changing bases with the matrix $\mathbf{U_j}$, then matching boundary conditions with the matrix $\mathbf{I_{j+1}^{-1}I_j}$, and finally changing back to the original basis. The transfer matrix moving from layer j to layer $j+1$ is then given by:

$$\mathbf{T^{j,j+1}} = \mathbf{U_{j+1}^{-1}I_{j+1}^{-1}I_jU_jD_j}, \tag{II.9}$$

and the total transfer matrix is given by:

$$\mathbf{T} = \mathbf{T^{0,1}T^{1,2}\cdots T^{N-1,N}}. \tag{II.10}$$

The form of the above matrices will depend on the Hamiltonian used. $\mathbf{D}$ is a diagonal vector of eigenvalues, and $\mathbf{U}$ is a matrix of eigenvectors. The method of solving for these eigenvalues and eigenvectors follows below.

The 6 X 6 Luttinger-Kohn Hamiltonian in the basis $|F_i\rangle$ can be written in the block-diagonal form [23]:

$$H = \begin{pmatrix} H_+ & 0 \\ 0 & H_- \end{pmatrix}, \tag{II.11}$$

where the basis vectors $|F_i\rangle$ are superpositions of the eigenstates of the angular

momentum operator $|J, m_J\rangle$ (eigenvalues J and z-axis projections m_J):

$$|F_1\rangle = \alpha|3/2, -3/2\rangle - \alpha^*|3/2, 3/2\rangle \tag{II.12}$$

$$|F_2\rangle = \beta|3/2, 1/2\rangle + \beta^*|3/2, -1/2\rangle \tag{II.13}$$

$$|F_3\rangle = \beta|1/2, 1/2\rangle + \beta^*|1/2, -1/2\rangle \tag{II.14}$$

$$|F_4\rangle = \alpha|3/2, -3/2\rangle + \alpha^*|3/2, 3/2\rangle \tag{II.15}$$

$$|F_5\rangle = \beta|3/2, 1/2\rangle - \beta^*|3/2, -1/2\rangle \tag{II.16}$$

$$|F_6\rangle = \beta|1/2, 1/2\rangle - \beta^*|1/2, -1/2\rangle, \tag{II.17}$$

and the 3 X 3 Hamiltonians are given by

$$H_{\pm} = \begin{pmatrix} P+Q+V & R \mp \imath S & \sqrt{2}R \pm \imath S/\sqrt{2} \\ R \pm \imath S^{\dagger} & P-Q \mp \imath C+V & \sqrt{2}Q \mp \imath\sqrt{3/2}\Sigma \\ \sqrt{2}R \mp \imath S^{\dagger}/\sqrt{2} & \sqrt{2}Q \pm \imath\sqrt{3/2}\Sigma^{\dagger} & P+\Delta_{SO} \pm \imath C+V \end{pmatrix}, \tag{II.18}$$

with

$$P = (\frac{\hbar^2}{2m_0})\gamma_1(k_x^2 + k_y^2 + k_z^2), \tag{II.19}$$

$$Q = (\frac{\hbar^2}{2m_0})\gamma_2(k_x^2 + k_y^2 - 2k_z^2), \tag{II.20}$$

$$R = -\sqrt{3}(\frac{\hbar^2}{2m_0})\gamma_\phi k_\parallel^2, \tag{II.21}$$

$$S = 2\sqrt{3}(\frac{\hbar^2}{2m_0})k_\parallel[(\sigma - \delta)k_z + k_z\pi], \tag{II.22}$$

$$\Sigma = 2\sqrt{3}(\frac{\hbar^2}{2m_0})k_\parallel[\frac{1}{3}(\sigma - \delta) + \frac{2}{3}\pi]k_z + k_z[\frac{2}{3}(\sigma - \delta) + \frac{1}{3}\pi], \tag{II.23}$$

$$C = 2(\frac{\hbar^2}{2m_0})k_\parallel[k_z(\sigma - \delta - \pi) - (\sigma - \delta - \pi)k_z], \tag{II.24}$$

$$\gamma_\phi = \sqrt{\bar{\gamma}^2 + \mu^2 - 2\bar{\gamma}\mu\cos\phi}, \qquad k_\parallel^2 = k_x^2 + k_y^2, \tag{II.25}$$

$$\bar{\gamma} = \frac{1}{2}(\gamma_2 + \gamma_3), \qquad \mu = \frac{1}{2}(\gamma_3 - \gamma_2), \tag{II.26}$$

$$\sigma = \bar{\gamma} - \frac{1}{2}\delta, \qquad \pi = \mu + \frac{3}{2}\delta, \qquad \delta = \frac{1}{9}(1 + \gamma_1 + \gamma_2 - 3\gamma_3). \tag{II.27}$$

γ_i are the Luttinger parameters, V and Δ_{SO} are the valence band offset and spin-orbit splitting, respectively, and k_i are the wave vector components. The values of these parameters for GaAs and AlAs are given in Table 2.1.

In the absence of applied electric fields, and assuming the quantum well is symmetric, the upper and lower Hamiltonians $\mathbf{H}_\pm$ will produce degenerate band structures. Thus, a complete solution of the band structure will follow from solving only the upper Hamiltonian.

Assume the bound state energy E is known and solve for the eigenvalues k_z and

eigenvectors of the following matrix:

$$\begin{pmatrix} 0 & 1 \\ -H_2^{-1}(H_0 - E) & -H_2^{-1}H_1 \end{pmatrix} \begin{pmatrix} u \\ k_z u \end{pmatrix} = k_z \begin{pmatrix} u \\ k_z u \end{pmatrix}. \tag{II.28}$$

The $\mathbf{H_i}$ are the components of the Hamiltonian of different orders in k_z:

$$[\mathbf{H}] = [\mathbf{H_2 k_z^2} + \mathbf{H_1 k_z} + \mathbf{H_0}]. \tag{II.29}$$

For the upper 3 X 3 Hamiltonian, these matrices are given by:

$$\mathbf{H_2} = \begin{pmatrix} (\gamma_1 - 2\gamma_2) & 0 & 0 \\ 0 & (\gamma_1 + 2\gamma_2) & -2\sqrt{2}\gamma_2 \\ 0 & -2\sqrt{2}\gamma_2 & \gamma_1 \end{pmatrix} \tag{II.30}$$

$$\mathbf{H_1} = \begin{pmatrix} 0 & \mp\imath 2\sqrt{3}\gamma_3 k_\parallel & \pm\imath\sqrt{6}\gamma_3 k_\parallel \\ \pm\imath 2\sqrt{3}k_\parallel & 0 & \mp\imath 3\sqrt{2}\gamma_3 k_\parallel \\ \mp\imath\sqrt{6}\gamma_3 k_\parallel & \pm\imath 3\sqrt{2}\gamma_3 k_\parallel & 0 \end{pmatrix} \tag{II.31}$$

$$\mathbf{H_0} = \begin{pmatrix} (\gamma_1 + \gamma_2)k_\parallel^2 + V & -\sqrt{3}\gamma_\phi k_\parallel^2 & -\sqrt{6}\gamma_\phi k_\parallel^2 \\ -\sqrt{3}\gamma_\phi k_\parallel^2 & (\gamma_1 - \gamma_2) + V & \sqrt{2}\gamma_2 k_\parallel^2 \\ -\sqrt{6}\gamma_\phi k_\parallel^2 & \sqrt{2}\gamma_2 k_\parallel^2 & \gamma_1 k_\parallel^2 + \Delta_{SO} + V \end{pmatrix}. \tag{II.32}$$

From here, the procedure is to find the eigenvalues k_z of the matrix on the left hand side of (II.28) using standard numerical methods. The eigenvalues must be categorized into forward and backward moving states. An array containing unsorted eigenvalues can be sorted by multiplying them by $-\imath$, sorting the real part of the result in descending order, then multiplying the vector by $\imath$ to recover their original values. The eigenvectors must be organized into the same order as their corresponding eigenvalues. Once the ordering is done correctly, define the

propagation matrix $\mathbf{D}$ as:

$$\mathbf{D} = \begin{pmatrix} e^{\imath k_{z1} z} & 0 & 0 & 0 & 0 & 0 \\ 0 & e^{\imath k_{z2} z} & 0 & 0 & 0 & 0 \\ 0 & 0 & e^{\imath k_{z3} z} & 0 & 0 & 0 \\ 0 & 0 & 0 & e^{\imath k_{z4} z} & 0 & 0 \\ 0 & 0 & 0 & 0 & e^{\imath k_{z5} z} & 0 \\ 0 & 0 & 0 & 0 & 0 & e^{\imath k_{z6} z} \end{pmatrix}, \tag{II.33}$$

and the eigenvector matrix as:

$$\mathbf{U} = \begin{pmatrix} \vec{u_1} & \vec{u_2} & \vec{u_3} & \vec{u_4} & \vec{u_5} & \vec{u_6} \end{pmatrix}, \tag{II.34}$$

where $\vec{u_i}$ are the eigenvectors where their bottom three components have been multiplied by $\imath$.

The final required matrix is the boundary matching matrix $\mathbf{I}$, given by:

$$\mathbf{I} = \begin{pmatrix} \mathbf{1} & \mathbf{0} \\ \mathbf{B_1} & \mathbf{B_2} \end{pmatrix}, \tag{II.35}$$

where

$$\mathbf{B_1} = \begin{pmatrix} 0 & 2\sqrt{3}\pi k_{\|} & -\sqrt{6}\pi k_{\|} \\ -2\sqrt{3}(\sigma - \delta)k_{\|} & (\sigma - \delta - \pi)k_{\|} & \sqrt{2}(2\sigma - 2\delta + \pi)k_{\|} \\ \sqrt{6}(\sigma - \delta)k_{\|} & -\sqrt{2}(\sigma - \delta + 2\pi)k_{\|} & -2(\sigma - \delta - \pi)k_{\|} \end{pmatrix} \tag{II.36}$$

$$\mathbf{B_2} = \begin{pmatrix} \gamma_1 - 2\gamma_2 & 0 & 0 \\ 0 & \gamma_1 + 2\gamma_2 & -2\sqrt{2}\gamma_2 \\ 0 & -2\sqrt{2}\gamma_2 & \gamma_1 \end{pmatrix}. \tag{II.37}$$

For a quantum well of finite barrier heights, the matrices must be found for both the barrier and the well materials separately, using the appropriate constants for each material (Luttinger parameters γ_i, Δ_{SO}, etc.). The potential height V to be used is $V = 0$ for the well, and for the barrier $V = \Delta V$ is the difference between

valence band offsets of the materials (it is a positive number in the inverted energy picture).

For a single quantum well, the barriers are given by layers $j = 1, 3$ and the well is layer $j = 2$. With this notation, the total transfer matrix is:

$$\mathbf{T} = \mathbf{U_3^{-1}I_3^{-1}I_2U_2D_2U_2^{-1}I_2^{-1}I_1U_1}. \tag{II.38}$$

The propagation distance within the barriers can be taken to be zero [27], and thus the propagation matrices for the barriers reduce to the identity and do not appear in the transfer matrix above.

Having obtained the transfer matrix, it can be divided into four 3 X 3 blocks:

$$\mathbf{T} = \begin{pmatrix} \mathbf{T_{11}} & \mathbf{T_{12}} \\ \mathbf{T_{21}} & \mathbf{T_{22}} \end{pmatrix}. \tag{II.39}$$

Bound state energies of the quantum well correspond to energies which result in $det(\mathbf{T_{22}}) = \mathbf{0}$, since these correspond to wavefunctions which decay at infinity. These values are generally plotted as a function of k_x and k_y along a certain direction (i.e. $k_y = 0$ or $k_x = k_y$). Such a plot is shown in Fig. 2.3, which reproduces the results published by A. M. Malik *et al.* [28] as a check to ensure that the calculation was performed correctly. The band structure of our mixed-type quantum well sample of chapter VI was calculated using this technique, and the corresponding Matlab script is given in appendix B.

CHAPTER III

THEORY OF ULTRAFAST OPTICAL SPIN CONTROL

Overview

Many different optical spin control mechanisms have been proposed, all of which are equally valid in the ideal case [20, 29–32]. However, semiconductors are subject to many complications which cannot be ignored due to many-body interactions. As a result, not all spin control techniques are equally viable. Rotations must be performed on a time scale faster than relevant decay rates, and optical pulses must not interact strongly with nearby resonances. The method presented in this dissertation was chosen with these issues in mind.

The simplest spin control mechanism is through direct excitation of the spin up to spin down transition. An on-resonant electric field can induce Rabi oscillations between the spin states, as is commonly described in optics textbooks [32]. However, the energy splitting of the spin states under relatively high magnetic fields is on the order of 0.1 meV in semiconductors. Therefore, on-resonant electric fields lie in the microwave regime, and pulses must be produced using electronic devices. Unfortunately, electronics are limited to timescales of $\sim$ 10 nanoseconds (ns). In semiconductor quantum wells, spin lifetimes are on the order of 10 ns, making

electronic control practically useless. In semiconductor quantum dots, where spin lifetimes can be much longer ($\sim$ ms), such a control scheme may have a practical purpose, as has been demonstrated experimentally [8]. The fidelity of such rotations will be limited due to dipole decoherence during the duration of the pulse, and can be improved dramatically by moving to the picosecond (ps) timescale.

Other proposed spin control mechanisms rely on real or virtual population transfer of the ground state electrons through an excited state in what is commonly described as a Λ-system, as shown in Fig. 3.1a. An elegant solution of this system, proposed by P. Chen *et al.* [29], utilizes two electric fields which couple separately to the two optical transitions. It was theoretically demonstrated that this control scheme would allow spin rotations about any arbitrary axis. The downside is that the two electric fields must have narrow bandwidths, and hence long pulse durations. Although the long pulse duration is a negative factor in this control scheme, the benefit of the ability to use narrow bandwidth pulses may outweigh the cons. Such a control mechanism was recently demonstrated by Timothy Sweeney *et al.* [33] in the same CdTe quantum well sample used in chapter IV.

A spin control mechanism based on temporally short pulses was proposed by S. Economou *et al.* [30] in which a single, spectrally broad electrical field is coupled to both transitions of the Λ-system. An on-resonant pulse of area 2π would result in a spin rotation about the growth axis of the sample (perpendicular to the magnetic field). On-resonant pulses are highly unfavorable due to the fast dipole decoherence

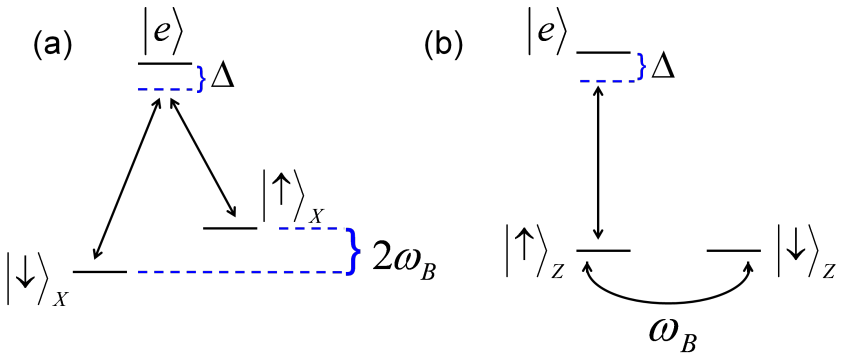

Figure 3.1 Two equivalent energy level diagrams, written in different bases. (a) Λ-system: electron spin states written in the x-basis, where the external magnetic field is along the x-direction. (b) L-system: electron spin states written in the z-basis, the sample growth direction. Δ is the electric field detuning.

rate of the 2DEG system ($\sim$ 2 ps) [17]. Although the proposed scheme focused primarily on on-resonant pulses, the technique can be extended to off-resonant pulses where the the trion transition is only virtually excited.

As pointed out in the same paper by S. Economou *et al.*, the Λ-system can be rewritten in the z-basis (sample growth direction), resulting in what we call the L-system, as shown in Fig. 3.1b. In this basis, the magnetic field along the x-direction causes population to precess between the spin states in the z-basis at the Larmor precession frequency ω_B. The L-system is a convenient picture for describing spin control since it has only one allowed optical transition. Here, an on-resonant pulse will induce Rabi oscillations between one of the electron ground states and the excited state. A 2π pulse will induce one full Rabi oscillation resulting in an accumulated minus sign in the phase between the electron ground states. The minus sign is equivalent to a full electron spin rotation about the z-axis. Again,

on-resonant pulses are highly unfavorable, but the theory can be extended to off-resonant pulses. Below resonance, the applied electric field induces an optical Stark shift of the optically active electron ground state energy level, resulting in a splitting $\delta\omega$ of the electron ground states [20], as shown in Fig. 3.2. This energy splitting can be viewed as an effective magnetic field along the z-axis, which causes the electron spin to precess about the z-axis, and the total rotation angle about the z-axis is given by the integral of the time dependent optical Stark shift:

$$\phi = \int \delta\omega(t)dt. \tag{III.1}$$

.

The L-system is our picture of choice. It allows for temporally short pulses, which can be shorter than relevant decay times within the sample, and it provides us with a tool for monitoring the effectiveness of our optical pulse. In other words,

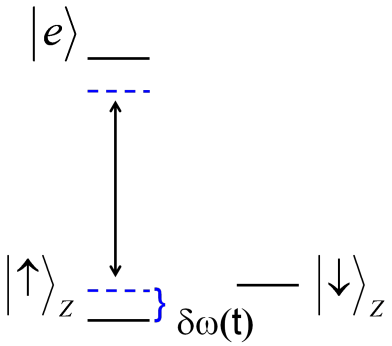

Figure 3.2 Diagram demonstrating Stark shift induced energy splitting $\delta\omega$(t) by an applied, below-resonance, optical field.

we know the pulse can induce π rotations only if a large enough Stark shift is manifest in our absorption data.

Bloch Sphere

Here we introduce the notion of the Bloch sphere, which relates the density matrix elements to the orientation of the spin polarization. The Bloch sphere often helps one to visualize the dynamics of a two-level system. In the z-basis, the density matrix is given by:

$$\rho = \begin{pmatrix} \rho_{\uparrow\uparrow} & \rho_{\uparrow\downarrow} \\ \rho_{\downarrow\uparrow} & \rho_{\downarrow\downarrow} \end{pmatrix}, \tag{III.2}$$

with $\rho^*_{\downarrow\uparrow} = \rho_{\uparrow\downarrow}$. The density matrix elements can be related to the spacial orientation of the electron spin by determining the ensemble averages of the spin operators in each direction. In the z-basis, the spin operators are given by [34]:

$$S_x = \frac{\hbar}{2}\begin{pmatrix} 0 & 1 \\ 1 & 0 \end{pmatrix}, \qquad S_y = \frac{\hbar}{2}\begin{pmatrix} 0 & -i \\ i & 0 \end{pmatrix}, \qquad S_z = \frac{\hbar}{2}\begin{pmatrix} 1 & 0 \\ 0 & -1 \end{pmatrix}. \tag{III.3}$$

The ensemble average of an operator A is given by [34]:

$$[A] = Tr(\rho A), \tag{III.4}$$

where Tr is the trace of a matrix. Computing the ensemble averages of the spin operators, we find:

$$[S_x] = \frac{\hbar}{2}(\rho_{\uparrow\downarrow} + \rho_{\downarrow\uparrow}) = \hbar Re(\rho_{\uparrow\downarrow}) \tag{III.5}$$

$$[S_y] = \frac{i\hbar}{2}(\rho_{\uparrow\downarrow} - \rho_{\downarrow\uparrow}) = -\hbar Im(\rho_{\uparrow\downarrow}) \tag{III.6}$$

$$[S_z] = \frac{\hbar}{2}(\rho_{\uparrow\uparrow} - \rho_{\downarrow\downarrow}). \tag{III.7}$$

The Bloch sphere represents the ensemble average of the electron spin in each dimension, normalized such that the magnitude of the Bloch vector is unity when the density matrix is normalized to unity in the following manner:

$$\langle x\rangle = \frac{2}{\hbar}[S_x] = 2Re(\rho_{\uparrow\downarrow}), \qquad \langle y\rangle = \frac{2}{\hbar}[S_y] = 2Im(\rho_{\uparrow\downarrow}), \qquad \langle z\rangle = \frac{2}{\hbar}[S_z] = \rho_{\uparrow\uparrow} - \rho_{\downarrow\downarrow}. \tag{III.8}$$

Using the optical Bloch equations, the density matrix elements can be found as a function of time and related to the direction of the spin polarization using the notion of the Bloch sphere. In our experiments, described in chapter IV, a magnetic field along the x-direction causes the electron spins to precess about the x-axis. We then measure the z-projection of the electron spin polarization. Visualizing these dynamics using the Bloch sphere is helpful, since we can imagine the Bloch vector precessing about the x-axis, and relate the z-axis projection of the Bloch vector to the measured signal.

Hamiltonian

To solve for the time-dependent dynamics of the spin polarization, we must first define the Hamiltonian for the system. Here, we go through the derivation of the Hamiltonian in detail, in a manner similar to derivations that can be found in numerous sources [35].

Consider the Λ-system of Fig. 3.1a, where a magnetic field applied along the x-axis induces a splitting of the electron spin ground states by an energy $2\hbar\omega_B$. In

the absence of an applied electric field, the unperturbed Hamiltonian H_0 is simply

$$H_0 = -\hbar\,\omega_B|\uparrow\rangle_X\langle\uparrow|_X + \hbar\,\omega_B|\downarrow\rangle_X\langle\downarrow|_X + \hbar\,\omega_0|e\rangle\langle e|, \tag{III.9}$$

where the zero of energy is defined as the middle of the electron ground states. The interaction Hamiltonian is given by

$$H_I = \frac{\hbar\,\Omega}{2}(e^{i\omega t} + e^{-i\omega t})(|\downarrow\rangle_X\langle e| + |e\rangle\langle\downarrow|_X + |\uparrow\rangle_X\langle e| + |e\rangle\langle\uparrow|_X), \tag{III.10}$$

where ω is the field frequency and $\Omega = -\dfrac{\mu E}{\hbar}$ is the Rabi frequency. The dipole transition strength μ is assumed to be the same for both transitions. Change to the z-basis by making the transformations:

$$|\uparrow\rangle_X = \frac{1}{\sqrt{2}}(|\uparrow\rangle_Z + |\downarrow\rangle_Z) \tag{III.11}$$

$$|\downarrow\rangle_X = \frac{1}{\sqrt{2}}(|\uparrow\rangle_Z - |\downarrow\rangle_Z). \tag{III.12}$$

After canceling like terms, the unperturbed Hamiltonian becomes

$$H_0 = -\hbar\,\omega_B|\uparrow\rangle_Z\langle\downarrow|_Z - \hbar\,\omega_B|\downarrow\rangle_Z\langle\uparrow|_Z + \hbar\,\omega_0|\,e\rangle\langle e|, \tag{III.13}$$

and the interaction Hamiltonian becomes

$$H_I = \frac{\hbar\,\Omega}{\sqrt{2}}(e^{i\omega t} + e^{-i\omega t})(|\uparrow\rangle_Z\langle e| + |\,e\rangle\langle\uparrow|_Z). \tag{III.14}$$

Rewriting the Hamiltonian in matrix form, in the basis $\{|\downarrow\rangle_Z, |\uparrow\rangle_Z, |\,e\rangle\}$, we have

$$H = \hbar\begin{pmatrix} 0 & -\omega_B & 0 \\ -\omega_B & 0 & \dfrac{\Omega}{\sqrt{2}}(e^{i\omega t} + e^{-i\omega t}) \\ 0 & \dfrac{\Omega}{\sqrt{2}}(e^{i\omega t} + e^{-i\omega t}) & \omega_0 \end{pmatrix}. \tag{III.15}$$

The L-system of the previous section, shown in Fig. 3.1b is described by this Hamiltonian. The diagonal elements depict a three level system at which the $|\uparrow\rangle_z$ and $|\downarrow\rangle_z$ states are at energy zero, and the excited state $|e\rangle$ is at energy $\hbar\omega_0$. The $|\uparrow\rangle_z$ and $|\downarrow\rangle_z$ states are coupled by a field of frequency ω_B and the $|\uparrow\rangle_z$ ground state is the only ground state which couples to $|e\rangle$ through the applied electric field of Rabi frequency Ω.

By making a change to the rotating frame, which is convenient for numerical applications, and using the rotating wave approximation, the Hamiltonian can be reduced to:

$$H = \hbar \begin{pmatrix} 0 & -\omega_B & 0 \\ -\omega_B & 0 & \frac{\Omega}{\sqrt{2}} \\ 0 & \frac{\Omega}{\sqrt{2}} & \Delta \end{pmatrix}, \tag{III.16}$$

where $\Delta = \omega - \omega_0$ is the electric field detuning. The justification for this simplified form of the Hamiltonian requires knowledge of which terms can be dropped from the equations of motion. At this point, it is not apparent based on the Hamiltonian alone. However, justification will be given in the upcoming section titled "Optical Bloch Equations". We state its form here so that it can be used to demonstrate the optical Stark effect in this system.

Optical Stark Shift

The fact that the control pulse induces a Stark shift of one ground state relative to the other can be seen in the adiabatic limit in which the change in the excited

state population is assumed to be slow, i.e. $\frac{\partial c_e}{\partial t} = 0$, where c_e is the excited state coefficient, which is valid in the large detuning regime [31]. In the adiabatic limit, the three-level system can be reduced to an effective two-level system, as shown below.

We find the time dependence of the system by applying the Schrödinger equation:

$$i\hbar \begin{pmatrix} \dot{c}_\downarrow \\ \dot{c}_\uparrow \\ \dot{c}_e \end{pmatrix} = \begin{pmatrix} 0 & -\omega_B & 0 \\ -\omega_B & 0 & \frac{\Omega}{\sqrt{2}} \\ 0 & \frac{\Omega}{\sqrt{2}} & \Delta \end{pmatrix} \begin{pmatrix} c_\downarrow \\ c_\uparrow \\ c_e \end{pmatrix}, \tag{III.17}$$

which results in the following coupled equations for the wavefunction coefficients:

$$i\hbar \dot{c}_\downarrow = -\omega_B c_\uparrow \tag{III.18}$$

$$i\hbar \dot{c}_\uparrow = -\omega_B c_\downarrow + \frac{\Omega}{\sqrt{2}} c_e \tag{III.19}$$

$$i\hbar \dot{c}_e = \frac{\Omega}{\sqrt{2}} c_\uparrow + \Delta c_e. \tag{III.20}$$

In the adiabatic limit, the time derivative of the excited state is assumed to be zero. This allows us to use the third equation in the series above to solve for the steady state value of c_e:

$$c_e = -\frac{\Omega}{\sqrt{2}\Delta} c_\uparrow. \tag{III.21}$$

Replacing this value of c_e in the other two equations, we obtain coupled equations between the coefficients of the two ground state energy levels. Written in matrix

form, we have:

$$i\hbar \begin{pmatrix} \dot{c}_\downarrow \\ \dot{c}_\uparrow \end{pmatrix} = \begin{pmatrix} 0 & -\omega_B \\ -\omega_B & -\dfrac{\Omega^2}{2\Delta} \end{pmatrix} \begin{pmatrix} c_\downarrow \\ c_\uparrow \end{pmatrix}. \tag{III.22}$$

In this form, it is evident that the system has been reduced to a two-level system, with energies given by the diagonal components of the two-level Hamiltonian. In this case, the optically active ground state energy level in the three-level system has been shifted by an amount $-\dfrac{\Omega^2}{2\Delta}$, while the optically inert energy level remains at its previous energy of zero. The shifted energy level will accumulate phase while the optical pulse is applied. The total phase accumulated is equivalent to a rotation of the electron spin by the same angle, which is given by:

$$\phi = \int \frac{\Omega(t)^2}{2\Delta} dt. \tag{III.23}$$

A complete spin flip occurs when $\phi = \pi$. For far off-resonant pulses, where Δ is large, the optical pulse intensity, $I \sim \Omega^2$, must be adequately large, or else the pulse duration must be sufficiently long.

Optical Bloch Equations

The adiabatic limit is extremely useful when it comes to giving us a physical picture of the Stark shift induced spin rotation. However, the requirement of a large detuning may not be attainable for the chosen system. A more thorough treatment of the spin rotation scheme can be obtained through the optical Bloch equations (OBE). The OBE will take into account the adverse effects of excited

state excitation. As we shall see in chapter IV, through experimentation, the OBE predict the experimental results quite well.

The OBE for the L-system can be derived using the Liouville equation

$$\dot{\rho} = -\frac{i}{\hbar}[H, \rho]. \tag{III.24}$$

where ρ is the density matrix

$$\rho \equiv \begin{pmatrix} \rho_{\downarrow\downarrow} & \rho_{\downarrow\uparrow} & \rho_{\downarrow e} \\ \rho_{\uparrow\downarrow} & \rho_{\uparrow\uparrow} & \rho_{\uparrow e} \\ \rho_{e\downarrow} & \rho_{e\uparrow} & \rho_{ee} \end{pmatrix}, \tag{III.25}$$

where $\uparrow$ represents the +z direction, and $\downarrow$ the -z direction. After performing the matrix multiplication of the Liouville equation and equating matrix elements, one obtains the following coupled differential equations:

$$\dot{\rho}_{\downarrow\downarrow} = -i\omega_B \rho_{\downarrow\uparrow} + c.c. = 2\omega_B Im[\rho_{\downarrow\uparrow}] \tag{III.26}$$

$$\dot{\rho}_{\uparrow\uparrow} = i\omega_B \rho_{\downarrow\uparrow} - i\frac{\Omega}{\sqrt{2}}(e^{i\omega t} + e^{-i\omega t})\rho_{e\uparrow} \tag{III.27}$$

$$= 2Im[-\omega_B \rho_{\downarrow\uparrow} + \frac{\Omega}{\sqrt{2}}(e^{i\omega t} + e^{-i\omega t})\rho^*_{\uparrow e}] \tag{III.28}$$

$$\dot{\rho}_{\downarrow\uparrow} = i\omega_B(\rho_{\uparrow\uparrow} - \rho_{\downarrow\downarrow}) + i\frac{\Omega}{\sqrt{2}}(e^{i\omega t} + e^{-i\omega t})\rho_{\downarrow e} \tag{III.29}$$

$$\dot{\rho}_{\downarrow e} = i\omega_B \rho_{\uparrow e} + i\omega_0 \rho_{\downarrow e} + i\frac{\Omega}{\sqrt{2}}(e^{i\omega t} + e^{-i\omega t})\rho_{\downarrow\uparrow} \tag{III.30}$$

$$\dot{\rho}_{\uparrow e} = i\omega_B \rho_{\downarrow e} + i\omega_0 \rho_{\uparrow e} + i\frac{\Omega}{\sqrt{2}}(e^{i\omega t} + e^{-i\omega t})(2\rho_{\uparrow\uparrow} + \rho_{\downarrow\downarrow} - 1). \tag{III.31}$$

The relations $\rho_{ij} = \rho^*_{ji}$ and $\rho_{\downarrow\downarrow} + \rho_{\uparrow\uparrow} + \rho_{ee} = 1$ were used above to eliminate redundant matrix elements. Numerical computations will be made easier by going

into the rotating frame by defining

$$c_e = \tilde{c}_e e^{i\omega t} \tag{III.32}$$

$$\rho_{\downarrow e} = c_\downarrow^* c_e = c_\downarrow^* \tilde{c}_e e^{i\omega t} = \tilde{\rho}_{\downarrow e} e^{i\omega t} \tag{III.33}$$

$$\rho_{\uparrow e} = \tilde{\rho}_{\uparrow e} e^{i\omega t} \tag{III.34}$$

The above set of differential equations then become

$$\dot{\rho}_{\downarrow\downarrow} = 2\omega_B Im[\rho_{\downarrow\uparrow}] \tag{III.35}$$

$$\dot{\rho}_{\uparrow\uparrow} = 2Im[-\omega_B \rho_{\downarrow\uparrow} + \frac{\Omega}{\sqrt{2}}(1 + e^{-2i\omega t})\tilde{\rho}_{\uparrow e}^*] \tag{III.36}$$

$$\dot{\rho}_{\downarrow\uparrow} = i\omega_B(\rho_{\uparrow\uparrow} - \rho_{\downarrow\downarrow}) + i\frac{\Omega}{\sqrt{2}}(1 + e^{2i\omega t})\tilde{\rho_{\downarrow e}} \tag{III.37}$$

$$\dot{\tilde{\rho}}_{\downarrow e} = \frac{\partial}{\partial t}(\rho_{\downarrow e} e^{-i\omega t}) \tag{III.38}$$

$$= i\omega_B \tilde{\rho}_{\uparrow e} - i\Delta\tilde{\rho_{\downarrow e}} + i\frac{\Omega}{\sqrt{2}}(1 + e^{-2i\omega t})\rho_{\downarrow\uparrow} \tag{III.39}$$

$$\dot{\tilde{\rho}}_{\uparrow e} = \frac{\partial}{\partial t}(\rho_{\uparrow e} e^{-i\omega t}) \tag{III.40}$$

$$= i\omega_B \tilde{\rho}_{\downarrow e} - i\Delta\tilde{\rho}_{\uparrow e} + i\frac{\Omega}{\sqrt{2}}(1 + e^{-2i\omega t}(2\rho_{\uparrow\uparrow} + \rho_{\downarrow\downarrow} - 1) \tag{III.41}$$

where $\Delta = \omega - \omega_0$ is the field detuning. Finally, we make the rotating wave approximation by eliminating fast oscillating terms $\propto e^{2i\omega t}$, and add phenomenological decay terms, to obtain the final forms of the differential

equations:

$$\dot{\rho}_{\downarrow\downarrow} = 2\omega_B Im[\rho_{\downarrow\uparrow}] + \frac{\Gamma}{2}(1 - \rho_{\downarrow\downarrow} - \rho_{\uparrow\uparrow}) \tag{III.42}$$

$$\dot{\rho}_{\uparrow\uparrow} = -2Im[\omega_B \rho_{\downarrow\uparrow} - \frac{\Omega}{\sqrt{2}}\tilde{\rho}^*_{\uparrow e}] + \frac{\Gamma}{2}(1 - \rho_{\downarrow\downarrow} - \rho_{\uparrow\uparrow}) \tag{III.43}$$

$$\dot{\rho}_{\downarrow\uparrow} = i\omega_B(\rho_{\uparrow\uparrow} - \rho_{\downarrow\downarrow}) + i\frac{\Omega}{\sqrt{2}}\tilde{\rho}_{\downarrow e} - \gamma'\rho_{\downarrow\uparrow} \tag{III.44}$$

$$\dot{\tilde{\rho}}_{\downarrow e} = i\omega_B\tilde{\rho}_{\uparrow e} - (i\Delta + \gamma)\tilde{\rho}_{\downarrow e} + i\frac{\Omega}{\sqrt{2}}\rho_{\downarrow\uparrow} \tag{III.45}$$

$$\dot{\tilde{\rho}}_{\uparrow e} = i\omega_B\tilde{\rho}_{\downarrow e} - (i\Delta + \gamma)\tilde{\rho}_{\uparrow e} + i\frac{\Omega}{\sqrt{2}}(2\rho_{\uparrow\uparrow} + \rho_{\downarrow\downarrow} - 1). \tag{III.46}$$

These are the optical Bloch equations for the L-system in the rotating frame after making the rotating wave approximation. This form of the OBE can be derived by directly utilizing the Hamiltonian of (III.16), rather than that of (III.15), which makes a move to the rotating frame and makes the rotating wave approximation prematurely.

Although semiconductors are much more complicated than the simple three level system these were derived from, the OBE can describe the dynamics of electron spins in semiconductors quite well. The analytical results presented in the remainder of this chapter and in chapter IV were calculated by solving the OBE with a MatLab script, which can be found in appendix B.

Spin Initialization

Using the OBE, it is important to first model the method with which spin coherence is initialized in the L-system. Assume that electron spins are initially

randomly distributed between the two electron ground states. Upon application of an electric field of the proper polarization, some portion of the population in the $|\uparrow\rangle_Z$ state is excited to the excited state $|e\rangle$, as shown graphically in Fig. 3.3. This leaves a net population in the $|\downarrow\rangle_Z$ state. Due to the applied magnetic field along the x-direction, this net spin polarization will then precess between the two spin ground states at the Larmor precession frequency $2\omega_B$. In the case of our experiments, the decay of the excited state population does not negate the spin polarization because the hole spin inhabiting the excited state energy level rapidly dephases due to light hole/ heavy hole density of state overlap, and thus the excited state population will essentially randomly decay into both ground states [36].

Fig. 3.4 displays this spin initialization mechanism as calculated using the OBE with the decay terms set to zero. The y-axis displays the populations $(\rho_{\downarrow\downarrow}, \rho_{\uparrow\uparrow}, \rho_{ee})$ of the L-system as a function of time. A random distribution of the electron spins

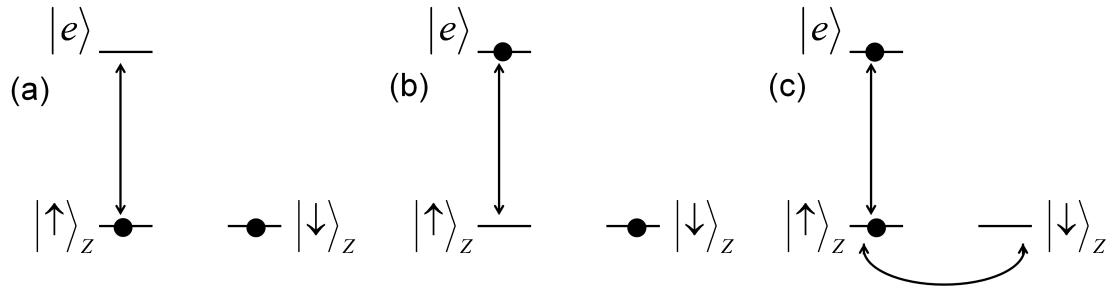

Figure 3.3 Schematic illustrating the spin initialization mechanism. (a) Initially, the electron spins are randomly distributed between the two ground states, with no well defined phase between the states. (b) Population is optically excited from one of the ground states to the excited state, leaving a net spin polarization in the opposite direction. (c) The net spin polarization now precesses back and forth between the two ground states at the Larmor precession frequency.

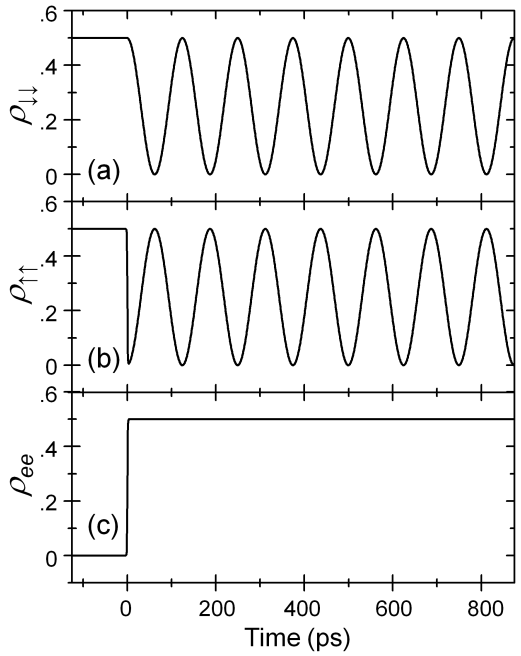

Figure 3.4 Spin initialization without decay terms, calculated using the OBE. A resonant pulse is applied at 0 ps. (a) and (b) Populations of the spin down and spin up ground states, respectively. (c) Excited state population.

pre-pulse is assumed by choosing the initial conditions $\rho_{\downarrow\downarrow} = \rho_{\uparrow\uparrow} = \frac{1}{2}$ and $\rho_{\downarrow\uparrow} = \rho_{\downarrow e} = \rho_{\uparrow e} = 0$. A π-pulse, applied at time $t = 0$ ps excites the population from the $|\uparrow\rangle_Z$ state to the $|e\rangle$ state, leaving a net population in the $|\downarrow\rangle_Z$ state. This population then oscillates back and forth between the ground states with a period $T_B = \frac{2\pi}{2\omega_B} = 125$ ps.

Decay terms must be included to properly model the spin dynamics. Fig. 3.5 depicts the populations of the three-level system with realistic decay terms of a 2DEG. Two decay components are visible in the spin coherence, a short component which follows the trion population decay $\frac{1}{\Gamma} = 500$ ps, and a long component which

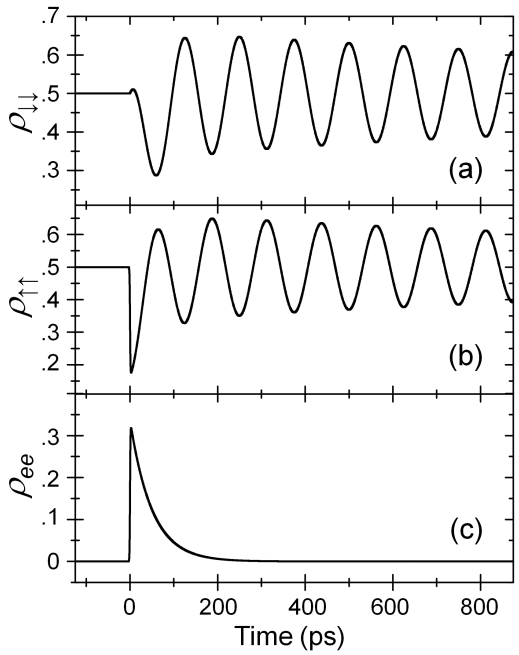

Figure 3.5 Spin initialization with decay terms $\Gamma = .002$ ps^{-1}, $\gamma' = .0005$ ps^{-1}, and $\gamma = 0.5$ ps^{-1}. (a) and (b) Populations of the spin down and spin up electron ground states, respectively. (c) Excited state population. Note, the trion population decay in (c) contributes to a decay term in (a) and (b).

is determined by the spin lifetime $\dfrac{1}{\gamma'} = 2$ ns. In this calculation, the trion is assumed to decay equally into both ground states.

Spin Rotations

With the understanding of how to initialize a spin polarization behind us, it remains to demonstrate how spin rotations are realized. As mentioned in the introduction to this chapter, spin rotations can be realized via an on-resonant or an off-resonant electric field. Experimentally, it is important to utilize off-resonant fields to minimize excited state excitation and the resulting decoherence effects.

However, we will first explore on-resonant fields as a check to ensure that our calculations make sense and are in agreement with the calculations of S. Economou *et al.* [30].

As described in the paper of S. Economou *et al.*, an on-resonant pulse of area 2π will induce a minus sign of the $|\uparrow\rangle_z$ state relative to the $|\downarrow\rangle_z$ state, which is a π rotation of the spin about the z-axis. Clearly, the timing of the optical pulse is important, for if the spin polarization is initially along the z-axis, then a rotation about the z-axis will have no net effect. Conversely, a spin polarization along the y-axis will be rotated to the opposite state.

We use the OBE of the previous section to demonstrate the application of 2π pulses at various times. The top two graphs of Fig. 3.6 demonstrate π-rotations when the spin polarization is along the +y or -y direction when an on-resonant pulse of area 2π is applied. In the absence of decay terms, as shown here, the π rotation is essentially perfect. Compare these with those at the bottom of Fig. 3.6 in which the pulse arrives while the spin polarization is along the +z or -z direction. In those cases, there is no net effect on the electron spins, and the phase of the quantum beats remains the same.

By including decay terms which match the parameters of semiconductor quantum wells, the on-resonant spin rotation technique is no longer adequate. The upper left graph of Fig. 3.7 depicts the effect of an on-resonant 2π pulse under the same conditions of Fig. 3.6 with decay terms now included. Although the

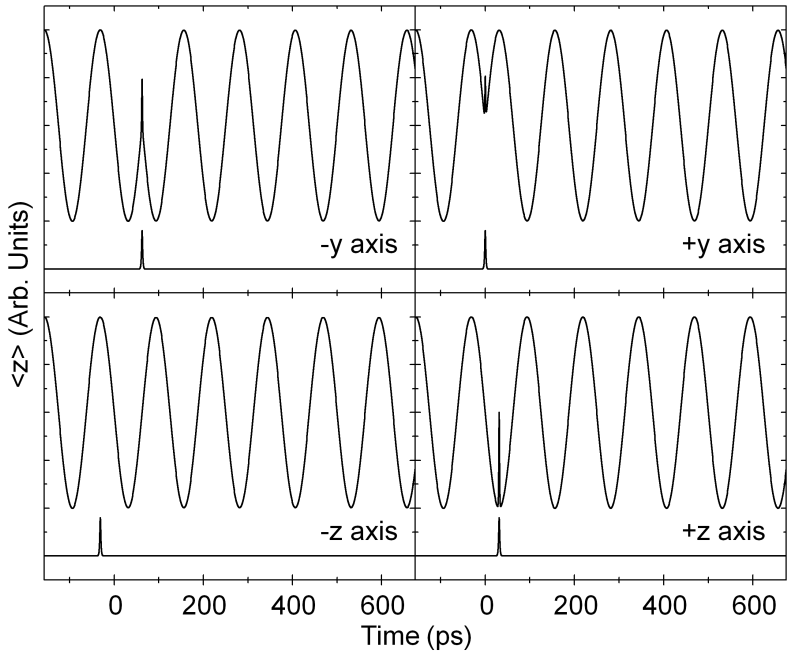

Figure 3.6 Timing dependence of on-resonant pulses of area 2π in the absence of decay terms. The electric field pulse is plotted below each time trace. Top: Pulses applied while the spin polarization is along the y-axis are rotated by π, as is evident by the π phase shift of the oscillations. Bottom: Pulses applied while the spin polarization is along the z-axis leave no net effect. Pulse duration is 2 ps.

rotation still works to some degree, it is far from optimal. The amplitude of the quantum beats after pulse arrival is significantly smaller than before, and there is an additional phase shift (other than the expected π). The main reason that the rotation is so inefficient in this case is due to the very short dipole decoherence time $\frac{1}{\gamma} = 2$ ps, which is characteristic of a 2DEG. In the ideal case, the 2π-pulse leaves no net excited state population as it induces one full Rabi oscillation. The short dipole decoherence time in the realistic case prevents the pulse from driving all of the excited state population back down to the ground state. The efficiency

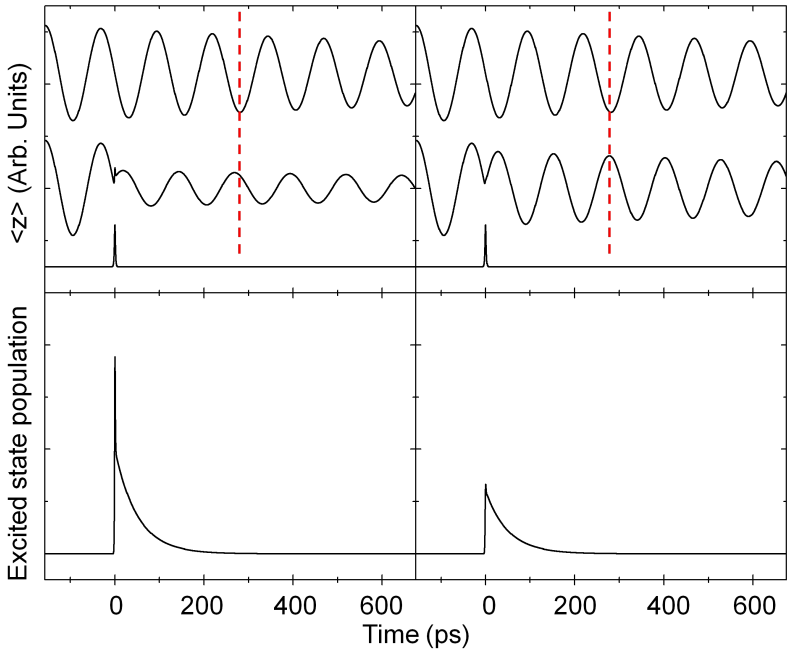

Figure 3.7 Spin flip in the presence of realistic decay terms $\Gamma = 0.002$ ps^{-1}, $\gamma' = 0.0005$ ps^{-1}, and $\gamma = 0.5$ ps^{-1}. Top-left: An applied, on-resonance, 2π optical pulse, shown at the bottom of the graph, performs an inefficient spin rotation, as indicated by the small resulting oscillation amplitude of the z-component of the Bloch vector, $\langle z \rangle$, in the middle of the graph. The plot at the top of the graph is the oscillation in the absence of an optical pulse, for reference. Top-right: The same plot, with the applied pulse now off-resonance by $\Delta = 6$ ps^{-1} and an amplitude 3.25 times larger to compensate for the detuning. Bottom-left: Excited state population in the on-resonant case. Bottom-right: Excited state population in the off-resonant case. Pulse duration is 2 ps.

of the rotation is then hindered by the percent of the population that is trapped in the excited state. In theory, one could make the pulse duration much shorter than the dipole decoherence time to overcome this obstacle. However, in practice this only causes more problems, because the decrease in pulse duration leads to an increase in the spectral bandwidth of the pulse, and excitation of nearby resonances becomes significant.

The dipole decoherence can be overcome more effectively by tuning the pulse below resonance of the excited state. This prevents population from being excited to the excited state, yet it still has the ability to perform full π rotations of the electron spin. The upper right graph of Fig. 3.7 demonstrates the result of applying a pulse with a detuning of $\Delta = 6$ ps^{-1} (≈ 2 nm), under the same conditions of the graph on the upper left, with a 3.25 times stronger field to compensate for the detuning. The efficiency of the rotation is much greater with the introduction of the detuning, as is apparent from the large amplitude of the quantum beats after the arrival of the pulse. The beats are also π out of phase from the reference beats, with no significant additional phase shift. There is still room for improvement, however, which is apparent from the excess excited state population that still persists after the duration of the pulse.

By detuning the pulse, the rotation has been shown to be more effective in the presence of realistic decay terms. In theory, one could continue to detune by arbitrarily large amounts to achieve 100% rotation efficiency. However, in practice this is not practical, as will be explained in detail in chapter IV, because interactions with other resonances become more pronounced with large detunings. As one can imagine, it can be difficult to determine the optimum set of parameters with which to perform efficient spin rotations. Short pulse durations avoid decoherence effects, but if they are too short, meaning large pulse bandwidth, interactions with other resonances become significant. Large detuning avoids decoherence effects,

but requires larger laser power, and also leads to interaction with other resonances. The pulse parameters must be balanced in a way which can only be determined through experimentation.

CHAPTER IV

ULTRAFAST COHERENT ELECTRON SPIN FLIP IN A MODULATION-DOPED CDTE QUANTUM WELL

Figures 4.5-4.7, 4.9, 4.10b, and 4.11b were published in Ref. [21] with co-authors Timothy Sweeney, Ronald T. Cox, and Hailin Wang. The material presented in this chapter was obtained by the author with the exception of the data presented in Fig. 4.5 which was obtained by Timothy Sweeney.

Modulation-doped CdTe Quantum Wells

The semiconductor sample in which we demonstrate the experimental realization of ultrafast optical electron spin flips is a modulation-doped cadmium telluride quantum well. In modulation doping, atoms with one extra electron in their valence shell replace one of the constituent atoms of the material that makes up the barrier of the quantum well. The extra electrons are easily ionized from the dopant atoms and fall into the quantum well, where the potential is relatively low. It is energetically favorable for these donated electrons to relax to the quantum well rather than to remain as a lone electron in the valence shell of the dopant atom. These excess electrons occupy states in the conduction band of the quantum well and have a density proportional to the dopant atom density. The excess

electrons donated through the modulation-doping form a permanent 2DEG and are the electrons whose spin we control through optical manipulation.

CdTe is a direct gap, II-VI semiconductor, with a zinc blende crystal structure, a band gap energy of 1.61 eV [22], and a g-factor of -1.644 [37]. The sample used for the data presented in this chapter was a high quality n-doped CdTe quantum well grown by molecular beam epitaxy on a $Cd_{0.88}Zn_{0.12}Te$ substrate that is transparent near the band edge. It consists of 10 periods of 10 nm width CdTe wells and 45 nm $Cd_{0.84}Zn_{0.16}Te$ barriers. Indium doping in the substrate, with an estimated density of 3×10^{10} cm^{-2}, provides the wells with excess electrons. This sample was generously provided by Ronald T. Cox and K. Kheng of the Nanophysics and Semiconductors team at the Néel Institute and the CEA in Grenoble, France. As a side note, the first experimentally measured trion absorption line was measured in this sample [38].

Optical excitations of the 2DEG are characterized by the trion energy level. A trion consists of two electrons of opposite spin bound to a positively charged hole, similar to a negatively charged hydrogen atom. Fig. 4.1a depicts the energy schematic for trion excitations. $\sigma+$ (σ-) circularly polarized light excites electrons in the 2DEG with spin $s_z = \frac{1}{2}$ ($s_z = -\frac{1}{2}$) to the trion state $|\uparrow\downarrow\Uparrow\rangle_z$ ($|\uparrow\downarrow\Downarrow\rangle_z$), which consists of a hole with total angular momentum $J_z = \frac{3}{2}$ ($J_z = -\frac{3}{2}$) and two electrons of opposite spin. By choosing either $\sigma+$ or σ- polarized light, we are left

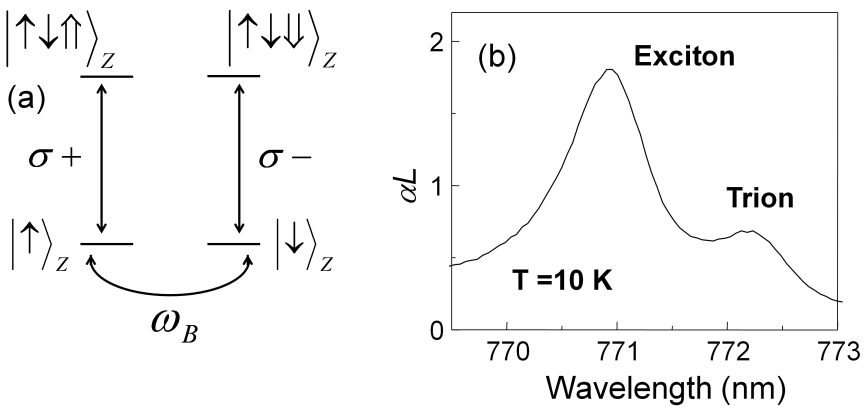

Figure 4.1 CdTe quantum well absorption scheme. (a) Energy level diagram depicting electron spin ground state transitions to trion energy levels. The double arrows in the trion kets represent the heavy hole angular momentum. A magnetic field along the x-direction causes population oscillation between the two electron ground states in the z-basis. (b) Absorption of the CdTe quantum well sample at 10 K. Linewidths of the heavy hole exciton and trion are approximately 1.2 nm and 0.7 nm, respectively.

with an L-system, as described in detail in chapter III, and thus the off-resonant Stark shift spin control mechanism can be implemented.

Fig. 4.1b depicts the absorption of the sample at 10 K in which the trion absorption is clearly observed at a wavelength just above the heavy-hole exciton absorption line. The trion linewidth is $\sim$ 0.7 nm, the HH exciton $\sim$ 1.2 nm, and the center of the trion line is $\sim$ 1.25 nm from the center of the HH exciton line. The close proximity of the trion to the HH resonance can cause major problems for spin control purposes since exciton excitation can lead to detrimental many-body interactions.

Three Pulse Differential Transmission Setup

Three separate laser beams were necessary for the spin control experiment. We refer to them as the "pump" beam, the "control" beam, and the "probe" beam. The circularly polarized pump initializes the electron spin polarization by exciting an electron from the 2DEG to the trion state, leaving a net spin in the opposite direction. The control beam rotates the electron spin via the optical Stark shift. The probe beam measures the spin polarization by measuring the transmission of the sample at either trion transition.

All three beams were derived from the same femtosecond mode-locked Ti:sapphire laser, with 82 MHz repetition rate, as shown in Fig. 4.2. The control pulse was sent through a grating-based spectral pulse shaper which allowed variation of the control bandwidth and center wavelength. The pump and probe beams were sent to separate delay stages to vary the relative delay between the three beams. The probe beam was sent to a spectrometer after passing through

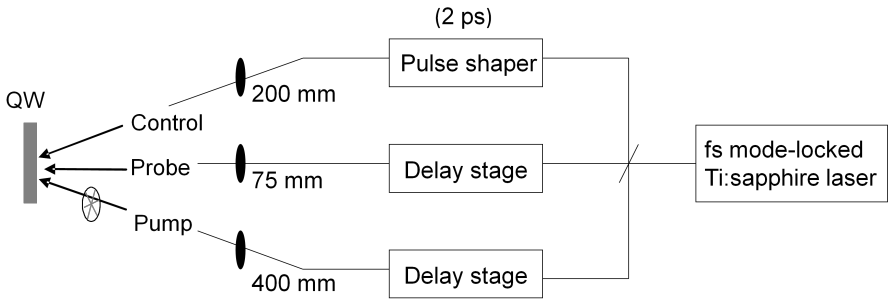

Figure 4.2 Three beam spin control setup. The QW resides in a cold-finger cryostat with a 0.45 T magnetic field applied in the plane of the sample (Voigt configuration).

the sample. An optical chopper was used to modulate the probe beam for lock-in detection in direct transmission measurements. For differential transmission (DT) measurements, the pump beam was chopped instead. Special care was taken to ensure that the spot sizes of the pump and control pulses were large compared to the probe spot size so that the spins measured by the probe were interacting with a relatively uniform optical field. The spot sizes were measured to be 44 μm, 30 μm, and 9 μm for the pump, control, and probe, respectively. A control power of 1 mW corresponds to an estimated energy flux per pulse of 0.6 μJ/cm^2.

The sample was mounted in a cold-finger cryostat, with a helium flow that allowed temperatures as low as 4 K. A permanent magnet was mounted adjacent to the sample such that a 0.45 T magnetic field would be applied in the plane of the sample (Voigt configuration).

Circularly polarized light was used for all three pulses, as required for the trion transitions shown in Fig.4.1a. The probe was chosen to be cross-circularly polarized with the pump and control (pump and control are co-circularly polarized) so that scatter from the pump and control could be removed from the measurement signal.

Control Pulse Design

Three parameters of the control pulse were taken into consideration in designing the experiment, which were the pulse duration τ, the pulse intensity $\sim \Omega^2$, and the detuning Δ.

The fast dipole decoherence time requires τ to be as short as possible. The dipole decoherence in 2DEGs is approximately 2 ps; therefore, pulses were meant to be kept below 2 ps. To avoid exciton excitation, which leads to many-body effects, the Rabi frequency Ω must be kept smaller than the trion to exciton spectral frequency difference. These two requirements are in conflict with the desired parameters for obtaining large rotation angles, as defined by (III.23). Hence, a compromise is necessary, which is to push τ to the 2 ps limit, and keep Δ as small as possible. Through experimentation, it was found that the optimal parameters were $\Delta = 2$ nm and $\tau = 2$ ps (0.5 nm bandwidth).

Fig. 4.3 depicts the spectra of all three beams overlaid with the sample absorption. The tail of the pump and probe pulses were used to initialize and measure the spin polarization, while the control pulse has been spectrally narrowed with the pulse shaper.

Optical Stark Shift

As the spin rotation is based on the optical Stark effect, it is insightful to measure the Stark shifts due to the presence of the control beam. The Stark shift as a rotation mechanism requires the shift of one electron spin state relative to the other. Therefore, it is important to check that both ground states are not shifted by an optical pulse. Fig. 4.4 depicts the absorption of the sample before and during the arrival time of the control pulse for the two cases when the probe is co-circularly

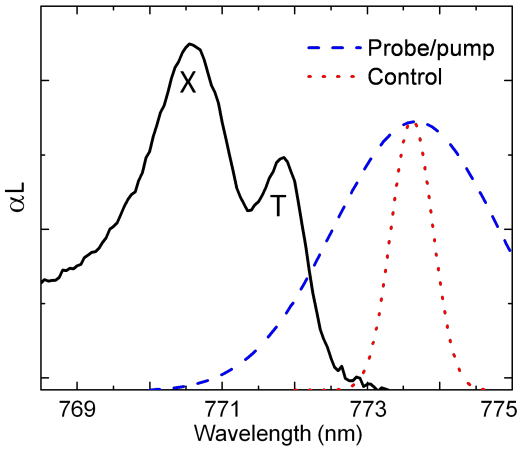

Figure 4.3 Experimental beam spectra. Sample absorption shown in solid black. The high energy tail of the pump and probe interact with the trion resonance. The control beam linewidth has been narrowed by the pulse shaper to 0.5 nm, with center wavelength 1.8 nm detuned from the peak of the trion absorption.

and cross-circularly polarized with respect to the control pulse (no pump beam is present in either case). These data were taken with control pulse parameters that do not match the spin flip parameters to exaggerate the effect of the polarization on the Stark shift. When the beams are co-circularly polarized, the trion absorption peak is shifted to higher energy by a significant amount. When the beams are cross-circularly polarized, the trion peak does not shift. The probe is only able to detect a Stark shift if it is measuring the same transition with which the control pulse is interacting. In the co-circularly polarized case, the probe and control interact with the same transition, whereas they do not in the cross-circularly polarized case. The lack of a blue shift in the cross-circularly polarized case reflects the fact that the control pulse does not induce a significant Stark shift of the electron spin state that

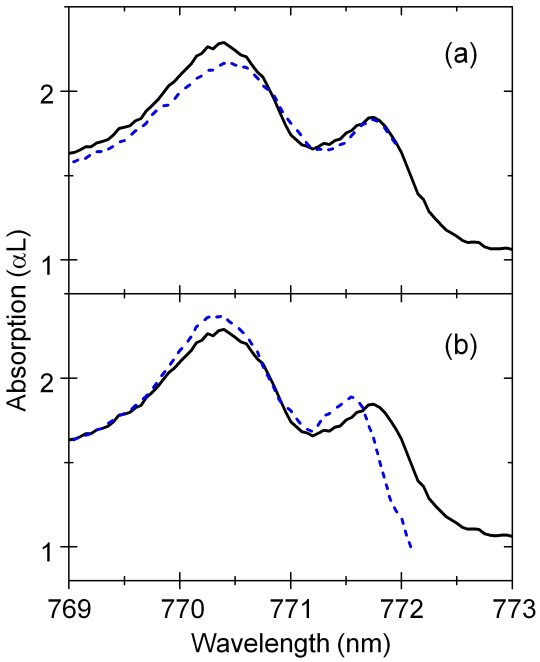

Figure 4.4 Measurements of the Stark shift polarization dependence due to an applied control pulse below resonance at 4 K. Absorption before the control arrival time is shown in black, and during the peak of the control pulse is shown as the dashed blue line. (a) Control and probe beams are cross-circularly polarized, so that they measure the opposite electron spin ground state. No shift is observed. (b) Control and probe are co-circularly polarized, so that they measure the same electron spin ground state. A significant Stark shift is observed. Control pulse parameters were 0.5 nm bandwidth, 3 mW power, and 0.63 nm red detuning from trion peak.

is meant to be stationary, and thus a net energy splitting of the two ground states is achieved.

The following Stark shift data were performed with parameters which matched the spin flip control pulse parameters, and are measured in the absence of the pump pulse. Fig. 4.5 depicts the absorption of the sample at various delays with respect to the control pulse arrival time for two key control pulse powers. The dotted red, solid black, and dashed blue lines depict the absorption 20 ps before, during, and

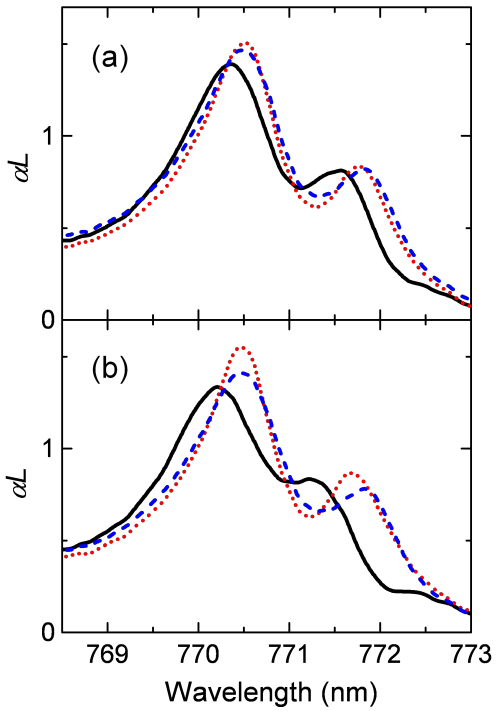

Figure 4.5 (a) and (b) Experimentally measured Stark shifts leading to $\frac{\pi}{2}$ and π spin rotations, respectively, at 4 K. Dotted red, solid black, and dashed blue lines correspond to absorption measurements taken 20 ps before, during, and 20 ps after the arrival of the control pulse. The control pulse had a 0.5 nm bandwidth (2 ps duration), and was detuned 1.8 nm from the trion absorption line.

20 ps after the control arrival time, respectively. By comparing the solid black plots to the dotted red plots, one can observe the Stark shift of the trion absorption as a result of the control pulse. By comparing the dotted red plots to the dashed blue plots, one can observe the recovery of the absorption after the control has passed.

As will be demonstrated in the following section, The 10 mW power used for Fig. 4.5a will result in a rotation of the electron spins by $\frac{\pi}{2}$, and the 20 mW power used for Fig. 4.5b will result in a rotation angle of π. A 10 mW control pulse

induces a peak Stark shift of ~ 0.22 nm and leaves little long lasting effects after its passing. A 20 mW control pulse induces a peak Stark shift of ~ 0.42 nm and results in noticeable bleaching of the exciton and trion peaks 20 ps after the pulse has passed. The bleaching is the major factor which determines the fidelity of spin rotations. The $\frac{\pi}{2}$ rotation will have a high fidelity since bleaching due to the control is negligible. The π rotation will have lesser fidelity as a result of the bleaching, although it will be enough to perform a successful rotation. Improvements in fidelity should focus on control pulses which induce less bleaching while still providing a large enough Stark shift.

As explained in chapter III, the rotation angle is given by the time integrated Stark shift:

$$\phi = \int \delta\omega(t)dt. \tag{IV.1}$$

.

Assuming the control pulse has a Gaussian temporal shape with a 2 ps full width at half maximum, and using the peak Stark shift values cited above, taken from Fig. 4.5, we find the expected rotation angles are 0.54π and 1.05π, from the 10 mW and 20 mW control pulses, respectively. Within our experimental error, this is in excellent agreement with the observed rotation angles to be presented in the following section.

Experimental Spin Initialization

The top plot of Fig. 4.6 depicts a typical DT measurement of electron spin polarization initialized by a 1.6 mW pump pulse. The transmission of the probe follows the sinusoidal oscillations of the electron spins as they precess about the external magnetic field. The 0.45 T applied magnetic field results in a Larmor precession period of 113 ps. The phase of the beats is dependent on the polarization of the probe, since the spin precession can be measured via two separate optical transitions with opposite selection rules (see Fig. 4.1a). Transmission of $\sigma-$ polarized light will oscillate π out of phase with $\sigma+$ polarized light (not shown). It is convenient to set the probe to be cross-circularly polarized from the pump and control (i.e. the pump and control are co-circularly polarized) to avoid interference as a result of scattered light from the pump and control into the spectrometer. For this reason, the probe will be cross-circularly polarized from the pump and control in the remainder of the data in this chapter.

Rotations Vs. Intensity

As mentioned in chapter III, π rotations are only possible while the electron spins are aligned along the y-axis. Since the probe measures the projection of the spins along the z-axis, the spins are along the y-axis when the DT beats are at a midpoint of their oscillations. To perform rotations, the control was first applied at one of these midpoints, and then the intensity was varied.

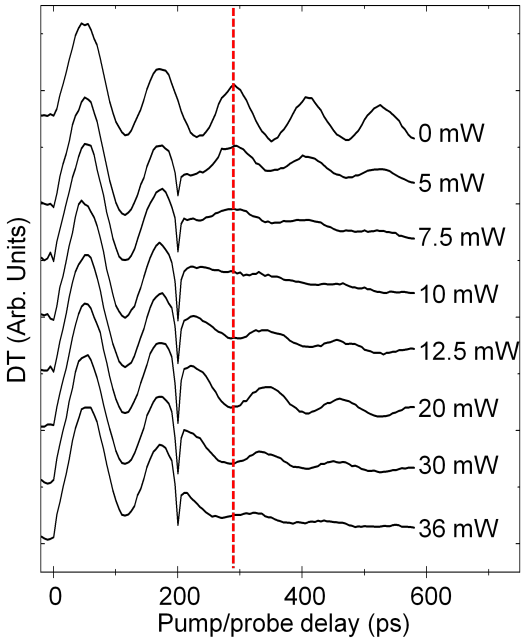

Figure 4.6 Spin rotation versus control pulse intensity at 4 K. Control pulse powers are indicated on the right. $\frac{\pi}{2}$ and π rotations are obtained at 10 mW and 20 mW powers, respectively. Control pulse bandwidth is 0.5 nm (2 ps duration), and detuned 1.8 nm from the trion absorption line. Pump power was 1.6 mW, with 5 nm bandwidth, detuned 1.8 nm red from trion.

Fig.4.6 depicts the result of this applied pulse with various intensities. At powers below 10 mW, the beat amplitude decreases with increasing intensity. At 10 mW, the beats have nearly vanished. This corresponds to a $\frac{\pi}{2}$ rotation in which the spins are along the x-axis. Increasing power beyond 10 mW results in an increase in the beat amplitude, π out of phase with the original beats, until they reach a maximum at 20 mW. This corresponds to the full π rotation angle. Increasing the power beyond 20 mW results in phase shifts other than π as a result of significant excited state excitation.

The power dependence on the rotation angle is in good agreement with the proposed optical Stark shift spin control mechanism. As noted in chapter III, the Stark shift for far detuned pulses $\delta\omega = -\frac{\Omega^2}{2\Delta}$ is linear with the control pulse intensity $I \sim \Omega^2$. Therefore, the rotation angle is expected to be proportional to the pulse power. Since a 10 mW control pulse induces a $\frac{\pi}{2}$ rotation angle, and a 20 mW pulse induces a π rotation angle, the linear intensity dependence is verified.

Using the OBE of chapter III, we can compare the measured results with theory. Fig. 4.7 displays this experimental/ theoretical comparison, where the calculation uses experimental parameters. The calculation agrees well with the experimental results in that the powers corresponding to $\frac{\pi}{2}$ and π rotations are linearly dependent on the control power and that oscillations with phase differences other than π occur at similar powers.

There are two significant differences between the experiment and calculation. Firstly, the beat amplitude for $\frac{\pi}{2}$ rotations is non-zero in the calculation. This is a result of an underestimate of the dipole decoherence time in the calculation. Here, it is assumed to be 2 ps, whereas the true dipole decoherence time of our sample must be somewhat longer, resulting in better $\frac{\pi}{2}$ rotations than predicted. Secondly, the behavior of the beats at high powers appears to be quite different. These differences are actually trivial. When the control power is large enough to excite significant excited state population, it will initialize a new spin polarization. The ratio of the new spin polarization to the original will be dependent on the bath

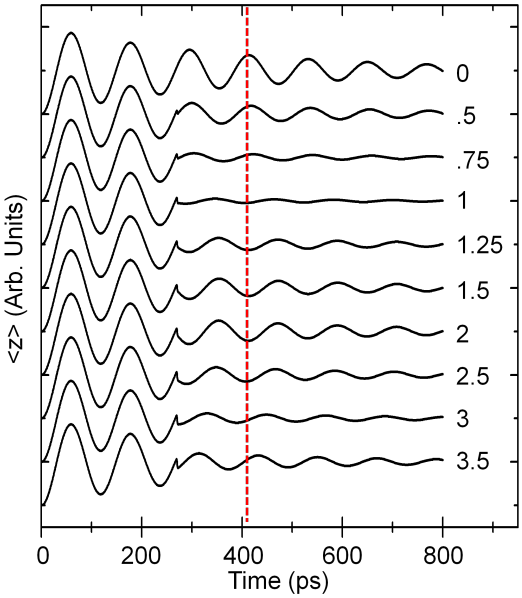

Figure 4.7 Calculated spin rotation versus control pulse intensity. Intensities indicated on the right side of the figure. Control intensities are normalized such that the intensity corresponding to a $\frac{\pi}{2}$ rotation is one. Control pulse parameters were 2 ps duration, and 6 ps^{-1} red detuning. Decay terms used were $\Gamma = 0.002$ ps^{-1}, $\gamma' = 0.0005$ ps^{-1}, and $\gamma = 0.5$ ps^{-1}.

population of electrons. In the calculation, half of the electron spin population is polarized, while in the experiment this number is unknown. A better fit of the spin precession at high powers could be devised simply by varying the bath population in the calculation.

Greater rotation angles can be obtained with a larger control pulse bandwidth at the expense of a decreased fidelity of the π rotation. Fig. 4.8 demonstrates the result of applying a control pulse of 0.9 nm bandwidth and 1.8 nm detuning to the sample under the same conditions as those presented in Fig. 4.6. As the control power is increased from zero, the spin precession amplitude decreases until it nearly

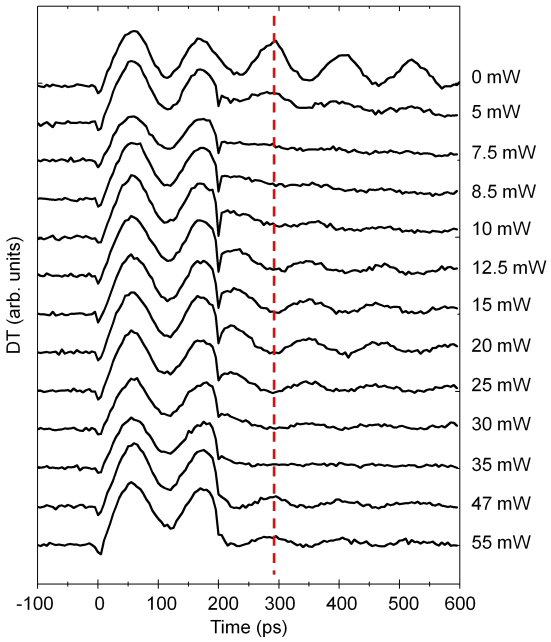

Figure 4.8 Larger maximum rotation angle demonstrated with larger control bandwidth at 4 K. Control bandwidth was 0.9 nm with a detuning of 1.8 nm and powers indicated in the figure on the right.

vanishes at 7.5 mW, corresponding to a $\frac{\pi}{2}$ rotation. Increasing the power beyond 7.5 mW results in an increase in the spin precession amplitude, with the beats now π out of phase with the unperturbed beats. The amplitude is maximized at 20 mW, corresponding to a π rotation. Increasing the control power beyond 20 mW results in a decrease in the spin precession amplitude, until the beats vanish at 35 mW, corresponding to a $\frac{3\pi}{2}$ rotation. Increasing the control power beyond 35 mW results in an increase in the spin precession. Identification of the power which results in a 2π rotation is unclear due to the limited available control power of 55 mW. However, the Rabi oscillations implied in this data are an excellent

demonstration of the coherent control of the electron spins induced by the control pulse.

Pulse Arrival Timing

As mentioned in chapter III, the timing of the control pulse is crucial for π rotations of electron spins. Spins along the y-axis can be fully rotated, while spins along the z-axis will remain unchanged. It is highly important to demonstrate this timing dependence as a check that we are truly observing spin rotations. Fig. 4.9 displays four different control arrival times with a set control power of 20 mW. A sharp spike indicates the control arrival time in the graphs. The top two graphs in Fig. 4.9 demonstrate the result of applying the control pulse while the electron spins are along the y-axis. The 20 mW control pulse in this case induces a complete electron spin flip. Spin precession in the absence of a control pulse are overlaid on these graphs for reference. The rotated electron spins are clearly π out of phase with the unperturbed spins. Alternatively, when the 20 mW control pulse arrives while the spins are along the z-axis, as shown in the bottom two graphs of Fig. 4.9, no spin rotation is induced, which is clearly seen by comparison with the unperturbed spins.

The timing dependence can be extended to arbitrary control arrival times. Physically, a full rotation about the z-axis should result in spin precessions which are symmetric about the control arrival time. A series of such measurements were

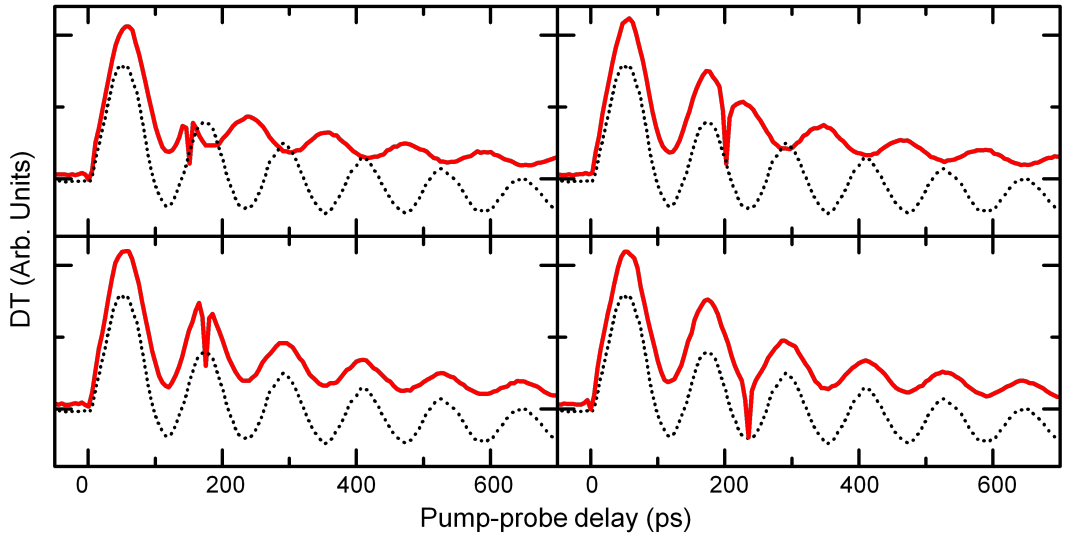

Figure 4.9 Rotation dependence on control pulse arrival time at 4 K. Black dotted lines are spin precession in the absence of the control pulse, for reference. Solid red lines are precessions which interact with a control pulse of 20 mW power, 2 ps duration, and 1.8 nm red detuning. Top: Control pulse arrives at the midpoint of oscillation, while the spins are along the ±y axis. Bottom: Control pulse arrives at an oscillation extrema, while the spins are along the ±z axis.

taken and are graphed together in Fig. 4.10. The precession peaks are clearly mirrored about the control arrival time in this graph.

The high symmetry demonstrated experimentally here is not as easy to achieve as one might expect. The large dipole decoherence rates in semiconductor quantum wells can result in asymmetries. Fig. 4.11b shows a simulation of electron spin flips for different control arrival times when the dipole decoherence time is faster than the control pulse duration. Here, the dipole decoherence is set to 1 ps, while the control pulse duration is 2 ps. The spin precession after the arrival of the control pulse appears to be somewhat bowed, which is a direct result of this rapid decoherence.

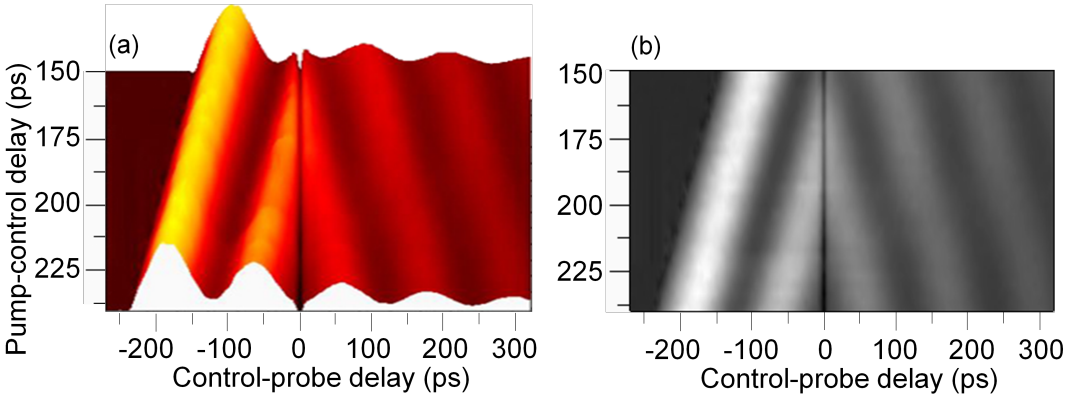

Figure 4.10 Spin precession mirrored about control arrival times at 4 K. Control parameters were 20 mW power, 2 ps duration, and 1.8 nm red detuned. Delay times are given relative to the control pulse delay, rather than the pump pulse delay. (a) Raw data. (b) 2D projection.

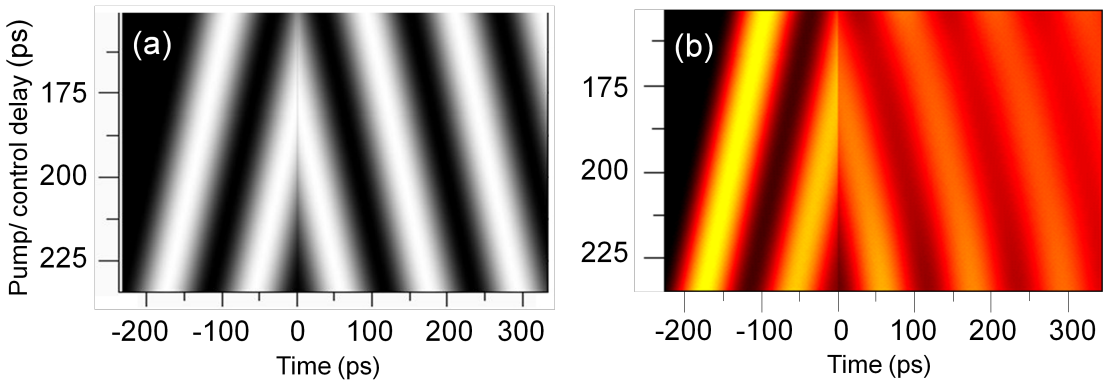

Figure 4.11 Calculated spin precession dependence on control pulse arrival time. Decay terms used were $\Gamma = 0.002$ ps^{-1}, $\gamma' = 0.0005$ ps^{-1}, and $\gamma = 0.5$ ps^{-1}. Control pulse parameters were 2 ps duration and 6 ps^{-1} detuning. (a) Dipole decoherence $\gamma = 0$. (b) $\gamma = 1$ ps^{-1}.

The high symmetry of the spin precession before and after the control pulse in the experiment suggests that the dipole decoherence time is somewhat longer than the expected value of 2 ps. Fig.4.11a demonstrates the same calculation with the dipole decoherence set to zero.

Chapter Summary

The data presented in this chapter was of the first experimental demonstration of complete electron spin flips in a semiconductor quantum well. The image of a mirrored spin precession about the control pulse arrival time presents a key piece of experimental evidence to demonstrate this fact. Rabi oscillations as a function of control pulse power were another key piece of evidence reflecting this result.

It was shown that the spin control mechanism is the optical Stark shift by comparing Stark shifts in absorption measurements to rotation angles of the spin precession. A linear dependence of the rotation angle on the control pulse power verifies the Stark shift mechanism, as well as an estimate of the rotation angle based on the measured Stark shift. The experimental results were in excellent agreement with calculations based on the optical Bloch equations.

CHAPTER V

DONOR-BOUND ELECTRON SPIN COHERENCE IN BULK INP AND GAAS

Figures 5.2a,b, 5.3-5.7, and 5.9-5.11 will appear in future co-authored works which have either been submitted for review or are under preparation for submission. The total of the material presented in this chapter was obtained by the author.

Introduction

Electrons bound to donor impurities in bulk semiconductors are a highly promising spin control system due to their long spin coherence times ($\sim$ ms) [15] and the relatively narrow linewidths of their optical transitions ($\sim$ 1 Å). Donor-bound electrons (DBE) are spatially localized and zero-dimensional. These systems would appear to be highly favorable over either quantum dots or modulation-doped quantum wells for ensemble spin applications for two reasons: (1) the spatial localization of the electrons minimizes decoherence due to spin-orbit coupling, a significant advantage over electrons in modulation-doped quantum wells, and (2) DBEs do not experience the large inhomogeneous broadening that ensembles of quantum dots are found to demonstrate due to fluctuations in size and shape.

Despite the apparent advantage of DBEs for ensemble applications, coherent

spin control in this system has not been as successful to date as in the other major semiconductor spin systems. This chapter will describe experimental efforts to overcome the unique challenges of the DBE system.

Donor Impurities

If an atom is introduced into a lattice which has one electron more than is necessary to form the covalent bonds with neighboring atoms, then it is easily ionized, donating a free electron to the lattice. Such atoms are known as donor impurities. For III-V semiconductors, like GaAs and InP, an atom with three valence electrons (Ga or In) can be replaced by an atom with four valence electrons (Si or Ge, for example) to introduce a donor impurity. Likewise, an atom with five valence electrons (Al or P) can be replaced by an atom with six valence electrons (Se or Te, for example).

An unionized donor is a stationary, hydrogen-like electron-proton pair, whose binding energy and Bohr radius can be predicted by making simple substitutions into the hydrogen atom formulas. Replacing the electron mass m_0 with the electron effective mass m_0^* and multiplying the vacuum permittivity ϵ_0 by the static dielectric constant ϵ_r of the host material, we obtain the binding energy and Bohr radius for DBE's in bulk material:

$$E_{D^0} = -\frac{m_0^* e^4}{32\pi^2\hbar^2\epsilon_r^2\epsilon_0^2}, \qquad a = \frac{4\pi\epsilon_r\epsilon_0\hbar^2}{m_0^* e^2}. \tag{V.1}$$

For the materials discussed in this dissertation, the electron effective mass at the

Λ valley is $m_0^* = 0.067m_0$ for GaAs and $m_0^* = 0.08m_0$ for InP, where m_0 is the true electron mass. The static dielectric constants are $\epsilon_r = 13.18$ for GaAs and $\epsilon_r = 12.5$ for InP. Using these parameters, the values obtained for the above expressions are $E_{D^0} = -5.2$ meV and $a = 104$ Å for GaAs and $E_{D^0} = -7.0$ meV and $a = 83$ Å for InP. This simple model is in good agreement with the experimentally measured values [14, 39, 40].

Donor-bound Excitons

A neutral donor impurity can serve as an attractive potential for carriers in a semiconductor lattice through the van der Waals interaction. Excitons (electron/hole pairs) can be attracted to these impurities and form a four-body complex known as a donor bound exciton (D^0X). D^0Xs are composed of a positive nucleus, two electrons of opposite spin, and a positively charged hole. They are spatially localized due to the immobility of the positive atomic nucleus and hence experience no Doppler broadening, leading to relatively narrow linewidths (~ 1 Å). However, despite numerous theoretical attempts to describe this system, no theory has been able to accurately account for the energy structure and transition selection rules [41–44].

Photoluminescence and absorption experiments have demonstrated a series of non-degenerate energy levels associated with DBE to D^0X transitions [41, 45]. The many transitions are believed to be a result of the different possible spin orientations

of the positively charged hole. Circularly polarized light can interact with these transitions to form a Λ system, similar to that of chapter III. However, examining the measured transition schemes of W. Rühle *et al.* [45] and V. A. Karasyuk *et al.* [41], we find that other allowed transitions may interfere with this Λ system picture. The presence of these other transitions will put additional constraints on spin control parameters.

Donor-bound Electron Spin Coherence in GaAs

Introduction

Recent studies of electrons bound to neutral donors in bulk GaAs have shown limited success. Full π rotations have yet to be attained; however, rotations of up to $\frac{\pi}{3}$ have been demonstrated by K. Fu *et al.* [46]. Although $\frac{\pi}{3}$ rotations fall short of the ultimate goal, they are surprisingly good in light of our own experimental efforts in the same system. As a side note, spin echo measurements on DBEs have since been demonstrated by the same group using the $\frac{\pi}{3}$ rotation pulse [47]. They identify the limiting factor in their spin control measurements as an enhanced dephasing due to free exciton excitation and the associated many-body effects. Our interpretation of their findings was that it should be possible to improve upon the $\frac{\pi}{3}$ rotation by a narrowing of the linewidth of the applied rotation pulse, which would reduce the peak intensity of the pulse, reducing the intensity dependent excitonic

excitation. The reduction in the pulse area due to the peak intensity decrease is compensated by a longer pulse duration.

Through our own investigations, we found that the higher energy D^0X states can have significant, but detrimental, contributions to the spin rotation, which puts an additional limiting factor on the system. Our measurements suggest that the higher energy D^0X states can limit the efficiency of Stark shift based rotations by as much as an order of magnitude under realistic experimental parameters for the following reason: the spin rotation mechanism of a far detuned control pulse can be seen as resulting from Stark shifting one electron spin state with respect to the other, as described in detail in chapters III and IV. In the D^0X system, the strange optical selection rules can cause pulses to induce Stark shifts of both DBE ground states simultaneously, as observed in our measurements to be described below. In effect, any expected rotation due to Stark shifting one DBE spin state will be undone by the simultaneous Stark shift of the other DBE spin state. Fig. 5.1 illustrates this effect schematically. The net energy difference between the ground states, and hence the net rotation angle, will be small using this technique, and beam powers that exceed those of other semiconductor spin systems will be necessary to compensate for this effect. High beam powers introduce decoherence, which ultimately limits the maximum attainable rotation angle [48]. It is our hope that the $\frac{\pi}{3}$ rotation angle can be improved upon by taking into account the effect of the

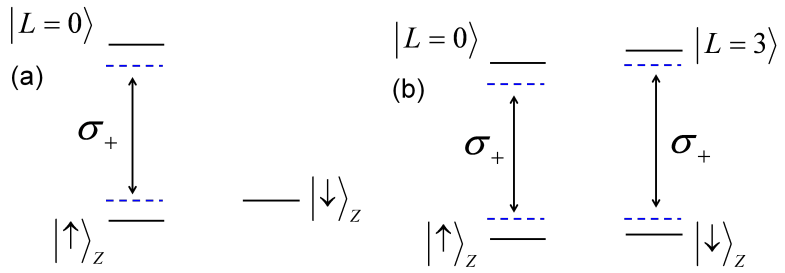

Figure 5.1 Stark shift of electron spin ground states in two cases. (a) One ground state couples to an excited state with a given polarization of light (in this case $\sigma+$), resulting in a net energy difference of the two ground states. (b) Both ground states couple to excited states with the same polarization of light, resulting in a small net energy difference between the two ground states.

higher energy D^0X states which are a previously unidentified culprit in the limiting of the efficiency of Stark shift based spin rotations.

Experimental Setup

Our experiments were conducted in high purity bulk GaAs of 10 μm thickness, grown by molecular beam epitaxy on a GaAs substrate. The substrate was removed by wet etch for transmission measurements. To minimize spectral broadening associated with strain, the sample was placed in a holder which allowed it to remain free-standing, as described below. It was mounted in an exchange gas cryostat with a permanent magnet adjacent to the sample such that a 0.45 T magnetic field was applied in the sample plane (Voigt configuration). The sample absorption was measured using the broad bandwidth (5 nm full width) of a femtosecond mode-locked Ti:sapphire laser with an 82 MHz repetition rate. Differential transmission (DT) data was taken by measuring the change of transmission of a weak probe beam with a lock-in amplifier due to a chopped pump beam. The terms pump and

probe refer to the spin polarization initializing and measuring beams, respectively. An electronically controlled linear stage was used to vary the relative arrival time of the two pulsed beams. An average pump power of 0.1 mW corresponds to a peak pulse intensity of 800 W/cm^2. The GaAs sample used for the data presented was generously donated by John Prineas from the Department of Physics and Astronomy at the University of Iowa.

Two free standing holders were utilized in our measurements to reduce the sample strain. The first was a brass holder, produced by Kris Johnson from the TSA machine shop at the University of Oregon, which was made out of brass and allows samples to be replaced as needed. We chose brass because its thermal expansion coefficient is closest to GaAs out of the common metals used in machine shops. A slot in the holder had approximately the same dimensions of our samples, with a little leeway, and small holes through which lasers could pass through the sample. The sample was made free standing by first using crystal bond to adhere it to a sapphire disc so that the substrate could be etched away. Afterwards, the crystal bond was removed with acetone, and the sample washed free of the crystal bond. This left a 10 μm thin GaAs wafer, which is surprisingly easy to handle, and will generally not break unless squeezed.

A second free standing holder was constructed which itself was made of GaAs so that the thermal expansion of the holder would match the sample. This holder was made by bonding several large pieces of GaAs together using crystal bond. The

pieces were constructed so that a slot made to be the same size as the sample was produced, and two holes were etched through the GaAs holder so that lasers could pass through the sample. The holes were etched using a methanol and bromine mixture, which etches a millimeter of GaAs within minutes. Most of the GaAs was covered with paraffin wax to protect it from the etchant, but a hole was poked through the wax where the etchant was meant to produce holes. This procedure works with decent accuracy, although the edges are somewhat jagged, and can encourage laser scattering. It was found through experimentation that the GaAs holder did not produce a noticeable difference on the sample strain, and so the brass holder was used for most of our measurements. The convenience of being able to switch samples using the brass holder was a major benefit. The data shown in the following sections was taken using solely the brass holder. The GaAs holder was mentioned simply to make the point that the thermal expansion of the brass holder did not result in an added strain on our free standing sample.

Experimental Results

Optical excitations of DBEs are characterized by transitions to the D^0X states. Identification of D^0X to DBE transitions is primarily obtained through photoluminescence (PL) measurements. The PL of our sample at 4 K is shown in Fig. 5.2a. Multiple emission lines corresponding to D^0X to DBE transitions are evident around 819.5 nm and are readily identified by comparison to previous experimental work [48]. We label the D^0X transitions using the notation L =

0, 1, 2, 3 from lowest to highest energy in accordance with V. A. Karasyuk *et al.* [41]. Additionally, the free exciton (X), ionized donor-bound exciton (D^+X), and acceptor-bound exciton (A^0X) states are visible. Although only three D^0X emission lines are resolved in this data, comparison to other higher resolution measurements shows that a fourth emission line is present near the lowest energy D^0X line [48]. All D^0X transitions show relatively narrow linewidths of ~ 1 Å, which is characteristic of donor states due to the fact that they are nonmobile and do not experience Doppler broadening. The high purity of our sample is demonstrated by the well defined D^0X peaks, which can broaden into each other at higher donor densities [49, 50].

Although the D^0X transitions are clearly visible in photoluminescence data, they are difficult to resolve in absorption data due to the high purity of our sample and resulting low donor concentration. Fig. 5.2b shows the absorption of our sample at 4 K. A large exciton absorption peak dominates the signal and produces a series of Fabry-Perot fringes throughout the surrounding spectral domain. Absorption lines corresponding to D^0X to DBE transitions cannot be unambiguously resolved in these plots because of the interference. A calculation of an absorption complicated by Fabry-Perot interference is shown in Fig. 5.2c to illustrate this point (see appendix A for calculation). Despite the difficulty in resolving the D^0X peaks in direct absorption measurements, they make a clear contribution to the differential transmission (DT) signal, as will be described

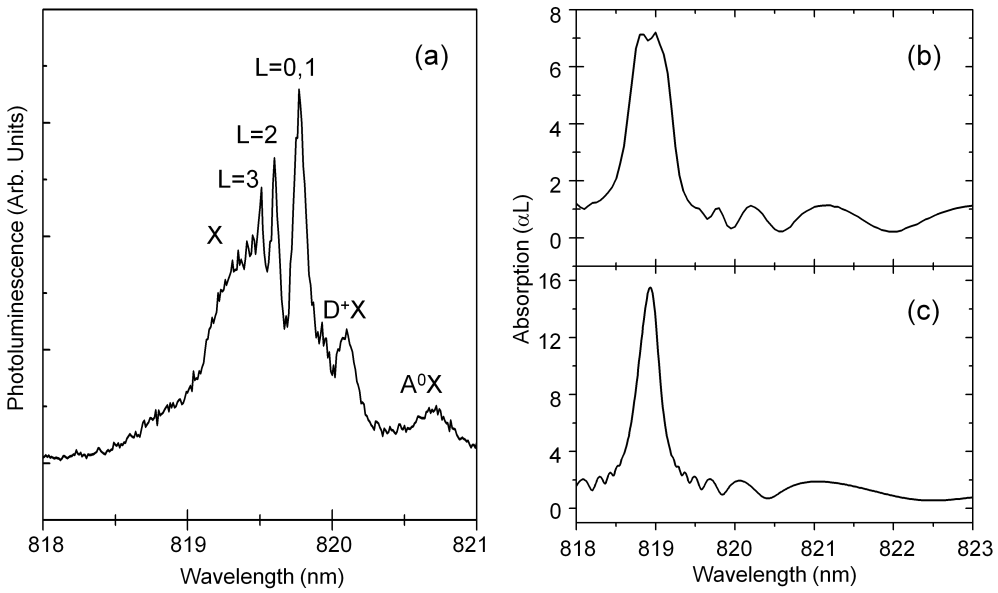

Figure 5.2 (a) Bulk GaAs PL demonstrating D^0X transitions at 4 K, using a 532 nm excitation beam. (b) Bulk GaAs absorption spectrum. (c) Absorption calculation demonstrating Fabry-Perot interference near a large absorption peak. Parameters used, defined in appendix A, were: $R = 0.323$, $L = 10$ μm, $\gamma_0 = 0.6$ ps^{-1}, $\gamma' = 24$ ps^{-1}, $\frac{Ne^2 f_0}{\epsilon_0 m} = 143.4$ ps^{-2}.

below. From the DT measurements, the spectral position of the lowest energy D^0X peak is found to be 0.65 nm (1.1 meV) red of the free exciton peak. This spectral separation places the D^0X transitions within the lower energy tail of the free exciton peak, and for this reason care was taken to minimize the broadening due to inhomogeneous sample strain by placing the sample in a free standing holder, described in the previous section. The free standing holder made a noticeable difference in minimizing the inhomogeneous strain, although the free exciton/ D^0X spectral overlap cannot be completely removed due to the large magnitude of the free exciton absorption. The close proximity of the large free exciton absorption

prevents on-resonant DBE spin control since excessive free excitons would be produced in such a process, which leads to a large enhanced decoherence [48].

Fig. 5.3a depicts the nonlinear spectrum of a DT measurement of a weak probe in the presence of a chopped, circularly polarized pump which is resonant with the lowest energy D^0X peak. The probe beam measures the change in the absorption spectrum due to the presence of the pump beam. Two narrow peaks emerge at zero delay between the pump/ probe arrival times. These peaks are identified as the $L = 0$ and $L = 3$ D^0X transitions based on their relative spectral separation from each other and from the free exciton. The lowest energy D^0X peak is situated 0.65 nm (1.1 meV) from the free exciton peak, and the two D^0X peaks are separated

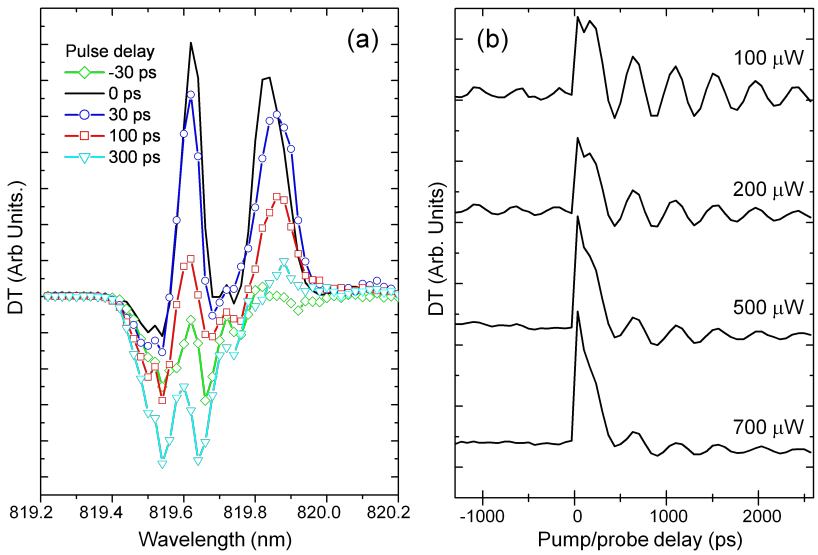

Figure 5.3 D^0X peaks observed in DT measurements, using a 0.04 nm bandwidth pump pulse centered at 819.85 nm, resonant with the $L = 0$ D^0X transition. (a) D^0X bleaching observed in spectral dependence using a 100 μW pump power. (b) Quantum beats at the $L = 0$ transition demonstrate coherence which outlasts the laser repetition period (12.5 ns) under adequately low excitation power.

by 0.28 nm (0.5 meV). These numbers can be compared with Ref. [43, 50]. The $L = 2$ peak does not seem to appear in this data, which may be a result of a weaker transition strength. However, it does make an appearance, in measurements to be described below, at a position midway between these transitions, and thus further verifies our identification of the two D^0X lines shown as the $L = 0$ and $L = 3$ transitions.

Quantum beats clearly emerge when the pump/ probe delay is varied across a 3 ns window. Fig.5.3b depicts quantum beats at the $L = 0$ D^0X peak when initialized by a resonant pump beam of width 0.04 nm. At low temperatures and modest pump power the quantum beats demonstrate extremely long lifetimes, longer than the repetition rate of the laser (12.5 ns), as observed from the beats at negative delays in Fig. 5.3b. Beats are also observed at the $L = 3$ peak, although they are π out of phase with the beats observed at the $L = 0$ peak, as seen by comparing the two plots of Fig. 5.4a. The opposite phase dependence suggests that the $L = 0$ and $L = 3$ D^0X states couple to the opposite DBE ground state, as shown in Fig. 5.5. This proposed transition scheme is further confirmed by moving the pump beam to be resonant with the $L = 3$ state and observing the resultant beats. When the pump is resonant with the $L = 3$ state, the beats observed at the $L = 0$ transition are opposite of what they are when the pump is resonant with the $L = 0$ state, which can be seen by comparing the plots in Fig. 5.4b. More will be said about this proposed transition scheme and its implications in the following section.

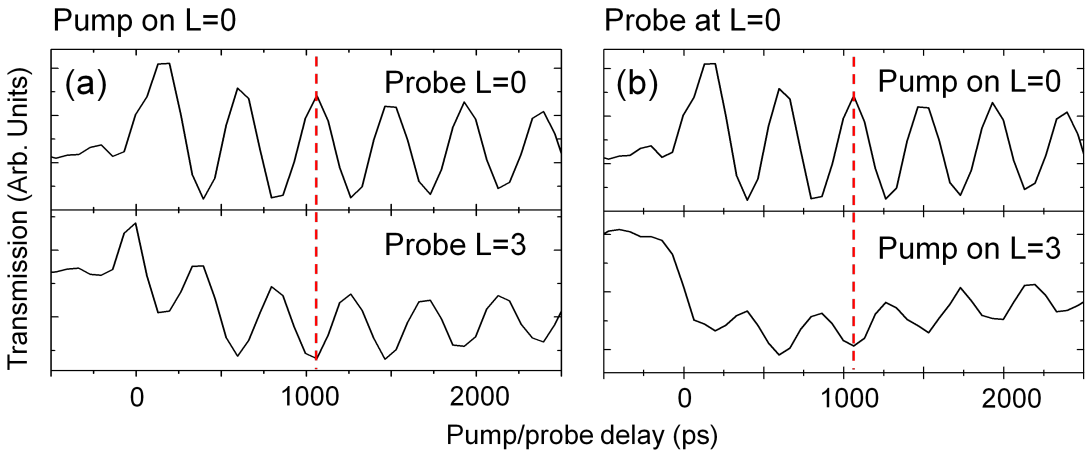

Figure 5.4 Comparison of quantum beats observed at the $L = 0$ and $L = 3$ transitions. (a) A pump resonant with $L = 0$ initializes beats at $L = 0$ and $L = 3$, which are π out of phase with each other. (b) A pump resonant with the $L = 3$ transition initializes beats at $L = 0$ which are π out of phase with the beats at $L = 0$ when the pump is resonant with $L = 0$. The pump bandwidth was 0.04 nm with 100 μW excitation power

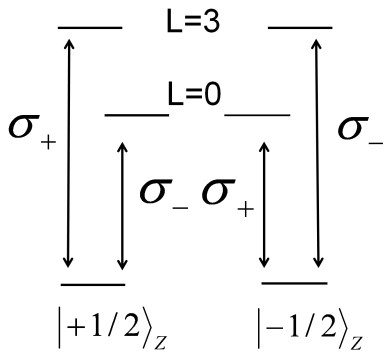

Figure 5.5 Observed D^0X transition scheme in bulk GaAs using circularly polarized light. Pulses of either polarization couple to both DBE ground states.

The full spectral dependence of the quantum beats can be observed by comparing the transmission during the peak of an oscillation with that during the trough of an oscillation. In this way, one can see how the absorption spectrum is changing as a result of the oscillating electrons. The DT at different delay times with respect to the pump pulse is shown in Fig. 5.6a. It is difficult to determine the effect of the oscillating electrons on the spectrum from the raw data shown here since Fabry-Perot interference once again complicates the spectrum. However, by plotting the difference in spectra at different times, the behavior becomes more clear. The method is as follows. Spectra were taken at the six

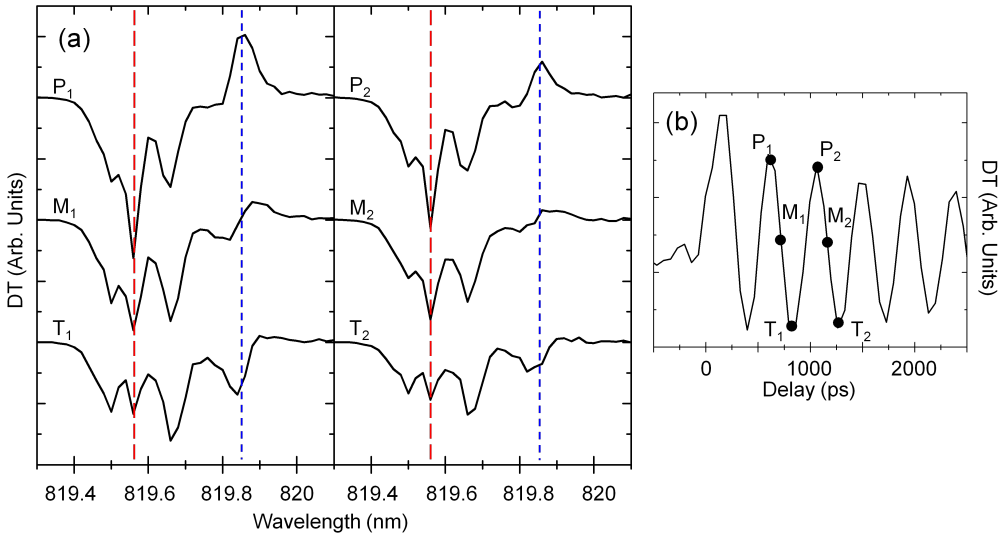

Figure 5.6 (a) Nonlinear spectrum at various delays, corresponding to key oscillations points. The $L = 3$ and $L = 0$ transitions are marked by the red long dashed line and blue short dashed line, respectively. (b) Definitions of the oscillation times at which nonlinear spectra were measured. Relative to the pump arrival time, these are: $P_1 = 600$ ps, $M_1 = 710$ ps, $T_1 = 830$ ps, $P_2 = 1040$ ps, $M_2 = 1150$ ps, and $T_2 = 1270$ ps.

different times shown in Fig. 5.6b. These times are labeled P_1, P_2, M_1, M_2, T_1, and T_2, according to whether they were taken at the peak, midpoint, or trough of a quantum beat oscillation. Fig. 5.7 displays the result of subtracting the spectra taken at a midpoint from the spectra taken at the peaks or troughs. In other words, if the time dependent spectra is denoted as S(t), then we plot the change in spectra $S(P_1)$ - $S(M_1)$, $S(T_1)$ - (M_1), $S(P_2)$ - $S(M_2)$, and $S(T_2)$ - $S(M_2)$. Examining Fig. 5.7, we can see that the D^0X peaks switch sign when the beats evolve from a peak to a trough, consistent with beating. Additionally, the beats at each D^0X peak are π out of phase, as demonstrated by the opposite signs of the two D^0X peaks in a given plot. Finally, the $L = 2$ D^0X peak seems to emerge in this data,

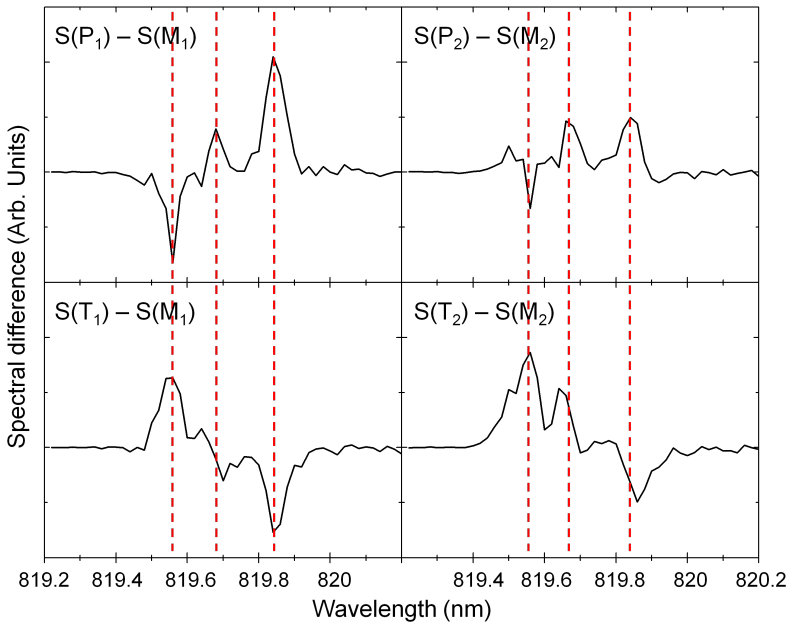

Figure 5.7 Spectral response to electron spin precession. The dashed lines mark (from left to right) the $L = 3$, $L = 2$, and $L = 0$ transitions.

as evidenced by the time dependent activity in between the $L = 0$ and $L = 3$ peaks. The contribution of the $L = 2$ transition to this data is relatively weak and does not demonstrate clear beating as a function of time, suggesting that the $L = 2$ transition does not interact significantly with circularly polarized light. This sentiment is demonstrated more dramatically in the absence of the $L = 2$ transition in the previously mentioned DT measurements of Fig. 5.3a.

Discussion of Results in Bulk GaAs

The opposite phase of the quantum beats at the $L = 0$ and $L = 3$ D^0X peaks has a negative impact on the efficiency of Stark shift based spin rotations, as will be explained in this section. Based on the spectral dependence of the phase of the quantum beats, the energy level diagram can be effectively described as shown in Fig. 5.5. In this diagram, circularly polarized light couples the $L = 0$ and $L = 3$ D^0X states to opposite DBE ground states. The $L = 2$ D^0X state is not included because it seems to have a much weaker transition strength, as evidenced by its absence in the DT data of Fig. 5.3a.

The energy diagram of Fig. 5.5 is qualitatively different than the trion transition scheme described in chapter IV. In that case, circularly polarized light couples a single electron spin ground state to a trion energy level, while the opposite electron ground state remains optically inert. For this reason, a below resonant circularly polarized pulse can induce a Stark shift of one electron ground state relative to the other, as explained in detail in chapters III and IV. Alternatively,

DBE ground states couple to separate D^0X states using the same polarization, and so an attempted Stark shift of one DBE ground state will be accompanied by the simultaneous Stark shift of the other DBE ground state. Therefore, the net Stark shift induced energy separation of DBE ground states will be smaller than the splitting induced in systems where one ground state remains optically inert.

The limited Stark shift efficiency can be easily estimated by extending the Stark shift calculation in the adiabatic limit, demonstrated in chapter III. In the L-system of chapter III, it was shown that the Hamiltonian can be reduced to an effective two-level Hamiltonian given by:

$$H = \hbar \begin{pmatrix} 0 & -\omega_B \\ -\omega_B & -\dfrac{\Omega^2}{2\Delta} \end{pmatrix} \tag{V.2}$$

The total Stark shift induced energy splitting of the ground states is $\Delta E_0 = \dfrac{\Omega^2}{2\Delta}$, where the zero subscript labels this as the splitting in the case that only one DBE state is Stark shifted by the applied beam. This energy splitting will change in the presence of the additional excited state (the $L = 3$ transition). The four level Hamiltonian that results from adding an additional excited state to the L-system can also be reduced to an effective two-level Hamiltonian under the adiabatic limit. In this case, the approximation is that both excited state populations are invariant in time, which is valid in the large detuning regime. The resulting set of equations are solved almost identically as the above case, which was worked out in chapter III, and so the details will not be repeated here. In matrix form, the reduced two-level

Hamiltonian is given by:

$$H = \hbar \begin{pmatrix} -\dfrac{\Omega^2}{2(\Delta+\delta)} & -\omega_B \\ -\omega_B & -\dfrac{\Omega^2}{2\Delta} \end{pmatrix} \tag{V.3}$$

where δ is the energy separation of the excited states. By comparing the diagonal elements of (V.3), we can see that the Stark shift induced energy splitting is $\Delta E_t = \dfrac{\Omega^2}{2\Delta} - \dfrac{\Omega^2}{2(\Delta+\delta)}$, where the t subscript labels this as the splitting in the case that the $L = 3$ excited state is included. To compare this case to the ideal case ΔE_0, we can define the ratio $R = \dfrac{\Delta E_t}{\Delta E_0}$. This ratio deviates from 1 for detunings Δ on the order of the excited state energy separation δ, and goes to zero for $\Delta \gg \delta$. R is plotted in Fig. 5.8a as a function of detuning for various values of δ. In our bulk GaAs sample, $\delta = 0.5$ meV. R for this value of δ is shown in black at the bottom of Fig. 5.8a. For detunings on the order of that cited by K. Fu *et al.* [48], which is 1 THz (4.1 meV), the Stark shift efficiency is only about 10 percent of the expected value from the ideal case. Therefore, complete spin rotations require optical powers that are 10 times greater than would otherwise be required. To put this into perspective, an efficiency reduction of one half would render complete spin rotations of the 2DEG impossible according to Fig. 4.6 of chapter IV. Clearly, the Stark shift efficiency can be increased by reducing the detuning of the Stark shift inducing pulse. However, near resonant pulses interact with the large nearby exciton absorption, resulting in an enhanced dephasing due to many-body interactions. Taking these two factors

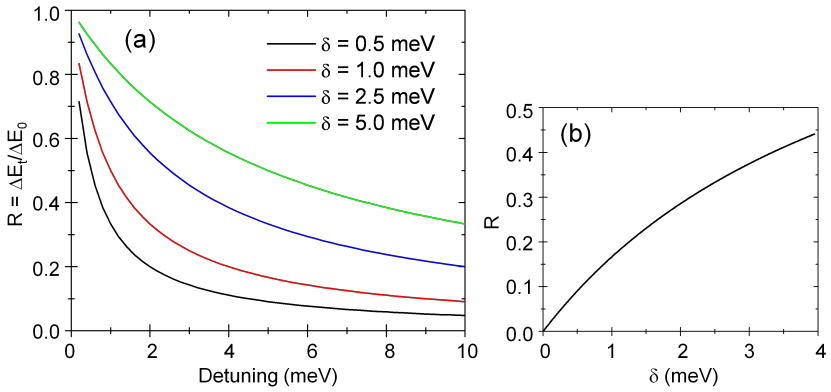

Figure 5.8 (a) Efficiency of Stark shift induced energy splitting versus detuning for various $L = 0$ to $L = 3$ energy separations δ. (b) Efficiency versus δ for a set detuning of $\Delta = 5$ meV.

in mind, it may be possible to compromise such that either limiting case can be avoided, although a successful set of parameters are yet to be discovered.

The two factors mentioned above which limit the success of spin rotations in bulk GaAs can be reduced if some of the above energy separations are increased. For far off-resonant pulses, the reduction in Stark shift efficiency due to coupling to both excited states can be improved upon by an increase in the excited state energy separation δ. Fig. 5.8b shows the R dependence on δ for a fixed detuning $\Delta = 5$ meV. R is approximately linear with δ for $\delta \ll \Delta$, therefore a threefold increase of δ would result in a threefold increase in the spin rotation angle, improving the previous $\frac{\pi}{3}$ rotation angle demonstrated by K. Fu *et al.* to a full π rotation.

For near resonant pulses, a greater D^0X to free exciton energy separation would reduce free exciton excitation and the resulting enhanced dephasing. It is possible that either energy separation could be manipulated to more appropriate parameters

through a clever use of external magnetic field or applied sample strain. It is unclear whether such techniques could overcome the inherent difficulties of the system. However, the $\frac{\pi}{3}$ spin rotations demonstrated by K. Fu *et al.* are promising. If the Stark shift efficiency can be increased by 3 times through the means described above, then complete π rotations should be possible.

Other semiconductors naturally demonstrate larger energy separations for the states mentioned above. The D^0X peaks of GaAs are much more closely packed than many other semiconductor materials, as compared in Ref. [43]. The free exciton peak is separated from the lowest energy D^0X state by a larger amount in many semiconductor materials as well. For these reasons, it may be wise to abandon DBE spin control in GaAs altogether in pursuit of a material with more appropriate parameters.

Donor-bound Electron Spin Coherence in InP

Introduction

The inability to perform full π rotations on DBE spins in bulk GaAs has led us to consider other bulk semiconductor systems whose natural parameters may be more suitable for electron spin control. As a III-V semiconductor is preferred due to their relatively sharp linewidths, we chose to investigate bulk InP. InP may be a more suitable material than GaAs because it has a larger g-factor $g_e = 1.25$, a larger D^0X to free exciton energy difference $\Delta E_f = 1.557$ meV [45], and a larger

separation of the D^0X states [43]. To compare, in GaAs $g_e = -0.42$ and $\Delta E_f =$ 1.1 meV [50]. A larger g-factor is convenient because smaller magnetic fields are necessary to produce the same Zeeman splitting, which in this case eliminates the need for a superconducting magnet. A larger D^0X to free exciton energy difference is highly important because it reduces unwanted free exciton excitation and hence minimizes detrimental many-body interactions, as described by K. Fu *et al.* [46]. The larger separation of the D^0X peaks improves the efficiency of Stark shift based spin rotations, as described in detail in the previous section. For these reasons, we began to investigate DBE spin coherence in bulk InP. The data presented in this dissertation was measured in a sample graciously provided by Liming Zhang from Bell Labs, Lucent Technologies.

Experimental Setup

The setup used to investigate bulk InP was essentially the same as that described above for GaAs. A notable difference is the adhering of the bulk InP to a sapphire disk, rather than to allow it to remain free standing. Although we attempted to create a free standing sample, it was found that InP is much more plastic than GaAs. GaAs could remain free standing because a 10 μm wide sample would remain ridged, but a similar slab of InP would curl, much like a ribbon when a knife is ran along it to make it curl for decoration. Therefore, it was necessary to adhere the InP to a sapphire disk. A low strain adhesive (Norland Optical Adhesive 88) was used to minimize the resulting strain in the adhering process. Ultimately, the

sample was found to experience a slight in-plane compressional strain due to the greater thermal expansion of InP compared to the a-plane thermal expansion of sapphire. The difference in thermal expansions is demonstrated by comparing data from various sources [51, 52]. The InP sample was 3 μm wide along the growth direction.

Experimental Results

The spectral position of the D^0X transitions is determined by photoluminescence data. Fig.5.9a depicts the photoluminescence of our sample at 6 K when illuminated by a 532 nm continuous wave laser. Emission at 874 nm corresponding to D^0X to DBE emission can be seen as well as two peaks at higher wavelength corresponding to acceptor-bound exciton transitions. Only two D^0X peaks can be individually resolved from our sample in contrast with other higher quality samples in which at least four unique states can be seen [45]. This, in conjunction with the large acceptor state emission, is a sign that our sample contains a large number of impurities, many of which do not contribute to donor-bound exciton formation. An unfortunate effect of these impurities is to contribute to the broadening of the HH exciton absorption peak, as well as the D^0X peaks [49]. Unwanted excitations can result as a consequence. In the case of GaAs, identification of the peaks as L = 0, 1, 2, or 3 was simple since each emission line matched the previously reported data. However, in the case of this InP sample, the absence of many of the lines in the PL makes identification unclear, especially since the spectral separation of these peaks

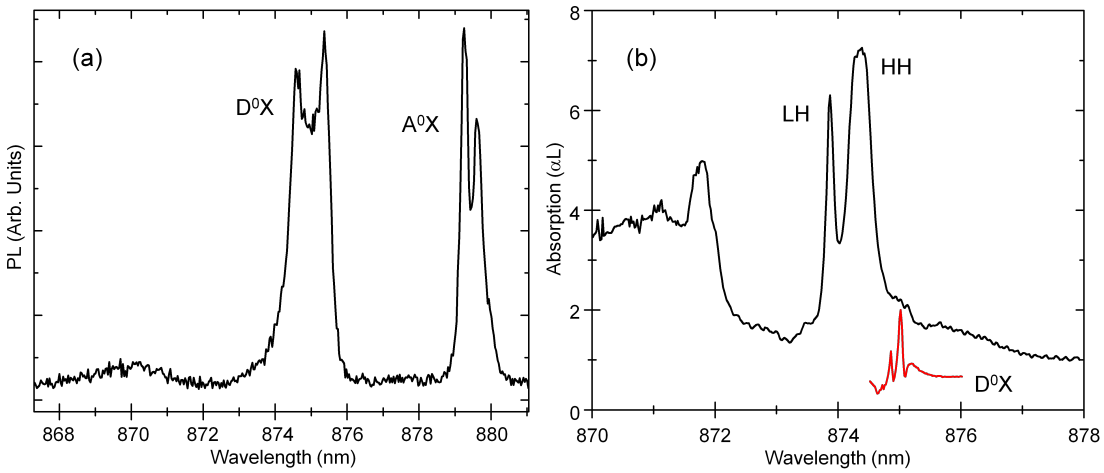

Figure 5.9 (a) Bulk InP PL demonstrating D^0X transitions at 6 K, using a 532 nm excitation beam. Significant acceptor-bound exciton (A^0X) PL is also apparent at lower energy. (b) Absorption spectrum at 1.4 K. DT measurement of D^0X transitions is overlaid with the absorption to demonstrate relative exciton/D^0X spectral separation. DT not to scale with linear absorption.

(0.6 meV) does not match the values reported by W. Rühle *et al.* [45]. For this reason, we drop the L notation and refer to these peaks simply as D^0X_1 (at higher wavelength) and D^0X_2.

Absorption measurements were performed using a femtosecond mode-locked Ti:sapphire laser with an 82 MHz repetition rate. As shown in Fig.5.9b, LH and HH exciton absorption peaks are evident around 874 nm. The HH absorption is split from the LH by 0.54 nm due to the in-plane compressional strain from the sample mount. Just below the band edge is a peak corresponding to the n=2 free exciton excited state. D^0X absorption peaks are too small to be unambiguously resolved in our sample since Fabry-Perot fringes complicate the spectrum. However, as will

be described, two D^0X peaks clearly emerge in differential transmission (DT) data when an on resonant pump beam excites the D^0X states.

Differential transmission data was collected by measuring the change in transmission of a weak probe beam in the presence of a stronger, chopped pump beam. Both beams were derived from the same femtosecond mode-locked Ti:sapphire laser. The spectral bandwidth of the pump was narrowed using a grating-based spectral pulse shaper. The pump beam was modulated using an optical chopper and the modulated signal was detected using a lock-in amplifier. The pump and probe beams were co-circularly polarized for the data shown. The resulting nonlinear spectrum is plotted in red at the lower portion of Fig. 5.9b. A 0.04 nm bandwidth pump beam centered at 875.03 nm reveals two sharp resonances in the spectrum corresponding to D^0X states when the pump and probe beams overlap in time. These peaks have relatively narrow linewidths of $\sim$ 1 Å, as is characteristic of D^0X transitions. The D^0X peaks are separated by 0.06 nm and the peak at highest wavelength is separated from the HH exciton by 0.70 nm (1.18 meV). The nearby proximity of the HH exciton places the D^0X peaks within the low energy tail of the HH absorption. The net overlap could be reduced by minimizing the impurity concentration of the sample, which is likely the most significant factor in contributing to the exciton broadening of this sample. Even more significant is the fact that this energy separation is quite a bit smaller than that reported in previous publications. W. Rühle *et al.* report a free exciton to

lowest D^0X state separation of 0.92 nm (1.56 meV), which is 0.22 nm (0.38 meV) larger than observed in our sample. It is most likely that the in-plane compressive strain experienced by the sample causes the free exciton transition to shift nearer to the D^0X peaks, which is an unfortunate effect, although perhaps strain could be applied to the sample in such a way as to increase the energy separation instead.

Despite the relatively high impurity concentration of this sample, quantum beats can be observed at either D^0X peak by varying the pump/ probe delay. Fig. 5.10 depicts quantum beats at the longer wavelength D^0X peak (875.03 nm) when initialized by a narrow, on-resonant pump beam. The resulting oscillation period is found to be 165 ps in the presence of the 0.4 T permanent magnet, in good agreement with the expected g-factor of 1.25 [45]. The beats show little decay over the time span shown, even in our impure sample. Beats are also evident when

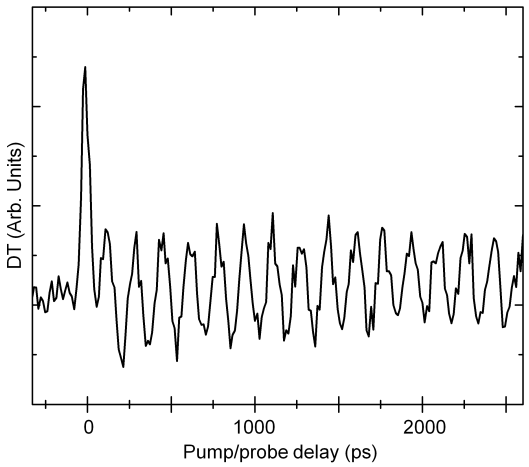

Figure 5.10 Quantum beats in bulk InP at 1.4 K, measured at the lowest energy D^0X transition. Beats initialized with a 200 μW, 0.04 nm bandwidth pump, centered at 875.03 nm. Sinusoidal decay fit gives a 7.4 ns lifetime.

scanning the delay at the higher energy D^0X transition. In contrast to the GaAs sample, in this sample the two D^0X peaks demonstrate beats that are in phase with each other, as shown in Fig. 5.11a. This difference will be discussed in the following section.

As was done in the case of GaAs, the spectral profile of the quantum beats was determined by measuring the transmission spectrum at different times relative to the quantum beat phase. In this case, measurements were taken at two times: (1) during the peak of an oscillation and (2) during the trough of an oscillation. By plotting the difference of the two spectra, one finds how the absorption spectrum is changing as a function of time due to the quantum beats. This difference data is plotted in Fig.5.11b. Two sharp peaks corresponding to the D^0X transitions emerge in the data. The fact that both peaks share the same sign demonstrates that the quantum beats at both peaks are in phase. The phase agreement is consistent with the energy diagram of Fig. 5.12a. This is in sharp contrast to the opposite beat phase of the GaAs D^0X states of the previous section. In the following section, the reason for this difference and its possible ramifications are speculated upon.

Discussion of Results in Bulk InP

Our original motivation for making the change from GaAs to InP was that the D^0X transitions in GaAs appeared to couple to both electron ground states under the same circularly polarized light. Our hope was that changing to a material that exhibited a larger energy separation between the D^0X transitions, or between the

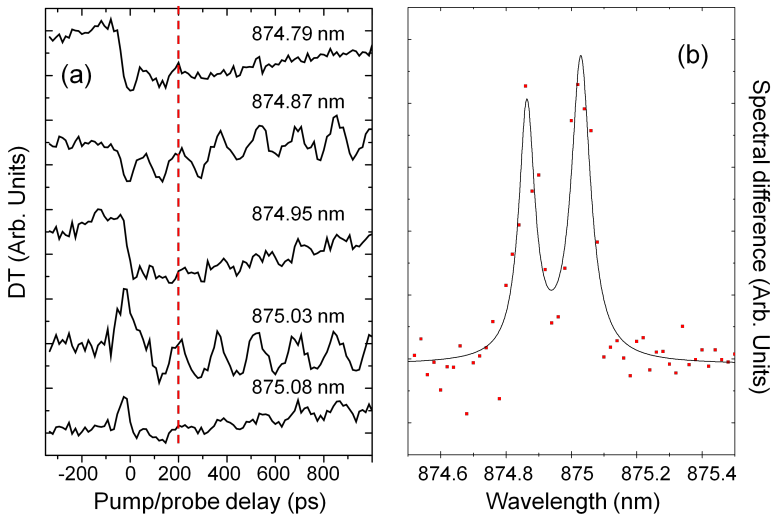

Figure 5.11 Quantum beat spectral dependence in bulk InP at 1.4 K. (a) Various detection wavelengths. (b) Spectral difference, where the spectrum taken during the trough of a quantum beat is subtracted from the spectrum taken at the peak of a quantum beat. Beats are evident at the two D^0X transitions at 874.87 nm and 875.03 nm. A two peak Lorentzian fit is used as a guide for the eye. Beats initialized with a 200 μW, 0.04 nm bandwidth pump, centered at 875.03 nm.

D^0X and free exciton transitions, would improve the efficiency of spin rotations. InP has been shown in previous publications to exhibit these properties [43, 45]. What we did not expect to find was that the transition selection rules under the same polarization of light appear to be quite different. The phase of the quantum beats measured in the previous section imply that the D^0X transitions are effectively given by the energy schematic of Fig. 5.12. In this schematic, circularly polarized light interacts with a single electron ground state, rather than both ground states as in the GaAs case. If this is true, then the inefficiency of Stark shift based spin rotations, corresponding to coupling to both DBE ground states, is not observed in InP. Thus, our switch to InP should provide a significant advantage

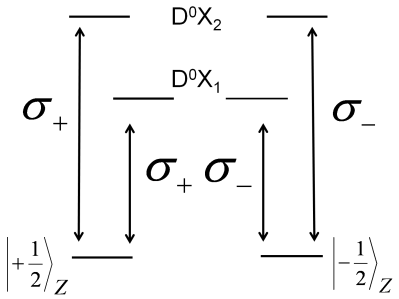

Figure 5.12 Observed D^0X transition scheme in bulk InP for circularly polarized light based on measurements of electron spin precession.

over GaAs. Unfortunately, the high impurity concentration of our sample results in the excitation of many unwanted states, even at high detunings. Modest pulse powers wipe out spin coherence as a result. A higher purity sample is necessary for further progress.

The difference in transition selection rules between InP and GaAs is unexpected. According to [53], the transitions in GaAs and InP should be qualitatively the same, other than the fact that the DBE have g-factors of opposite sign (which is undetectable for our weak external magnetic field). Therefore, assuming that the transition schemes for InP and GaAs are qualitatively the same, there are two possible causes for this difference. (1) The transition strengths of the transitions are quantitatively different in the two samples, causing different transitions to be dominant with circularly polarized light, or (2) the in-plane compressive strain on the InP sample leads to different selection rules than the free standing GaAs sample. Of course, it is also possible that D^0X states in InP and GaAs are qualitatively different. Indeed, examination of the two most prominent papers in each system,

W. Rühle *et al.* [45] for InP and V. A. Karasyuk *et al.* [41] for GaAs, reveals quite different optical selection rules for the two systems. A notable difference is the supposedly "unpolarized" transition appearing in the transitions of V. A. Karasyuk *et al.*, the like of which does not appear in the publication by W. Rühle *et al.*

By examining the D^0X transitions in InP reported by W. Rühle *et al.*, it can be seen that ignoring transitions to D^0X states with a light hole, and focusing solely on transitions which include a heavy hole would result in the same effective energy schematic as that proposed in Fig. 5.12. It could be supposed that the in-plane compressive strain has shifted the light hole D^0X states to higher energy, leaving only the heavy hole D^0X states in the detection region, since the same has happened to the free exciton light hole and heavy hole transitions. However, it has been shown in previous strain dependent measurements [54] that the D^0X transitions do not follow the free exciton transitions in this simple way. Therefore, it is unclear at this point which of the options proposed above lead to the different behavior of the InP and GaAs samples. An increased understanding of this difference could help provide an avenue for improving DBE spin control.

Chapter Summary

Through our investigations, it was found that the optical manipulation of DBE spins in bulk GaAs and InP is hindered by a limitation that was not previously

reported. D^0X transitions can couple to both DBE ground states with the same polarization of light, which decreases the effectiveness of Stark shift based spin rotations. This effect was observed in a high purity bulk GaAs sample in which quantum beats at the $L = 0$ and $L = 3$ D^0X transitions were π out of phase with each other. After switching to bulk InP, it was found that this sample did not exhibit the same behavior. The reason is not yet understood, yet its discovery may provide a new avenue for improving DBE spin control. The inherent, long lasting lifetime of ensemble electron spins in bulk semiconductors would be a highly useful spin system if its dynamics could be effectively controlled. We hope that our investigations will provide the ultrafast spin community with a new viewpoint on how the difficulties in this system can be overcome.

Additionally, our method of determining the spectral response of a sample due to the presence of oscillating electron spins can be utilized in any number of systems to help predict the feasibility of Stark shift based spin control, especially when the transition scheme is complicated, as in the case of DBEs.

CHAPTER VI

EXCITATION-INDUCED EXCITON ABSORPTION: CORRELATION-ENHANCED TUNNELING EFFECTS

Figures 6.1b, 6.2, 6.4, and 6.7-6.9 were published in the co-authored work, Ref. [55]. The total of the material presented in this chapter was obtained by the author.

Introduction

Our motivation for performing the experiments which lead to the results presented in this chapter were along the lines of obtaining an optically tunable 2DEG density for performing electron spin coherence studies. A unique type of semiconductor heterostructure, known as a mixed-type quantum well (MTQW), allows optical injection of excess electrons into the quantum well of interest. We hoped that we would be able to perform measurements on spin dynamics as a function of 2DEG density. However, several surprising results were observed during these measurements which warranted further study. Some of these results are still unexplained at the present. We focus on one of these results in which a nonlinear optical effect was observed which is the complete opposite of what is generally observed. Namely, the excitonic absorption spectra were found to increase in oscillator strength in the presence of a resonant pump, rather than decrease.

This result was found to result from a coupling between optical excitations and tunneling rates in the MTQW structure. We begin this chapter with a discussion of the properties of MTQWs and how an excess electron density can be optically generated in the quantum well of interest. We then proceed to describe the anomalous nonlinear effect mentioned above and present tunneling measurements of the sample which are shown to be directly related.

Quantum Tunneling in MTQW

MTQWs are structures in which quantum tunneling measurements can be studied and utilized. They consist of a type-I quantum well, called the wide well (WW), a type-II quantum well, called the narrow well (NW), and a barrier which separates the NW from the WW. The WW is a type-I quantum well because the lowest lying state in the conduction band is energetically lower than the lowest lying conduction band energy state in the barrier. The NW, on the other hand, is a type-II quantum well because the X-valley in the barrier is energetically lower than the lowest energy band in the conduction band of the NW. This energetic configuration, shown in Fig. 6.1b, allows electrons excited to the conduction band in the NW to trickle down through the X-valley of the barrier to the WW on a timescale of a few hundred picosecond [56]. Holes excited in the NW do not relax to the WW because there does not exist a valence band state in the barrier that lies at higher energy than the lowest valence band in the NW.

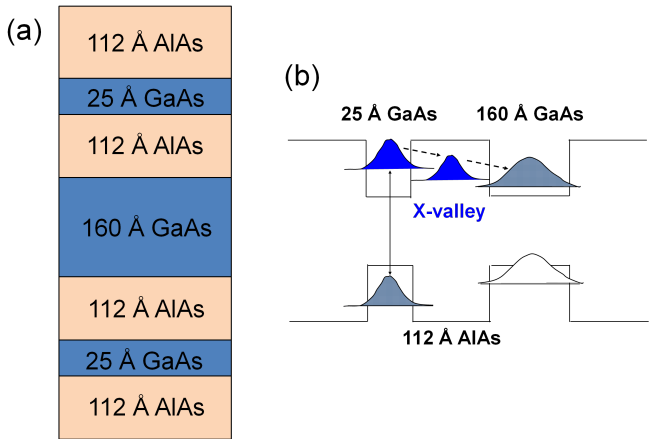

Figure 6.1 MTQW structural composition. (a) Diagram of the growth structure of the MTQW sample. The image presented is replicated three times in the sample, so that there are three wells of 160 Å, each surrounded by two wells of 25 Å. (b) Diagram of the relative energies of the conduction and valence bands in each layer of the MTQW.

Through the relaxation process described above, it is possible to inject electrons from the NW into the WW using photons of energy higher than the band gap of the NW ($\sim$ 670 nm) [56], producing spatially separated 2 dimensional electron and hole gases in the WW and NW, respectively. This allows one to control the density of electrons in the WW by varying the power of the electron injecting beam, which we call the HeNe beam, since a helium-neon laser (633 nm) was used to perform this function.

Eventually, the electrons in the WW recombine with the holes in the NW. Electrons in the WW cannot gain enough energy to return to the NW on their own. However, the valence band in the WW lies energetically higher than the valence band in the NW, thus holes in the NW can tunnel to the WW where

they quickly recombine with the electrons (ps timescale). Therefore, the lifetime of excess electrons in the WW is determined by the hole tunneling time.

The hole tunneling rate is difficult to describe analytically, and many variations on such calculations have been undertaken [57–59]. Two notable publications describe some of the main factors which determine the hole tunneling rate. A paper by I. Galbraith *et al.* [56] displays experimental data which demonstrates that the hole tunneling time increases exponentially with increasing barrier width. This should be so since the hole wavefunction's penetration into the barrier is described by an exponential.

As described in a publication by A. M. Malik *et al.* [28], holes which tunnel from the NW to the WW must satisfy both energy and momentum conservation. Fig. 6.2 depicts the valence bands of a 25 Å quantum well and a 160 Å quantum well, the parameters of the NW and WW of our sample, respectively, calculated using the 6 X 6 Luttinger-Kohn Hamiltonian (see chapter II for details on the calculation). Holes which tunnel from the NW to the WW satisfy energy and momentum conservation at points where the valence bands intersect in this figure. A direct result of this dependence is that tunneling rates ought to be sensitive to temperature variations, since the hole wave vector distribution will increase at higher temperatures. The relation of tunneling time to temperature, as shown by A. M. Malik *et al.* [28], is given by:

$$\tau \sim exp[\Delta/k_B T] \tag{VI.1}$$

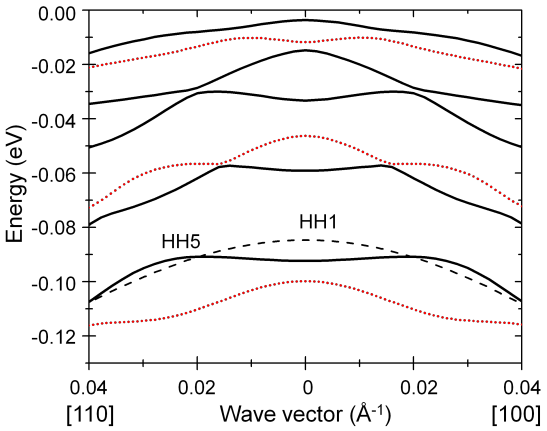

Figure 6.2 Valence band structure for a 160 Å GaAs quantum well (solid black and dotted red lines) and a 25 Å GaAs quantum well (dashed lines), calculated using the 6×6 Luttinger-Kohn Hamiltonian. In the 160 Å well, solid black lines represent heavy hole subbands, and red dotted lines represent light hole subbands. The lowest energy subband of the 25 Å well (HH1) overlaps the HH5 subband of the 160 Å well, with an energy difference of $\sim$ 6 meV between the overlap point and the $k = 0$ point of the 25 Å HH1 band.

at low temperatures, where Δ is the energy difference between the lowest subband minimum for holes in the NW and the energy at which the momentum/ energy intersection takes place in Fig. 6.2. In our sample, this difference is calculated to be around 6 meV. In addition to temperature variation, tunneling times should be directly affected by any mechanism which can induce an energy shift in the valence bands of either well, altering the points of energy and momentum overlap of Fig.6.2. Examples of such effects that can alter the tunneling time in this way are band gap renormalization [60, 61] and space charge effects [56]. Our experimental results presented in this chapter cannot be explained by these mechanisms, as will be described at the end of this chapter. But they can be explained by a mechanism similar to that described in recent publications [62, 63] in which a large enhancement

in tunneling occurs when electrons and holes directly face each other across the barrier. According to those publications, this spatial correlation is claimed to occur when electrons and holes in the bilayer form a Bose-Einstein condensate. The occurrence of a Bose-Einstein condensate is not necessary for electrons and holes to become spatially correlated across the barrier. As in our case, a small density of excitons in the WW cause electrons in the WW to behave like heavier particles. These "heavy electrons" can then be influenced by the potential dip induced by the localized positive charge of the hole across the barrier, increasing the likelihood of electrons to directly face holes across the barrier, and resulting in an enhanced tunneling rate. This interpretation of our data will be discussed in more detail at the end of this chapter.

Experimental Design

The MTQW sample used for our experiments is composed of a GaAs NW of 25 Å width, a GaAs WW of 160 Å width, and an AlAs barrier of 112 Å width, with the substrate etched away to allow for transmission measurements. The relatively wide width of the barrier results in tunneling times on the order of milliseconds [56]. Each WW is situated between two NWs in order to minimize macroscopic electric field effects due to the separation of electrons in the WW and holes in the NW. See Fig. 6.1a for a schematic of the MTQW growth structure. Photoluminescence measurements were performed using a 633 nm excitation beam and a CCD camera

for detection. Absorption measurements were performed using the broad bandwidth ($\sim$ 5 nm) of a femtosecond pulsed Ti:sapphire laser.

Tunneling measurements were performed by monitoring the transmission of the sample at the exciton resonance as a function of time after the application of a pulsed HeNe beam. In the presence of an electron gas, Coulomb interactions are screened, reducing the likelihood of forming an exciton. Thus, the exciton absorption strength becomes a function of the electron gas density. As electrons and holes recombine through the hole tunneling process, the exciton absorption line regains strength, and this change in the exciton absorption can be monitored as a function of time, giving a measure of the hole tunneling rate. The relatively large barrier between the WW and NW in our sample leads to tunneling dynamics on the order of milliseconds. On this timescale, an acousto-optic modulator (AOM) can be used to produce HeNe pulses on the order of microseconds and an oscilloscope can be used to monitor the transmission at the exciton resonance as a function of time. The experimental setup is shown in Fig. 6.3. A third beam, resonant with either the LH or HH exciton absorption, is derived from a separate Ti:sapphire laser. The mode-locking feature was negated so that it could be used in CW mode to excite an excitonic population. This beam also passed through an AOM to allow the beam to be pulsed, or remain CW, as needed.

The sample was bonded to a sapphire disc using a low strain adhesive (Norland Optical Adhesive 88) and mounted in an exchange gas cryostat. The long lifetime

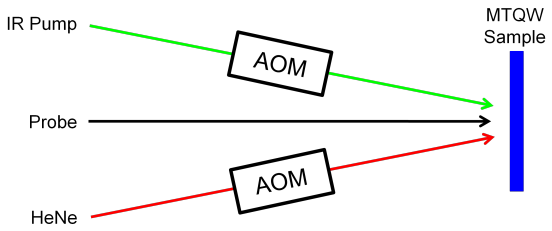

Figure 6.3 Three beam setup for MTQW measurements. After passing through the sample, the probe is sent to a spectrometer, where a single wavelength is selected, and then the signal is sent to a lock-in amplifier for absorption measurements, or an oscilloscope for tunneling measurements.

of the photo-injected electron population in the WW results in a sample which is highly sensitive to stray room light. For this purpose, the sample was subjected to complete darkness.

Electron Injection

Electron injection into the WW is confirmed through PL measurements. Fig. 6.4a displays PL in the spectral region of the HH exciton of the WW. In the presence of a 100 μW, 800 nm CW beam, which excites electron/ hole pairs in the WW only, emission due to exciton recombination is clearly seen at 810.4 nm. The addition of a 633 nm HeNe beam, which has enough energy to excite electron/hole pairs in the NW, causes a second peak to emerge at lower energy than the exciton emission line, which corresponds to trion recombination. Trions are only formed in the presence of an excess electron gas, and thus the emergence of this emission line is evidence of the relaxation to the WW of electrons photoexcited in the NW.

As mentioned in the previous section, excess electrons injected to the WW

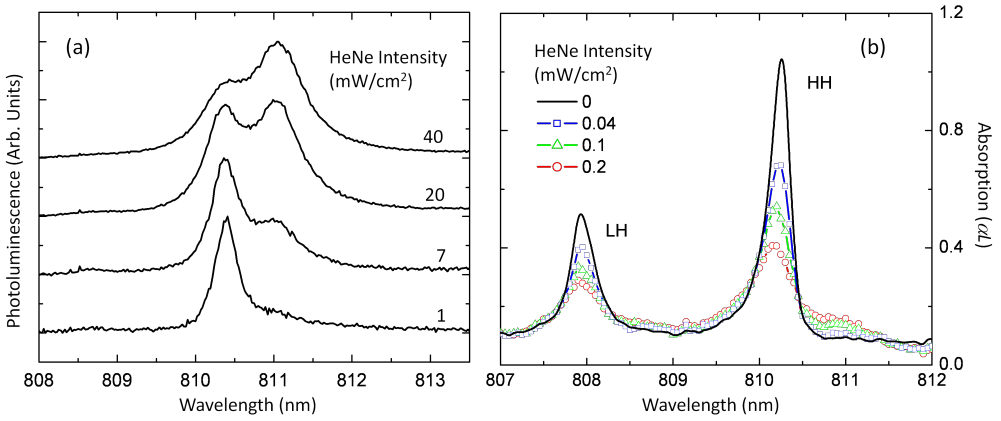

Figure 6.4 GaAs MTQW spectra versus HeNe intensity. (a) PL from the WW at 12 K versus HeNe intensity. At low HeNe powers, the exciton peak is evident around 810.3 nm. At higher HeNe powers, the trion peak emerges and eventually dominates the exciton PL. (b) Absorption of the WW at 12 K versus HeNe intensity. Very small intensities bleach the exciton resonance. A small trion peak is evident at higher wavelength as the HeNe power is increased.

in this process result in a significant reduction in the exciton absorption line strength. Fig. 6.4b displays the exciton absorption of the WW. In the absence of an excess electron gas, the exciton absorption lines are relatively narrow (0.27 nm), demonstrating the high quality of the sample. Upon application of the electron injecting HeNe beam, the exciton absorption strength rapidly diminishes. A modest intensity of 0.04 mW/cm^2 is enough to reduce the absorption strength to half of its initial value. This power is comparable to powers produced by room light, and thus measurements of this sample were taken in complete darkness. The weakening of the exciton absorption is accompanied by a broadening of the exciton peak and the emergence of a weak trion peak at lower energy. These features are all directly related to the presence of the injected electron gas, which screens

exciton formation, causes broadening of the exciton line through scattering, and increases the likelihood of trion formation. The excess electron gas density can thus be monitored through the large decrease in the exciton absorption line.

A HeNe beam of intensity 1 mW/cm^2 is estimated to generate an excess electron gas density of order 10^{10} cm^{-2}. This estimate was found in two ways. Firstly, our measurements can be compared to publications in which the trion PL strength is measured versus electron density [64] or papers in which the exciton screening is measured versus electron density [65]. Secondly, this number can be estimated through a simple rate equation calculation. The rate equation for the electron density is given by:

$$\frac{dN}{dt} = R - \frac{1}{\tau}N \tag{VI.2}$$

where N is the electron population, R is the rate at which electrons are injected into the well, and τ is the lifetime of the electron population (the hole tunneling time). R is the photon flux per unit time absorbed by the sample $\frac{\Delta I}{\hbar\omega}$, where ΔI is the portion of the intensity of the injection beam absorbed and $\hbar\omega$ is the energy of a photon of angular frequency ω. The steady-state solution is given by:

$$N = \frac{\Delta I}{\hbar\omega}\tau \tag{VI.3}$$

The intensity absorbed by the sample is given by Beer's law:

$$\Delta I = I_0 - I_{out} = I_0(1 - e^{-\alpha L}) \tag{VI.4}$$

where I_0 is the input intensity, I_{out} the emerging intensity, α the frequency

dependent absorption coefficient, and L the length of the sample. The HeNe spot size in our experiment was measured to be 3.46 mm. We use the value of bulk GaAs at the wavelength $\lambda = 633$ nm for our absorption coefficient, which is given by $\alpha = 3.9 \times 10^4$ cm^{-1} [66]. For a quantum well, this number will be somewhat smaller, and thus this α will actually give us an electron density which is an upper limit on the true value. $L = 5$ nm for photons absorbed in two narrow wells of length 2.5 nm each. Two wells are used since each WW is surrounded by two NWs (see Fig. 6.1a). With these numbers, we find $\Delta I = 8.2 \times 10^{-7}$ W/cm^2. Plugging this number into (VI.3), we find the estimated electron density to be $N = 2.6 \times 10^{10}$ cm^{-2} for a lifetime of $\tau = 10$ ms.

Tunneling Measurements

The tunneling of holes from the NW to the WW can be observed by monitoring the time dependent bleaching of the exciton absorption. A pulsed HeNe injects an excess electron gas into the WW, which causes the transmission at the exciton resonance to increase sharply on a picosecond timescale. The transmission at the exciton resonance then recovers to its original value slowly over a period of several milliseconds (for our sample with relatively large barrier width). A typical time trace is displayed in Fig. 6.5.

Monolayer interface fluctuations in the NW cause the holes in the NW to be spatially confined. This is because the NW is so narrow that a difference of a single

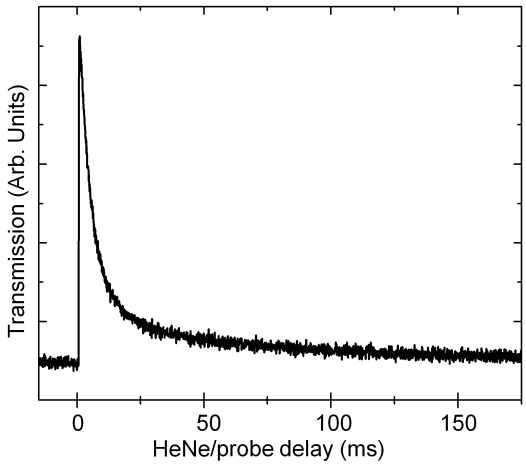

Figure 6.5 Typical measurement of hole tunneling time at 12 K. Electrons injected into the WW with a HeNe with an intensity of 6 mW/cm^2 and 0.4 ms duration.

layer of atoms in one section of the NW relative to another causes a significant difference in the local well width. Monolayer fluctuations in GaAs cause the well width to fluctuate by roughly half of the lattice spacing (a = 5.653 Å) for a zinc blende crystal structure from the nominal value. In the WW, such fluctuations in the well width are negligible, but in the NW these fluctuations cause the valence bands to broaden by as much as 25 meV. Fig. 6.6 shows the valence band structure of a 22.5 nm and a 27.5 nm well, calculated using the transfer matrix method described in chapter II. The difference between the two plots is filled in to represent the broadening induced by the monolayer fluctuations.

We expect that the tunneling process will exhibit a distribution of decay components due to the variation in local hole environments as a result of the monolayer fluctuations. We find that the tunneling rate appears to be well

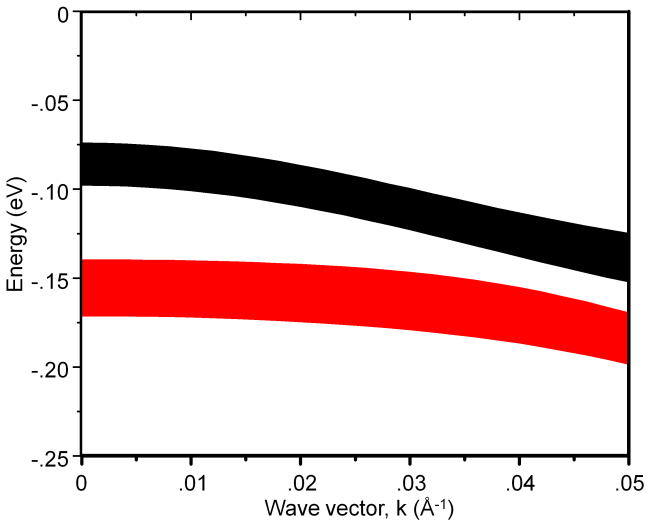

Figure 6.6 Calculated valence band broadening due to ± 2.5 nm monolayer fluctuations in NW.

represented by a double exponential, where the holes at the bottom of an energy distribution exhibit the longest lifetime. A double exponential fit is plotted in red in Fig. 6.7a as an example.

Temperature Dependence

As predicted by A. M. Malik *et al.* [28], the tunneling time demonstrates temperature dependence. Fig. 6.7a depicts tunneling measurements taken over a range of temperatures, with a HeNe pulse of 0.4 ms duration and an intensity of 6 mW/cm^2. The tunneling times obtained from a double exponential fit are plotted in Fig. 6.7b. From these fits, it is clear that the fast component of the double exponential fit decreases exponentially with increasing temperature, as described by (VI.1), with decay constant $\Delta = 0.24$ meV. The slow tunneling component

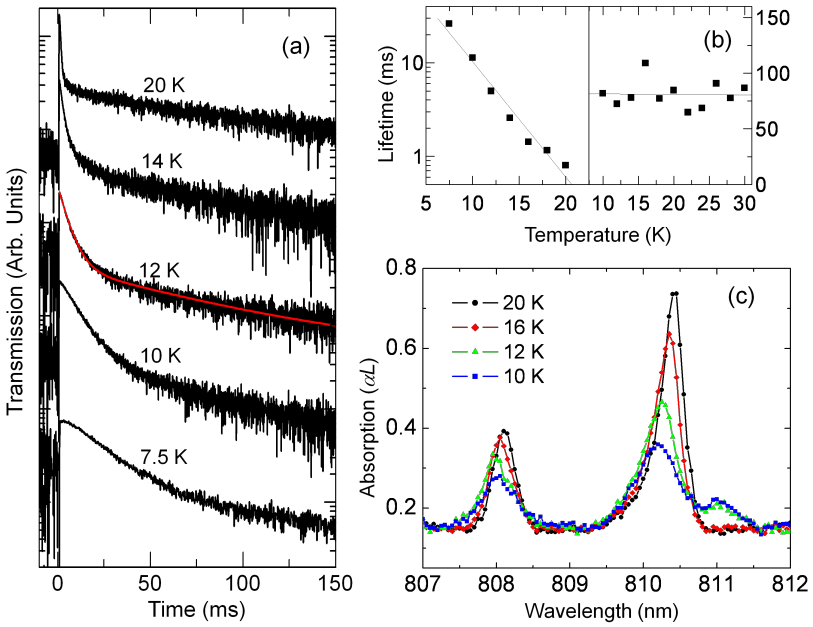

Figure 6.7 Temperature dependent measurements of the MTQW sample. (a) Transmission at the HH exciton absorption versus HeNe/ probe delay time at various temperatures. Pulsed HeNe duration was 0.4 ms, with a peak intensity of 6 mW/cm^2. (b) Double exponential fit lifetimes for the data shown in (a). An example fit is overlaid over the 12 K data in (a). Lines are overlaid in the graph as a guide to the eye. (c) Exciton absorption spectra at various temperatures in the presence of a 0.2 mW/cm^2 CW HeNe.

seems to be temperature independent in the range of temperatures measured in the experiment. The nearly temperature independent lifetime of the slow fit component further supports the assignment that it is due to holes which remain at the bottom of the energy distribution in the valence band.

The temperature dependence of the tunneling results in an anomalous temperature dependence of the exciton absorption. The exciton absorption is generally observed to increase in strength with lower temperature, which is accompanied by a narrowing of the linewidth. In this case, the opposite is

observed. Fig. 6.7c plots the exciton absorption in the presence of a 0.2 mW/cm^2 HeNe over a range of temperatures. At 10 K, the exciton absorption is significantly decreased due to electron screening and scattering processes, and is accompanied by the emergence of a trion peak at lower energy. As the temperature of the sample is increased, the exciton absorption red shifts, as expected [67]. However, the absorption strength also increases, and the linewidth narrows. Although this effect is not observed in conventional quantum wells, in which the exciton absorption strength increases with decreasing temperature, its appearance in this case is clearly a result of the hole tunneling dependence on temperature. As the temperature of the sample increases, the hole tunneling rate increases, which leads to a smaller net excess electron population in the WW, which diminishes the screening of exciton formation. For this reason, in subsequent measurements, it must always be kept in mind that measurements at different temperatures cannot be directly related since the steady-state electron population will vary.

Excitation-Induced Exciton Absorption

One of the most bizarre effects that we have come across in this sample is an excitation-induced exciton absorption, in which a beam resonant with either exciton absorption causes the exciton absorption line to increase in absorption strength, rather than decrease as is generally observed [68]. As will be explained, this effect

is directly related to a change in the hole tunneling rate due to the presence of a low density of excitons in the WW.

The absorption of our sample is shown in Fig. 6.8 in solid black in the absence of any beam other than a weak probe beam. With the addition of a CW HeNe beam, the absorption strength of the exciton decreases due to the screening of a population of injected electrons from the NW, as explained in previous sections. In the remaining plots of Fig. 6.8, the HeNe power is 0.2 mW/cm^2, which is large enough to induce a significant decrease in the exciton absorption strength. Leaving this HeNe power constant and applying a third beam to the sample, which we will call the infrared (IR) pump, resonant with either the LH or HH exciton, causes the exciton absorption strength to increase. A modest IR pump intensity of 0.03

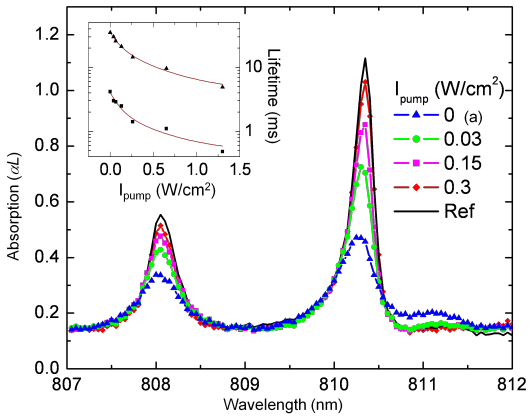

Figure 6.8 Excitation-induced exciton absorption. Absorption of the WW exciton spectra in the presence of a 0.2 mW/cm^2 CW HeNe and various CW IR pump intensities at 12 K. The absorption in the absence of both HeNe and IR pump is shown in solid black for reference. The inset plots the hole tunneling times as a function of the power of an applied CW IR pump, with the solid curves included as a guide to the eye.

W/cm^2 causes a 100% increase in the exciton absorption. An intensity of 0.3 W/cm^2 results in a near completely recovered exciton absorption. It appears as though the IR pump removes the effect of the HeNe beam. The purpose of the HeNe beam is, of course, to inject electrons into the WW. Therefore, it seems as though the IR pump is depleting the population of the excess electron gas. This process is confirmed in tunneling measurements, as described below.

Fig. 6.9b depicts the hole tunneling at 12 K initiated by a pulsed HeNe in the presence of various CW IR pump powers. The hole tunneling rate is found to increase with increasing IR pump power. These relatively low IR pump powers are comparable to those pump powers shown in Fig. 6.8 which induce a large increase in the exciton absorption strength. Double exponential fits of the hole tunneling time as a function of pump power are shown as an inset of Fig. 6.8. It is clear that the increasing absorption in Fig. 6.8 is directly related to an increase in the hole tunneling time. A full explanation of the physical process behind this effect will be explained towards the end of this chapter.

It is important to determine the time for which this recovered exciton absorption can persist. By setting the electron injecting HeNe to CW and instead setting the IR pump to be pulsed by an AOM, we can measure the time it takes for the absorption to be degraded once again by the HeNe. In other words, we can measure how long it takes for the HeNe to replenish the excess electron gas that was removed by the IR pump. Fig. 6.9a depicts this process at 12 K, where a 0.2 mW/cm^2 CW HeNe

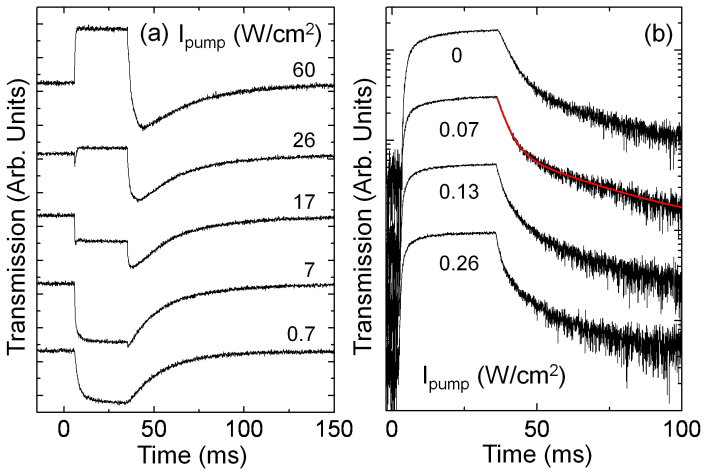

Figure 6.9 Tunneling dependence on IR pump power at 12 K. (a) 0.2 mW/cm^2 CW HeNe pump and a pulsed IR pump of various intensities and 30 ms duration. (b) CW IR pump of various powers and a pulsed HeNe of peak power 10 mW/cm^2 and 32 ms duration. A double exponential fit is shown as the solid red line as an example. The full set of fits are shown as the inset of Fig. 6.8.

remains constant, and an IR pump of 30 ms duration is incident on the sample. The increase in the exciton absorption due to the pump pulse results in a dip in the transmission. For the full range of powers demonstrated in Fig. 6.9a, the lifetime of the transmission dip is independent of the IR pump power. Rather, as can be shown by a simple rate equation calculation, the recovery time is dependent upon the excess electron lifetime, which will be shown below. At higher powers, the exciton population excited by the IR pump beam leads to saturation of the exciton absorption. This happens at powers much higher than those which lead to an increased tunneling rate. The exciton density can be estimated using (VI.3), with $\alpha L = 1$, and $\tau = 1$ ns, and a spot size of 110μm, to be 6.7×10^8 cm^{-2} with an intensity of $I = 0.26$ W/cm^2. Thus, exciton densities on the order of 10^{10} cm^{-2}

will serve to bleach the exciton absorption, whereas the enhanced tunneling occurs at exciton densities on the order of 10^8 cm^{-2}.

It can be shown that the lifetime of the transmission dip in Fig. 6.9a, which follows the electron density as it is re-injected into the sample, follows the hole tunneling time using a simple rate equation:

$$\dot{N} = R - \frac{1}{\tau}N \tag{VI.5}$$

where N is the electron density, R is the rate at which electrons are replenished in the WW by the HeNe, and τ is the electron lifetime (i.e. hole tunneling time). This differential equation has a simple solution, given by:

$$N = (N_0 - R\tau)e^{-t/\tau} + R\tau \tag{VI.6}$$

Hence, the re-injection time of the electrons is given by τ, the hole tunneling time. This result further confirms that the effect of the IR pump, which excites an exciton density, is to decrease the electron population.

Dawson Sample

A second sample was investigated to see if it would demonstrate the same enhanced tunneling behavior in the presence of an exciton resonant pump. The NW width was 25 Å of GaAs, the WW was 68 Å of GaAs, and the barrier was 108 Å of AlAs. These numbers are to be compared to the parameters of the sample investigated above, which will be referred to as the Prineas sample, and are

a 25 Å GaAs NW, 160 Å GaAs WW, and 112 Å AlAs. The secondary sample was provided to us by Phil Dawson, whose research on MTQWs has produced a collection of papers which are among the more prominent publications on MTQW systems. Samples similar to this one are used in many of his papers. The similarity in barrier widths suggests that this sample may demonstrate the same sort of qualitative behavior as our sample, although the significantly different WW width may result in differing quantitative values.

Indeed, the Dawson sample does demonstrate the same qualitative behavior as the Prineas sample, although the quantitative values for these behaviors are quite

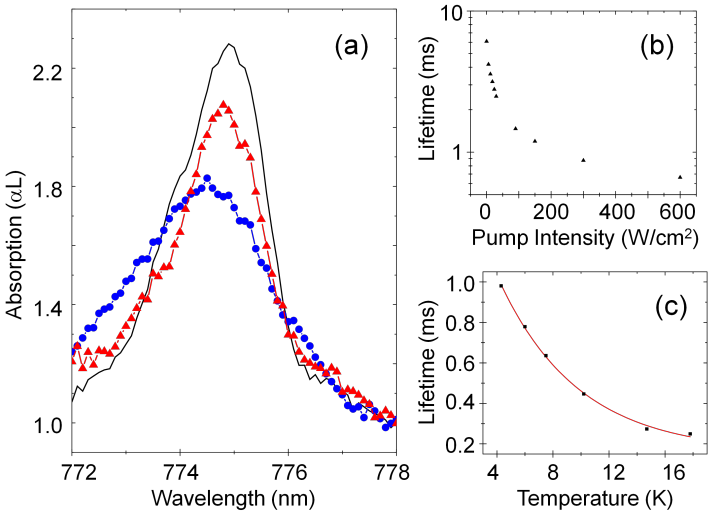

Figure 6.10 Dawson sample measurements. (a) Absorption of the HH exciton in the presence of a 75 mW/cm^2 CW HeNe and no IR pump and a 15 W/cm^2 IR pump, for the blue circle plot and the red triangle plot, respectively. The absorption in the absence of both HeNe and pump is shown as the solid black line for reference. (b) Exponential fit of the transmission decay lifetime as a function of CW IR pump power at 1.6 K. (c) Exponential fit of the transmission decay lifetime as a function of temperature.

different. The excitation-induced absorption is shown in Fig. 6.10a. A 75 mW/cm^2 CW HeNe beam serves to bleach the exciton absorption through the screening of injected electrons from the NW to the WW. By applying an additional beam, resonant with the heavy hole exciton absorption, the exciton absorption strength increases. As in the Prineas sample, an increase in tunneling rates is observed both through the application of the IR pump and also through an increase in temperature, as shown in Fig. 6.10b and c, respectively. Single exponential fits were used to model the tunneling decay rates in the Dawson sample.

It should be noted that the linewidth of the heavy hole exciton in this sample is much greater than that in the Prineas sample. Here the full width at half maximum is about 2 nm, whereas in the Prineas sample, it was 0.27 nm. This large inhomogeneous broadening will cause the valence band energy overlap between the NW and WW to be much larger, leading to faster tunneling times. The tunneling times in the Dawson sample are on the order of 1 ms. The reader may wish to see the publication by A. M. Malik *et al.* [28] in which they have calculated the valence band structure for this sample, although their calculation does not take into account the large inhomogeneous broadening of the sample, which can be a significant factor in the valence band overlap.

The HeNe power necessary to induce a similar bleaching of the exciton absorption as the Prineas sample is much higher, which is a result of the faster tunneling times. The IR power required to induce an enhanced tunneling time are

also significantly larger, as evidence by the data shown in Fig. 6.10b. It is likely that the large inhomogeneous broadening of the sample results in a less sensitive enhanced absorption effect, but this is only speculation at this point.

Interpretation of Enhanced Tunneling

As described in the introduction to this chapter, a variety of factors are known to alter the hole tunneling rate in a MTQW system. However, in our attempt to understand the experimental data presented in this chapter, we were forced to rule out many of these. First of all, the increased tunneling rate cannot be due to lattice heating by the IR pump. Such an effect would result in a spectral red shift reminiscent of the data shown in Fig. 6.7c. The absence of a red shift in the data of Fig. 6.8 demonstrates that the IR pump does not heat the sample to any notable extent. Additionally, the increased tunneling times due to the IR pump show qualitatively different behavior than the increased times due to a temperature increase, which is evident by the fast and slow decay fit plots shown in Fig. 6.7b and the inset of Fig. 6.8. An increased temperature shows a significant change in only the fast decay component of the tunneling whereas the IR pump induced increase effects both decay components. These measurable quantities provide evidence of what is already quite obvious, which is that an IR pump of 0.3 W/cm^2 is far too weak to induce a noticeable increase in lattice temperature, and thus its ability to increase the hole tunneling time must be due to something qualitatively different.

The excitation of carriers in the WW can induce a shift of the WW valence bands through a process known as band gap renormalization (BGR) [60, 61]. However, such effects are known to occur only at carrier densities several magnitudes larger ($\sim 10^{12}$ cm^{-2}) than the exciton densities generated in our measurements ($\sim 10^{8}$ cm^{-2}), which rules out BGR as a possible mechanism. Also, the increased tunneling rate cannot be explained by space charge effects [56] since the IR pump only excites excitons in the plane of the WW and thus cannot contribute to a macroscopic electric field in the growth direction of the sample.

An effect which makes more sense, both quantitatively and qualitatively, is a correlated tunneling effect in which electrons in the WW become correlated with holes in the NW through the exciton excitation, which can greatly increase the hole tunneling rate, similar to the enhanced tunneling mechanism of the Bose-Einstein condensate (BEC) of Ref. [62, 63]. Holes in the NW create a potential dip in the WW through the Coulomb interaction. Obviously, the magnitude of this dip is dependent on the barrier width. Fig. 6.11 demonstrates the magnitude of the Coulomb potential as seen by a negative charge in the WW due to a positive charge in the NW, as a function of its position in the plane of the WW. The dielectric constant for GaAs $\epsilon_r = 12.9$ was used, and the particles are assumed to be placed at the center of each well along the growth direction. For the barrier width of our sample, 112 Å, a negative charge in the WW feels a potential dip of approximately 5 meV due to a hole in the NW. This dip is too weak to trap conduction band

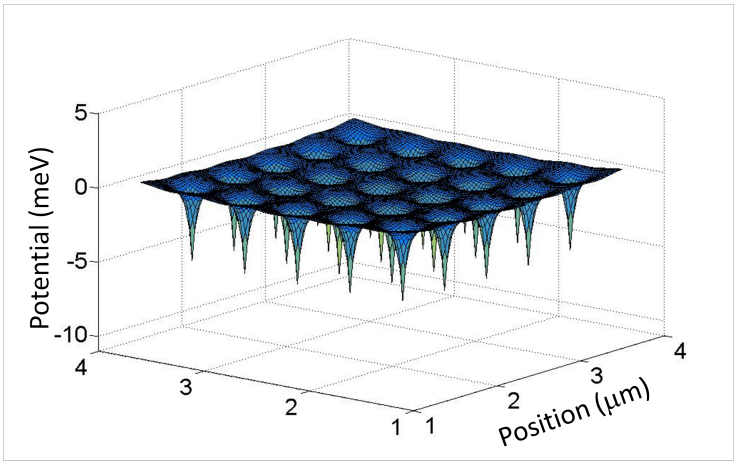

Figure 6.11 Coulomb potential due to holes in the NW as seen by electrons in the WW. The localization of holes due to monolayer fluctuations causes potential fluctuations in the WW, which are on the order of 5 meV. The hole locations will be random, rather than ordered as the figure suggests.

electrons, even at low temperatures, since they have kinetic energies on the order of 22 meV. This value of kinetic energy was determined by finding the energy of an electron in the lowest conduction subband by numerical application of the shooting method [23].

In the presence of the IR pump, excitons are excited in the WW, which can combine with excess electrons and form negatively charged trions. These particles are much heavier than electrons, and thus are more easily influenced by the potential fluctuations due to the holes in the NW. As a result, charges across the barrier can become spatially correlated with the holes in the NW. This spatial correlation leads to a great increase in the hole tunneling time, reminiscent of the increased tunneling of a BEC. It should be noted that the condition that the carriers form a BEC is not necessary for the increased tunneling rate. The only necessary condition is that

the electrons and holes are spatially correlated. In our sample, electrons cannot become spatially correlated with the holes in the NW unless they are in the presence of excitons. Excitons can combine with electrons to form trions, a much heavier particle. Additionally, electrons can be correlated with, or dressed by excitons in such a way that they behave as a much heavier particle [69]. In either case, the electron is effectively transformed into a heavier particle, which greatly increases its chance of being influenced by the positively charged holes in the NW. In this way, the intralayer correlations between electrons and excitons can significantly influence the interlayer correlation between electrons and holes, leading to large increases in the hole tunneling rate.

Chapter Summary

The focus of this chapter was on a newly observed enhanced tunneling mechanism of holes in a MTQW structure. The tunneling rate was found to be greatly increased in the presence of an IR pump which excited a low density exciton population in the WW. An increased tunneling rate lead to the unusual observation that the exciton absorption line was greatly enhanced in the presence of a resonant pump beam. Although the mechanism of the enhanced tunneling rate remains undetermined, we have proposed a correlation scheme which is consistent with all of our observations, in which the intralayer correlation between electrons and excitons can affect the interlayer correlations between electrons and holes,

leading to an enhanced hole tunneling rate. Explanations were given for why other better known mechanisms were ruled out. It is our hope that further investigations into this matter will unambiguously reveal the underlying physics leading to this effect.

CHAPTER VII

CONCLUSION

Electron spin control was investigated in two different semiconductor systems. The first, presented in chapter IV, was a two-dimensional electron gas in a CdTe quantum well. The second, presented in chapter V, was donor-bound electrons in bulk GaAs and InP. We demonstrated the ability to induce complete electron spin rotations of a two-dimensional electron gas. However, we found that the ability to rotate electron spins in bulk semiconductors is hindered by the unique optical selection rules of the donor-bound electron transitions, which has prevented full π rotations of DBE spins up to this point.

We have focused on off-resonant, Stark shift based spin rotations since rotations that utilize resonant excitation introduce significant decoherence to the spin system. In both systems, we investigated the effect that a Stark shift will produce on the electron spins. For spins in a 2DEG, a circularly polarized pulse applied below resonance will interact with one electron ground state, inducing a net energy splitting between the two electron ground states, resulting in a rotation. For DBE spins, we observed that a circularly polarized pulse applied below resonance will interact with both electron ground states, resulting in a smaller net energy difference via the optical Stark effect. This effect was determined by observing the evolution

of the nonlinear spectrum as a result of the precessing electron spins. Our method for determining the contribution of nearby resonances on Stark shift based rotations should be universally applicable, allowing researchers to determine the likelihood of realizing spin rotations in other systems with complicated transition structures.

The spin properties of donor-bound electrons are admittedly better than those of a two-dimensional electron gas. The difference is a result of the mobile nature of the two-dimensional electron gas as opposed to the localized donor-bound electrons. This inherent mobility of a two-dimensional electron gas leads to dephasing through the Rashba and Dresselhaus spin-orbit interactions, which are momentum dependent. Donor-bound electrons, on the other hand, experience dephasing through the weaker hyperfine coupling between the electron spin and the spins of lattice nuclei. The lifetime of donor-bound electron spins can thus be several orders of magnitude longer than in a two-dimensional electron gas, although it should be noted that nonmobile electrons can be utilized in a two-dimensional electron gas as well under the proper conditions.

Full donor-bound electron spin control remains elusive. However, as we have shown, complete spin control of a two-dimensional electron gas can be realized. Unfortunately, spin lifetimes of a 2DEG are limited to tens of nanoseconds. Applications utilizing 2DEG spins must conform to the limited lifetime unless the spin lifetimes can be prolonged through manipulation of electron mobility or the Rashba and Dresselhaus spin-orbit interactions.

The ability to realize rotations of electron spins in modulation-doped quantum wells has allowed for investigations into more elaborate spin control schemes, such as the two pulse technique described theoretically by P. Chen *et al.* [29] and recently demonstrated by T. Sweeney *et al.* [33]. A future project that would be useful for quantum computing applications would be to develop an adaptive control algorithm that could efficiently determine the optimum set of control parameters that would induce the highest fidelity spin rotations, quickly varying experimental parameters and analyzing the results. Once devised, such a technique could be universally applicable to other spin control systems.

As described in chapter VI, while attempting to realize a controllable density 2DEG, we observed the strange effect that a small density of excitons in the wide well of a mixed-type quantum well can result in an enhanced tunneling rate of holes from the narrow well to the wide well. Our proposed mechanism for this effect is based on an enhanced spatial correlation of electrons and holes across the barrier due to the presence of a low density of excitons. The spatial correlation results in an increased hole tunneling rate. The coupled intralayer with interlayer correlations involved in this effect present a wealth of dynamics that remain to be probed.

The excitation-induced exciton absorption realized in this system could find applications as an optical switch. Using this effect, the exciton absorption would greatly increase in the presence of adequately strong light that excites electron/ hole pairs in the wide well, while the absorption strength would remain small in

the presence of only weak intensities. The sample would then be used to dim the emerging laser power when it exceeds a given limit.

A difficulty that must be overcome is learning to adjust the response time as well as the sensitivity of the changing absorption. In our sample, the response time of this effect is on the order of 10 ms, and the response is very sensitive. However, investigations into another sample provided by Phil Dawson revealed that a variation of the sample parameters can significantly increase the response time (< 1 ms) and reduce the sensitivity of the sample. A lot of work can be done to understand how variations in sample parameters can affect the excitation-induced absorption effect.

APPENDIX A

CALCULATION OF ABSORPTION SPECTRA COMPLICATED BY FABRY-PEROT INTERFERENCE

Fabry-Perot (FP) interference is a common phenomenon, which results from the interference of a beam with itself as it reflects off the surfaces of a thin film, as shown in Fig. A.1. Near a strong absorption peak, like the exciton peak in our bulk GaAs sample, the index of refraction is quickly changing versus wavelength, and thus the FP calculation has an added complication. The calculation is presented here for the interested reader, and utilizes basic electricity and magnetism techniques. Further reading can be found by M. Born and E. Wolf [70] and Y. Zhu *et al.* [71].

As a beam enters a thin film, it reflects inside the material an infinite number of times. Each reflected beam makes two passes through the material and experiences

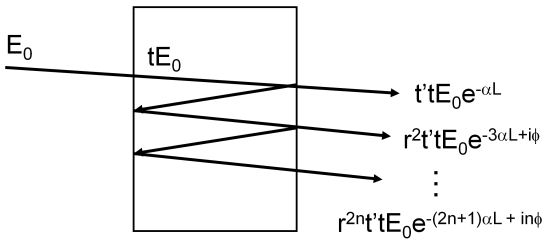

Figure A.1 Fabry-Perot interference in a thin film. The electric field is multiplied by the transmission coefficients t and t' for transmission at each surface and reflection coefficient r for reflection at each surface. It experiences absorption through each pass of the sample, and accumulates phase ϕ at each pass. The infinite series of beams emerging from the sample adds together to give the total electric field.

two lengths of the material in absorption. The infinite series of beams emerging from the film, shown in Fig. A.1, interferes and forms the total outgoing electric field:

$$E = TE_0 e^{-\alpha L} \sum_{p=0}^{\infty} R^{2m} e^{-m(2\alpha(\omega)L + i\phi)}, \qquad \phi = 2\pi \frac{2L}{\lambda / n(\omega)} \tag{A.1}$$

where $T = t't$, $R = r^2$, L is the length of the sample, $\alpha(\omega)$ is the frequency dependent absorption coefficient, $n(\omega)$ is the frequency dependent refractive index, ϕ is the accumulated phase after passing through two lengths of the sample, and λ is the vacuum wavelength. The infinite series has a well known closed form solution:

$$\sum_{m=0}^{\infty} r^m = \frac{1}{1-r}. \tag{A.2}$$

Which simplifies (A.1) to:

$$E = \frac{TE_0}{1 - Re^{-(2\alpha(\omega)L + i\phi)}} \tag{A.3}$$

The intensity is then given by:

$$I = E^* E = \frac{T^2 E_0^2}{(1 - Re^{-2\alpha(\omega)L})^2 + 4R^{-2\alpha(\omega)L} \sin^2(\frac{\phi}{2})} \tag{A.4}$$

It remains to provide the forms of $\alpha(\omega)$ and $n(\omega)$. According to classical electricity and magnetism [72] (after applying the square root of a complex number) these are given by:

$$n(\omega) = \sqrt{\frac{\sqrt{Re[\frac{\epsilon(\omega)}{\epsilon_0}]^2 + Im[\frac{\epsilon(\omega)}{\epsilon_0}]^2} + Re[\frac{\epsilon(\omega)}{\epsilon_0}]}{2}} \tag{A.5}$$

$$\alpha(\omega) = \sqrt{\frac{\sqrt{Re[\frac{\epsilon(\omega)}{\epsilon_0}]^2 + Im[\frac{\epsilon(\omega)}{\epsilon_0}]^2} - Re[\frac{\epsilon(\omega)}{\epsilon_0}]}{2}} \tag{A.6}$$

where $\frac{\epsilon(\omega)}{\epsilon 0}$ is the dielectric contstant:

$$\frac{\epsilon(\omega)}{\epsilon_0} = 1 + \frac{Ne^2}{\epsilon_0 m} f_0(\omega_0^2 - \omega^2 - i\omega\gamma_0)^{-1} \tag{A.7}$$

This form of $\epsilon(\omega)$ gives the absorption a Lorentzian lineshape. To convolve this with a Gaussian lineshape, we allow a distribution of absorption frequencies ω', weighted by a Gaussian

$$f' = f_0 e^{-\frac{(\omega' - \omega_0)^2}{2\gamma'^2}}, \tag{A.8}$$

where ω_0 is the center frequency, and γ' is the Gaussian linewidth. The dielectric constant becomes:

$$\frac{\epsilon(\omega)}{\epsilon_0} = 1 + \frac{Ne^2 f_0}{\epsilon_0 m} \int e^{-\frac{(\omega' - \omega_0)^2}{2\gamma'^2}} (\omega'^2 - \omega^2 - i\omega\gamma_0)^{-1} d\omega' \tag{A.9}$$

where γ' is the Gaussian distribution linewidth. From here, we can numerically solve for the transmission of the sample, using the linewidths and the constant multiplying the integral above, as variable parameters to find the best fit for the experimentally measured absorption spectrum. A Matlab script is included in appendix B which performs this calculation.

APPENDIX B

MATLAB SCRIPTS FOR NUMERICAL COMPUTATIONS

This appendix collects the Matlab scripts that were written for obtaining numerical results presented in this dissertation. Included are the following scripts:

1.) SpinFlip.m and SpinFlipODE.m

2.) FP.m

3.) QWValenceBands.m

SpinFlip.m was used to solve the optical Bloch equations for the results presented in chapters 3 and 4. SpinFlipODE.m is an accompanying file which SpinFlip.m calls for solving a differential equation. FP.m was used to calculate the absorption of our bulk GaAs sample when complicated by Fabry-Perot interference, shown in Fig. 5.2c of chapter 5. QWValenceBands.m solves for the band structure of a semiconductor quantum well using the transfer matrix method, described in chapter 2. Whereas the first two programs can run almost instantaneously, the third can take a few minutes for obtaining a full range of results such as that shown in Fig. 2.3 and Fig. 6.2.

```
% SpinFlip.m
% Written by Carey Phelps working in the Wang Laboratory at the University
% of Oregon.
%
% The purpose of this program is to simulate the optical control of
% electron spin coherence by applying a short pulse to a three level
% system. The system is an L-type system written in the z-basis of the
% electron spins {|z⟩, |T⟩, |z'⟩}, defined as the growth direction of the
% sample. A magnetic field is applied along the x-direction (Voigt
% geometry) and the Hamiltonian is written in the rotating frame of the
% applied field frequency.
%
% The program is simple and basically just asks the differential equation
% solver ode45 to solve the optical Bloch equations for whatever parameters
% are chosen.
%
% Unit of time is picoseconds
%
% To test that the program is working properly, one can apply a 2pi pulse
% to a system which has no decay and see that, when the electron spin is in
% the y-axis of the Bloch sphere, the spin is flipped 180 degrees. To do
% so, set the parameters in this file as the following:
%           tspan = [0:.1:250];
%           y0 = [1,0,0,0,0];
% Also, set the parameters in the accompanying file "SpinFlipODE.m" as:
%           mu = 1;
%           G = 0;
%           g = 0;
%           wb = pi/100;
%           area = (2)*pi;
%           delta = 0;
%           sigma = 1;
%           tau = 25;
%
% Run the program with these parameters to see that the spin of the
% electron oscillates between the z-axis (y(1)) and the y-axis
% (imag(y(3))). The electron spin should be completely in the y-direction
% at time 25, at which point the applied 2pi pulse flips it into the
% -y-direction. The oscillations then continue as before.

% Time array
tspan = [0:.1:250]; % [t_initial:t_step:t_final]

% Initial condition % [pzz, pzT, pzz', pTT, pTz']
% To begin the spin in the +z-direction, set y0 = [1,0,0,0,0];
% The spin will then oscillate in the y,z plane. Note y(:,4) is the
% excited state population.
y0 = [1,0,0,0,0];

% Solve ODE
```

```
% Solves the optical Bloch equations and stores the solution in the
% variable y.
[t,y] = ode45('SpinFlipODE',tspan,y0);

% Define Bloch sphere components.
X = real(y(:,3));
Y = imag(y(:,3));
Z = 2*y(:,1) - 1 + y(:,4);

% Save data. The filename "data.out" can be changed at your convenience.
A = [tspan',X,Y,Z,y(:,4)];
save data.out A -ascii

% Plot the Z component of the Bloch sphere.
plot(tspan,Z)

% End SpinFlip.m
```

```
% SpinFlipODE.m
% Written by Carey Phelps working in the Wang Laboratory at the University
% of Oregon.
%
% A file accompanying SpinFlip.m which contains the differential equation
% to be solved in computing electron spin control in the L-system.

function dydt = SpinFlipODE(t,y)

% System parameters
mu = 1; % Transition strength
G = 0; % Population decay rate
g = 0; % Dipole decoherence rate
g2 = 0; % Spin lifetime T1
wb = pi/100; % Half of Zeeman splitting (pi/period)
area = (2)*pi; % Area of applied pulse
delta = 0; % Detuning of applied pulse

% Field parameters
sigma = 1; % Pulse duration
tau = 25; % Pulse delay

% A reminder of how y is defined
% y(1)=pzz , y(2)=pzT , y(3)=pzz' , y(4)=pTT , y(5)=pTz'

% Differential equation to be solved
dydt = zeros(size(y));


dydt(1) = 2*real(i*(wb*y(3) - mu*1/(2*sigma*sqrt(2*pi))*...
        area*exp(-((t-tau)/(sqrt(2)*sigma)).^2).*y(2))) + G*y(4);
dydt(2) = (i*delta-g)*y(2) - i*wb*conj(y(5)) + i*mu*1/(2*sigma*...
        sqrt(2*pi))*area*exp(-((t-tau)/(sqrt(2)*sigma)).^2).*(y(4)-y(1));
dydt(3) = i*wb*(2*y(1)+y(4)-1) - g2*y(3) + i*mu*1/(2*sigma*sqrt(2*pi))*...
        area*exp(-((t-tau)/(sqrt(2)*sigma)).^2).*y(5);
dydt(4) = 2*real(i*mu*1/(2*sigma*sqrt(2*pi))*area*...
        exp(-((t-tau)/(sqrt(2)*sigma)).^2).*y(2)) - 2*G*y(4);
dydt(5) = -(i*delta + g)*y(5) + i*wb*conj(y(2)) +i*mu*...
        1/(2*sigma*sqrt(2*pi))*area*exp(-((t-tau)/(sqrt(2)*sigma)).^2).*y(3);


% End SpinFlipODE.m
```

```
% FP.m
% Written by Carey Phelps working in the Wang Laboratory at the University
% of Oregon.
%
% Calculates the absorption spectrum when complicated by Fabry-Perot
% interference. Absorption line is a Lorentzian convolved with a Gaussian.
%
% Unit of length is microns, unit of time is picoseconds.

R = .323; % Reflection coefficient
T = 1 - R; % Transmission coefficient
L = 10; % Sample length
c = 299.8; % Speed of light
lambda = .819; % Central absorption wavelength
del = .6; % Lorentzian linewidth
gam = 24; % Gaussian broadening
a0 = 143.4; % Absorption strength
shift = .518; % Absorption spectrum offset for matching experimental data

% Wavelength range for absorption spectrum plot
lammin = .816;
lammax = .826;
lamstep = .00001;
lam = [lammin:lamstep:lammax];

w0 = 2*pi*c/lambda; % Central absorption angular frequency


% Integrate over Gaussian distribution
for k = lammin:lamstep:lammax
        DW = [-5*gam:5*gam/100:5*gam];
        ep_int = trapz(DW,exp(-DW.^2/(2*gam^2))./((w0^2 + DW.^2)-(2*pi*c/k)^2 ...
                - i*(2*pi*c/k)*del));
        ep_temp = 1 + a0*del/2*ep_int;

        if k == lammin
                ep = [ep_temp];
        else
                ep = [ep;ep_temp];
        end
end


% Define real/imaginary parts of dielectric constant
ep1 = real(ep);
ep2 = imag(ep);

lam=lam'; % Transpose wavelength array

% Find index of refraction and absorption coefficient
n = sqrt(.5*(sqrt(ep1.^2+ep2.^2)+ep1));
```

```
a = sqrt(.5*(sqrt(ep1.^2+ep2.^2)-ep1));

% Phase shift of photon after one round trip through sample
phi = 4*L*n*pi./lam;

% Total transmission including interference
TR = T^2*exp(-2*a*L)./((1-R*exp(-2*a*L)).^2 + ...
4*R*exp(-2*a*L).*(sin(.5*phi)).^2);

% Measureed absorption spectrum
ameasured = -log(TR) + shift;

% Plot absorption spectrum versus wavelength
plot(lam,ameasured)

% End FP.m
```

```
% QWValenceBands.m Matlab script
% by Carey Phelps, Hailin Wang group (2010)
% University of Oregon and Oregon Center for Optics
%
% This script solves for the valence band bound states in a semiconductor
% quantum well for a given wavevector value. It uses the upper 3X3
% Luttinger-Kohn Hamiltonian and the Transfer Matrix Method, following the
% treatment by Paul Harrison in his book Quantum Wells, Wires and Dots,
% which can be checked out of the UO Science Library. Refer to that text
% for a detailed discussion. To produce the whole valence band structure,
% this program can be modified to include a loop that calculates the
% valence band bound states for a range of wave vector values. Seek the
% author for such a version.
%
% Bound states for a given wave vector are found by the minima of the
% graphs that this program produces. Energies in eV.
%
% Make sure the following parameters are set appropriately:
% Parameters ending in w or b correspond to well or barrier parameters,
% respectively.
% For a specific material:
% g1w, g2w, g3w, g1b, g2b, g3b, DSOw, DSOb, VBOb, VBOw
% Set well width: dw
% Strain parameters, if desired: avb, avw, bb, bw, e_xx, e_yy, e_zz
% Energy range desired: E_initial, E_step, E_final
% Set wavevector components kx and ky
%
% Parameters for various semiconductors
% g1: GaAs = 6.98, Si = 4.22, Ge = 13.4, AlAs = 3.76, InAs = 20
% g2: GaAs = 2.06, Si = 0.39, Ge = 4.25, AlAs = 0.82, InAs = 8.5
% g3: GaAs = 2.93, Si = 1.44, Ge = 5.69, AlAs = 1.42, InAs = 9.2
% DSO: GaAs = 0.341, Si = 0.044, Ge = 0.29, AlAs = 0.28, InAs = 0.39
% VBO: GaAs = -0.80, AlAs = -1.33, InAs = -0.59
% av: GaAs = -1.116, Si = 2.46, Ge = 1.24, AlAs = -2.47, InAs = -1.00
% b: GaAs = -2.0, Si = -2.10, Ge = -2.86, AlAs = -2.3, InAs = -1.8

clear

% Natural parameters
hbarEV = 6.582119; % hbar in eV
hbarSI = 1.0545716; % hbar in SI units
m0 = 9.109382; % free electron mass

% Energy range
E_initial = 0;
E_step = .0001;
E_final = .25;

% Wave vector components
kx = 0.050001;
```

```
ky = 0.05;
kpar = sqrt(kx^2+ky^2);

% Avoid singularity for kx = 0
if kx == 0
phi = pi/2;
else
phi = atan(ky/kx);
end


% Well parameters
% Luttinger parameters (don't change factor in parentheses)
        g1w = 6.98*(hbarSI*hbarEV/m0*.5*10);
        g2w = 2.06*(hbarSI*hbarEV/m0*.5*10);
        g3w = 2.93*(hbarSI*hbarEV/m0*.5*10);
% Constants
        gammabarw = .5*(g2w+g3w);
        muw = .5*(g3w-g2w);
        deltaw = 1/9*(1+g1w+g2w-3*g3w);
        piw = muw+3/2*deltaw;
        sigmaw = gammabarw-.5*deltaw;
        gphiw = sqrt(gammabarw^2+muw^2-2*gammabarw*muw*cos(phi));
% Valence band offset
        VBOw = -.8;
% Split-off band offset
        DSOw = .341;
% Will width in Angstroms
        dw = 42.5;

% Barrier parameters
% Luttinger parameters (don't change factor in parentheses)
        g1b = 3.76*(hbarSI*hbarEV/m0*.5*10);
        g2b = .82*(hbarSI*hbarEV/m0*.5*10);
        g3b = 1.42*(hbarSI*hbarEV/m0*.5*10);
% Constants
        gammabarb = .5*(g2b+g3b);
        mub = .5*(g3b-g2b);
        deltab = 1/9*(1+g1b+g2b-3*g3b);
        pib = mub+3/2*deltab;
        sigmab = gammabarb-.5*deltab;
        gphib = sqrt(gammabarb^2+mub^2-2*gammabarb*mub*cos(phi));
% Valence band offset
        VBOb = -1.33;
% Split-off band offset
        DSOb = .28;
% Barrier width (zero by convention when using transfer matrix method)
        db = 0;

% Valence band offset difference
        V = VBOb - VBOw;
```

```
% Strain parameters
        e_xx = 0;
        e_yy = 0;
        e_zz = 0;

        avb = -2.47;
        avw = -1.116;
        bb = -2.3;
        bw = -2.0;

        Peb = -avb*(e_xx+e_yy+e_zz);
        Qeb = -.5*bb*(e_xx+e_yy-2*e_zz);

        Pew = -avw*(e_xx+e_yy+e_zz);
        Qew = -.5*bw*(e_xx+e_yy-2*e_zz);

% Identity matrix
Identity = [1,0,0;0,1,0;0,0,1];

% Begin loop over energy values
for E = E_initial:E_step:E_final

% Upper 3x3 Luttinger-Kohn Hamiltonian in barrier
H2b = [g1b-2*g2b,0,0;0,g1b+2*g2b,-2*sqrt(2)*g2b;0,-2*sqrt(2)*g2b,g1b];
H1b = [0,-1i*2*sqrt(3)*g3b*kpar,1i*sqrt(6)*g3b*kpar;1i*2*sqrt(3)*g3b*...
        kpar,0,-1i*3*sqrt(2)*g3b*kpar;-1i*sqrt(6)*g3b*kpar,1i*3*sqrt(2)*...
        g3b*kpar,0];
H0b = [(g1b+g2b)*kpar^2+Peb+Qeb-V,-sqrt(3)*gphib*kpar^2,-sqrt(6)*gphib*...
        kpar^2;-sqrt(3)*gphib*kpar^2,(g1b-g2b)*kpar^2+Peb-Qeb-V,sqrt(2)*...
        (g2b*kpar^2+Qeb);-sqrt(6)*gphib*kpar^2,sqrt(2)*(g2b*kpar^2+Qeb),...
        g1b*kpar^2+Peb+DSOb-V];

HLb = -inv(H2b)*(H0b-E*Identity);
HRb = -inv(H2b)*H1b;

Htotb = [0,0,0,1,0,0;0,0,0,0,1,0;0,0,0,0,0,1;HLb(1,1),HLb(1,2),...
        HLb(1,3),HRb(1,1),HRb(1,2),HRb(1,3);HLb(2,1),HLb(2,2),HLb(2,3),...
        HRb(2,1),HRb(2,2),HRb(2,3);HLb(3,1),HLb(3,2),HLb(3,3),HRb(3,1),...
        HRb(3,2),HRb(3,3)];

% Find kz eigenvalues in barrier
[kzbV,kzbD] = eig(Htotb);

% Reorder eigenvalue vector so that "forward" moving wavefunctions are in
% the upper rows and "backward" moving wavefunctions are in the lower rows.
kzb = -1i*[kzbD(1,1);kzbD(2,2);kzbD(3,3);kzbD(4,4);kzbD(5,5);kzbD(6,6)];
[kzb,kzbindex] = esort(kzb);
kzb = 1i*[kzb(1);kzb(2);kzb(3);kzb(6);kzb(5);kzb(4)];
```

```
% Define matrix of eigenvectors with the same ordering as the eigenvalues.
Ub = [kzbV(:,kzbindex(1)),kzbV(:,kzbindex(2)),kzbV(:,kzbindex(3)),...
        kzbV(:,kzbindex(6)),kzbV(:,kzbindex(5)),kzbV(:,kzbindex(4))];
Ub = [Ub(1,:);Ub(2,:);Ub(3,:);1i*Ub(4,:);1i*Ub(5,:);1i*Ub(6,:)];
Ubinv = inv(Ub);

% Propagation matrix in barrier
Db = [exp(1i*kzb(1)*db),0,0,0,0,0;0,exp(1i*kzb(2)*db),0,0,0,0;0,0,...
        exp(1i*kzb(3)*db),0,0,0;0,0,0,exp(1i*kzb(4)*db),0,0;0,0,0,0,...
        exp(1i*kzb(5)*db),0;0,0,0,0,0,exp(1i*kzb(6)*db)];

% Boundary matching matrix in barrier
B1b = [0,2*sqrt(3)*pib*kpar,-sqrt(6)*pib*kpar;-2*sqrt(3)*...
        (sigmab-deltab)*kpar,2*(sigmab-deltab-pib)*kpar,sqrt(2)*...
        (2*sigmab-2*deltab+pib)*kpar;sqrt(6)*(sigmab-deltab)*kpar,-sqrt(2)*...
        (sigmab-deltab+2*pib)*kpar,-2*(sigmab-deltab-pib)*kpar];
B2b = [g1b-2*g2b,0,0;0,g1b+2*g2b,-2*sqrt(2)*g2b;0,-2*sqrt(2)*g2b,g1b];

Ib = [1,0,0,0,0,0,0;0,1,0,0,0,0,0;0,0,1,0,0,0,0;B1b(1,1),B1b(1,2),B1b(1,3),...
        B2b(1,1),B2b(1,2),B2b(1,3);B1b(2,1),B1b(2,2),B1b(2,3),B2b(2,1),...
        B2b(2,2),B2b(2,3);B1b(3,1),B1b(3,2),B1b(3,3),B2b(3,1),B2b(3,2),...
        B2b(3,3)];
Ibinv = inv(Ib);

% Upper 3x3 Luttinger-Kohn Hamiltonian in well
H2w = [g1w-2*g2w,0,0;0,g1w+2*g2w,-2*sqrt(2)*g2w;0,-2*sqrt(2)*g2w,g1w];
H1w = [0,-1i*2*sqrt(3)*g3w*kpar,1i*sqrt(6)*g3w*kpar;1i*2*sqrt(3)*g3w*...
        kpar,0,-1i*3*sqrt(2)*g3w*kpar;-1i*sqrt(6)*g3w*kpar,1i*3*sqrt(2)*...
        g3w*kpar,0];
H0w = [(g1w+g2w)*kpar^2+Pew+Qew,-sqrt(3)*gphiw*kpar^2,-sqrt(6)*gphiw*...
        kpar^2;-sqrt(3)*gphiw*kpar^2,(g1w-g2w)*kpar^2+Pew-Qew,sqrt(2)*...
        (g2w*kpar^2+Qew);-sqrt(6)*gphiw*kpar^2,sqrt(2)*(g2w*kpar^2+Qew),...
        g1w*kpar^2+Pew+DSOw];

HLw = -inv(H2w)*(H0w-E*Identity);
HRw = -inv(H2w)*H1w;

Htotw = [0,0,0,1,0,0;0,0,0,0,1,0;0,0,0,0,0,1;HLw(1,1),HLw(1,2),...
        HLw(1,3),HRw(1,1),HRw(1,2),HRw(1,3);HLw(2,1),HLw(2,2),HLw(2,3),...
        HRw(2,1),HRw(2,2),HRw(2,3);HLw(3,1),HLw(3,2),HLw(3,3),HRw(3,1),...
        HRw(3,2),HRw(3,3)];

% Find kz eigenvalues in well
 [kzwV,kzwD] = eig(Htotw);

% Reorder eigenvalue vector so that "forward" moving wavefunctions are in
% the upper rows and "backward" moving wavefunctions are in the lower rows.
kzw = -1i*[kzwD(1,1);kzwD(2,2);kzwD(3,3);kzwD(4,4);kzwD(5,5);kzwD(6,6)];
[kzw,kzwindex] = esort(kzw);
kzw = 1i*[kzw(1);kzw(2);kzw(3);kzw(6);kzw(5);kzw(4)];
```

```
% Define matrix of eigenvectors with the same ordering as the eigenvalues.
Uw = [kzwV(:,kzwindex(1)),kzwV(:,kzwindex(2)),kzwV(:,kzwindex(3)),...
        kzwV(:,kzwindex(6)),kzwV(:,kzwindex(5)),kzwV(:,kzwindex(4))];
Uw = [Uw(1,:);Uw(2,:);Uw(3,:);1i*Uw(4,:);1i*Uw(5,:);1i*Uw(6,:)];
Uwinv = inv(Uw);

% Propagation matrix in well
Dw = [exp(1i*kzw(1)*dw),0,0,0,0,0;0,exp(1i*kzw(2)*dw),0,0,0,0;0,0,...
        exp(1i*kzw(3)*dw),0,0,0;0,0,0,exp(1i*kzw(4)*dw),0,0;0,0,0,0,...
        exp(1i*kzw(5)*dw),0;0,0,0,0,0,exp(1i*kzw(6)*dw)];

% Boundary matching matrix in well
B1w = [0,2*sqrt(3)*piw*kpar,-sqrt(6)*piw*kpar;-2*sqrt(3)*...
        (sigmaw-deltaw)*kpar,2*(sigmaw-deltaw-piw)*kpar,sqrt(2)*...
        (2*sigmaw-2*deltaw+piw)*kpar;sqrt(6)*(sigmaw-deltaw)*kpar,-sqrt(2)*...
        (sigmaw-deltaw+2*piw)*kpar,-2*(sigmaw-deltaw-piw)*kpar];
B2w = [g1w-2*g2w,0,0;0,g1w+2*g2w,-2*sqrt(2)*g2w;0,-2*sqrt(2)*g2w,g1w];

Iw = [1,0,0,0,0,0;0,1,0,0,0,0;0,0,1,0,0,0;B1w(1,1),B1w(1,2),B1w(1,3),...
        B2w(1,1),B2w(1,2),B2w(1,3);B1w(2,1),B1w(2,2),B1w(2,3),B2w(2,1),...
        B2w(2,2),B2w(2,3);B1w(3,1),B1w(3,2),B1w(3,3),B2w(3,1),B2w(3,2),...
        B2w(3,3)];
Iwinv = inv(Iw);

% Total transfer matrix
T = Ubinv*Ibinv*Iw*Uw*Dw*Uwinv*Iwinv*Ib*Ub*Db;
% Lower right 3x3 block of transfer matrix
T22 = [T(4,4),T(4,5),T(4,6);T(5,4),T(5,5),T(5,6);T(6,4),T(6,5),T(6,6)];
A = abs(det(T22));

% Build array of absolute value of determinants of matrix T22
if E == E_initial
        detT22 = [A];
else
        detT22 = [detT22;A];
end

end

% Define values for finding minima of logdetT22
Espan = [E_initial:E_step:E_final]';
Ebound = [0];
logdetT22 = log(detT22);

for k = 2:1:size(logdetT22) - 1
        if logdetT22(k) < logdetT22(k-1) && logdetT22(k) < logdetT22(k+1)
                Ebound = [Ebound,Espan(k)];
        end
```

```
end

% Print bound state energies (Note: first value of 0 is not a bound state)
Ebound'

% Save data
B = [Espan,logdetT22];
save QWValenceBands.m B -ascii

% Plot log of absolute value of determinant of T22. Minima are bound states
plot(Espan,logdetT22)

% End QWValenceBands.m
```

REFERENCES CITED

[1] I. Zŭtić and J. Fabian, Nature **447**, 268 (2007).

[2] R. P. Feynman, Int. J. Theor. Phys. **21**, 467 (1982).

[3] M. N. Baibich, J. M. Broto, A. Fert, N. Van Dau, F. Petroff, P. Etienne, G. Creuzet, A. Friederich, and J. Chazelas, Phys. Rev. Lett. **61**, 2472 (1988).

[4] G. Dresselhaus, Phys. Rev. **100**, 580 (1955).

[5] Y. A. Bychkov and E. I. Rashba, J. Phys. C: Solid State Phys. **17**, 6039 (1984).

[6] J. R. Petta, A. C. Johnson, J. M. Taylor, E. A. Laird, A. Yacoby, M. D. Lukin, C. M. Marcus, M. P. Hanson, and A. C. Gossard, Science **309**, 2180 (2005).

[7] F. H. L. Koppens, C. Buizert, K. J. Tielrooij, I. T. Vink, K. C. Nowack, T. Meunier, L. P. Kouwenhoven, and L. M. K. Vandersypen, Nature **442**, 766 (2006).

[8] K. C. Nowack, F. H. L. Koppens, Y. V. Nazarov, and L. M. K. Vandersypen, Science **318**, 1430 (2007).

[9] J. Berezovsky, M. H. Mikkelsen, N. G. Stoltz, L. A. Coldren, and D. D. Awschalom, Science **320**, 349 (2008).

[10] D. Press, T. D. Ladd, Bingyang, and Y. Yamamoto, Nature **456**, 218 (2008).

[11] E. D. Kim, K. Truex, X. Xu, B. Sun, D. G. Steel, A. S. Bracker, D. Gammon, and L. J. Sham, Phys. Rev. Lett. **104**, 167401 (2010).

[12] A. Greilich, S. E. Economou, S. Spatzek, D. R. Yakovlev, D. Reuter, A. D. Wieck, T. L. Reinecke, and M. Bayer, Nature Phys. **5**, 262 (2009).

[13] H. J. Briegel, W. Dür, J. I. Cirac, and P. Zoller, Phys. Rev. Lett. **81**, 5932 (1998).

[14] R. Benzaquen, R. Leonelli, and S. Charbonneau, Phys. Rev. Lett. **61**, 2472 (1988).

[15] K. C. Fu, W. Yeo, S. M. Clark, C. Santori, C. R. Stanley, M. C. Holland, and Y. Yamamoto, Phys. Rev. B **74**, 121304 (2006).

[16] E. A. Zhukov, D. R. Yakovlev, M. Bayer, M. M. Glazov, E. L. Ivchenko, G. Karczewski, T. Wojtowicz, and J. Kossut, Phys. Rev. B **76**, 205310 (2007).

[17] P. Gilliot, D. Brinkmann, J. Kudrna, O. Crégut, R. Lévy, A. Arnoult, J. Cibert, and S. Tatarenko, Phys. Rev. B **60**, 5797 (1999).

[18] Y. Shen, A. M. Goebel, and H. Wang, Phys. Rev. B **75**, 045341 (2007).

[19] S. G. Carter, Z. Chen, and S. T. Cundiff, Phys. Rev. B **76**, 201308 (2007).

[20] J. A. Gupta, R. Knobel, N. Samarth, and D. D. Awschalom, Science **292**, 2458 (2001).

[21] C. Phelps, T. Sweeney, R. T. Cox, and H. Wang, Phys. Rev. Lett. **102**, 237402 (2009).

[22] C. Kittel, *Introduction to Solid State Physics, 6th Edition* (Wiley, New York, 1986).

[23] P. Harrison, *Quantum Wells, Wires, and Dots, 2nd Edition* (Wiley, New York, 2005).

[24] C. R. Pidgeon and R. N. Brown, Phys. Rev. **146**, 575 (1966).

[25] G. Wannier, Phys. Rev. **52**, 191 (1937).

[26] S. A. Crooker, D. D. Awschalom, J. J. Baumberg, F. Flack, and N. Samarth, Phys. Rev. B **56**, 7574 (1997).

[27] S. L. Chuang, Phys. Rev. B **43**, 9649 (1991).

[28] A. M. Malik, M. J. Godfrey, and P. Dawson, Phys. Rev. B **59**, 2861 (1999).

[29] P. Chen, C. Piermarocchi, L. J. Sham, D. Gammon, and D. G. Steel, Phys. Rev. B **69**, 075320 (2004).

[30] S. E. Economou and L. J. Sham, Phys. Rev. B **74**, 205415 (2006).

[31] C. Emary and L. J. Sham, J. Phys.: Condens. Matter **19**, 056203 (2007).

[32] L. Allen and J. H. Eberly, *Optical Resonance and Two-Level Atoms* (Wiley, New York, 1975).

[33] T. Sweeney, C. Phelps, and H. Wang, *submitted for review* (2011).

[34] J. J. Sakurai, *Modern Quantum Mechanics, Revised Edition* (Addison-Wesley, Reading, MA, 1994).

[35] M. C. Phillips, Ph.D. thesis, University of Oregon, Eugene, Oregon (2002).

[36] T. A. Kennedy, A. Shabaev, M. Scheibner, A. L. Efros, A. S. Bracker, and D. Gammon, Phys. Rev. B **73**, 045307 (2006).

[37] A. A. Sirenko, T. Ruf, and M. Cardona, Phys. Rev. B **56**, 2114 (1997).

[38] K. Kheng, R. T. Cox, Y. M. d'Aubigné, F. Bassani, K. Saminadayar, and S. Tatarenko, Phys. Rev. Lett. **71**, 1752 (1993).

[39] D. G. Allen, C. R. Stanley, and M. S. Sherwin, Phys. Rev. B **72**, 035302 (2005).

[40] M. A. Gilleo, P. T. Bailey, and D. E. Hill, Phys. Rev. **174**, 898 (1968).

[41] V. A. Karasyuk, D. G. S. Beckett, M. K. Nissen, A. Villemaire, T. W. Steiner, and M. L. W. Thewalt, Phys. Rev. B **49**, 16381 (1994).

[42] H. Atzmüller, F. Fröschl, and U. Schröder, Phys. Rev. B **19**, 3118 (1979).

[43] B. Gil, P. Bigenwald, M. Leroux, P. P. Paskov, and B. Bonemar, Phys. Rev. B **75**, 085204 (2007).

[44] A. M. White, P. J. Dean, and B. Day, J. Phys. C: Solid State Phys. **7**, 1400 (1973).

[45] W. Rühle and W. Klingenstein, Phys. Rev. B **18**, 7011 (1978).

[46] K. C. Fu, S. M. Clark, C. Santori, C. R. Stanley, M. C. Holland, and Y. Yamamoto, Nature Phys. **4**, 780 (2008).

[47] S. M. Clark, K. C. Fu, Q. Zhang, T. D. Ladd, C. Stanley, and Y. Yamamoto, Phys. Rev. Lett. **102**, 247601 (2009).

[48] K. C. Fu, Ph.D. thesis, Stanford University (2007).

[49] H. F. Pen, F. A. J. M. Driessen, S. M. Olsthoorn, and L. J. Giling, Semicond. Sci. Technol. **7**, 1400 (1992).

[50] E. H. Bogardus and H. B. Bebb, Phys. Rev. **176**, 993 (1968).

[51] K. Haruna, H. Maeta, and T. Koike, J. Phys. C: Solid State Phys. **20**, 5275 (1987).

[52] M. Lucht, M. Lerche, H.-C. Wille, Y. V. Shvyd'ko, H. D. Rüter, E. Gerdau, and P. Becker, J. Appl. Cryst. **36**, 1075 (2003).

[53] F. A. J. M. Driessen, H. G. M. Lochs, S. M. Olsthoorn, and L. J. Giling, J. Appl. Phys. **69**, 906 (1991).

[54] S. P. Watkins, R. Arès, R. A. Masut, C. A. Tran, and J. L. Brebner, J. Appl. Phys. **75**, 2460 (1994).

[55] C. Phelps, J. Prineas, and H. Wang, Phys. Rev. B **83**, 153302 (2011).

[56] I. Galbraith, P. Dawson, and C. T. Foxon, Phys. Rev. B **45**, 13499 (1992).

[57] M. R. A. Shegelski, J. Kavka, and J. Hnybida, Am. J. Phys. **75**, 504 (2007).

[58] E. T. Yu, M. K. Jackson, and T. C. McGill, Appl. Phys. Lett. **55**, 744 (1989).

[59] H. Cruz, A. Hernandez-Cabrera, and A. Muñoz, Semicond. Sci. Technol. **7**, 332 (1992).

[60] A. Tackeuchi, A. P. Heberle, W. W. Rühle, and K. Köhler, Jpn. J. Appl Phys. **34**, L543 (1995).

[61] D. A. Kleinman and R. C. Miller, Phys. Rev. B **32**, 2266 (1985).

[62] I. B. Spielman, J. P. Eisenstein, L. N. Pfeiffer, and K. W. West, Phys. Rev. Lett. **84**, 5808 (2000).

[63] J. P. Eisenstein and A. H. MacDonald, Nature **432**, 691 (2004).

[64] G. Yusa, H. Shtrikman, and I. Bar-Joseph, Phys. Rev. B **62**, 15390 (2000).

[65] S. I. Gubarev, I. V. Kukushkin, S. V. Tovstonog, M. Y. Akimov, J. Smet, K. von Klitzing, and W. Wegscheider, JETP Letters **72**, 324 (2000).

[66] M. D. Sturge, Phys. Rev. **127**, 768 (1962).

[67] H. D. Sun, T. Makino, N. T. Tuan, Y. Segawa, M. Kawasaki, A. Ohtomo, K. Tamura, and H. Koinuma, Appl. Phys. Lett. **78**, 2464 (2001).

[68] H. Haug and S. W. Koch, *Quantum Theory of the Optical and Electronic Properties of Semiconductors, 5th Edition* (World Scientific, Singapore, 2009).

[69] I. E. Perakis and D. S. Chemla, Phys. Rev. Lett. **72**, 3202 (1994).

[70] M. Born and E. Wolf, *Principles of Optics, 6th Edition* (Pergamon, New York, 1980).

[71] Y. Zhu, D. J. Gauthier, S. E. Morin, Q. Wu, H. J. Carmichael, and T. W. Mossberg, Phys. Rev. Lett. **64**, 2499 (1990).

[72] J. D. Jackson, *Classical Electrodynamics, 3rd Edition* (Wiley, New York, 1999).